6-25-2021

Investigation of Bipolar Electrochemically Exfoliated Graphene for Supercapacitor Applications

Iman Khakpour
ikhak002@fiu.edu

FLORIDA INTERNATIONAL UNIVERSITY

Miami, Florida

INVESTIGATION OF BIPOLAR ELECTROCHEMICALLY EXFOLIATED GRAPHENE FOR SUPERCAPACITOR APPLICATIONS

A dissertation submitted in partial fulfillment of the

requirement for the degree of

DOCTOR OF PHILOSOPHY

in

MATERIALS SCIENCE AND ENGINEERING

by

Iman Khakpour

2021

To: Dean John L. Volakis
College of Engineering and Computing

This dissertation, entitled Investigation of Bipolar Electrochemically Exfoliated Graphene for Supercapacitor Applications, written by Iman Khakpour, having been approved in respect to style and intellectual content, is referred to you for judgment.

We have read this dissertation and recommend that it be approved.

Norman D. H. Munroe

Bilal El-Zahab

Zhe Cheng

Jin He

Chunlei Wang, Major Professor

Date of Defense: June 25, 2021

The dissertation of Iman Khakpour is approved.

Dean John L. Volakis
Dean of College of Engineering and Computing

Andrés G. Gil
Vice President for Research and Economic Development
and Dean of the University Graduate School

Florida International University, 2021

DEDICATION

This dissertation is wholeheartedly dedicated to my beloved family, who have been my constant source of inspiration, gave me strength, and continually provide their moral, spiritual, emotional, and financial support.

My Father's Soul, Karim

My Mother, Shahla

My Brother, Alireza

ACKNOWLEDGMENTS

First and foremost, I would like to express my sincere gratitude to my advisor Dr. Chunlei Wang who provided me with her aspiring guidance, invaluable constructive criticism and friendly advice. She always supported me throughout my research with dedication, patience and encouragement.

I would also like to express my deepest appreciation to the members of my dissertation committee – Dr. Norman Munroe, Dr. Bilal El-Zahab, Dr. Zhi Cheng, and Dr. Jin He for their willingness to serve on my committee and for providing unwavering support, suggestion and professional and personal guidance during my Ph.D. My sincere thanks also go to Dr. Anis Allagui, and Dr. Majid Beidaghi for their help and support along the way.

This work would not have been possible without the technical facilities provided at Advanced Materials Engineering Research Institute (AMERI) and the Center of Study Matter at Extreme Condition (CeSMEC) at FIU. I am very grateful to Dr. Patrick Roman, Dr. Alexander Franco Hernandez, Dr. Andriy Durigin, Jonathan Comparan, and Steward Schwarz for their patience and help with my experimentation.

I am thankful to all my friends and labmates, Dr. Negar Firoozi, Dr. Amin Rabiei Babokani, Dr. Shervin Tashakori, Dr. Hossein Talebinezhad, Dr. Jafar Orangi, Dr. Richa Agrawal, Dr. Ebenezer Dotun Adelowo, Shahrzad Forouzanfar, Omena Okpowe, Azmal Chowdhury, and Borzooye Jafarizadeh, Ali Bakhtiari, for their company, invaluable help and support during my Ph.D.

I am very thankful to the University Graduate School (UGS) at Florida International University for supporting me through Dissertation Evidence Acquisition (DEA), and Dissertation Year Fellowship (DYF) awards. I am also thankful to the Department of Mechanical and Materials Engineering (MME) at FIU for providing me with teaching

assistantship (TA) and the National Science Foundation (NSF) to support my Ph.D. program.

Finally, and most importantly, I could not have accomplished this without the support of my family. From the bottom of my heart, I wish to thank my beloved parents for their love, caring, and sacrifices for educating and preparing me for my future. Also, I express my thanks to the teachers, professors, and other professionals who either directly trained me or inspired me in some way.

ABSTRACT OF THE DISSERTATION

INVESTIGATION OF BIPOLAR ELECTROCHEMICALLY EXFOLIATED GRAPHENE FOR SUPERCAPACITOR APPLICATIONS

by

Iman Khakpour

Florida International University, 2021

Miami, Florida

Professor Chunlei Wang, Major Professor

Developing a reliable, simple, cost-efficient and eco-friendly method for scale-up production of high-quality graphene-based materials is essential for the broad applications of graphene. Up to now, various manufacturing methods have been employed for synthesizing high quality graphene, however aggregation and restacking has been a major issue and the majority of commercially available graphene products are actually graphite microplates. In this study, bipolar electrochemistry techniques have been used to exfoliate and deposit graphene nanosheets in a single-step process to enable high performance device application.

In the first part of this study, bipolar electrochemistry concept is utilized to design a single-step and controllable process for simultaneously exfoliating a graphite source and depositing both graphene oxide (GO) and reduced graphene oxide (rGO) layers on conductive substrates. The electrochemical performance of the fabricated graphene-based materials as the electrode for supercapacitors has been investigated. Areal capacitance of 1.932 mF cm^{-2} for the rGO, and 0.404 mF cm^{-2} for GO at a scan rate of 2 mV s^{-1} were achieved. Moreover, a cut-off frequency of 1820 Hz was obtained, which is a promising characteristic for AC filtering applications.

Although the physicochemical characteristics of produced graphene have been evaluated in the first part, the exfoliation and deposition mechanisms were still unclear. In the second part of this dissertation, a novel modified BPE system with an electrically connected graphite-platinum couple acting as the bipolar electrode has been designed in order to decouple and investigate the contribution of anodic/cathodic exfoliation and deposition of graphene in the BPE process. Electron microscopy and infrared spectroscopy results indicate that both anodic and cathodic exfoliation of graphene could take place regardless of the type of polarization; however, the morphology and deposition rate highly depend on the polarization. Furthermore, the graphene fabricated by anodic exfoliation was found to show higher levels of oxidation compared to the graphene produced by cathodic exfoliation.

In the last part of this study, for the first time, a vertically aligned graphene layer was deposited on a micro-sized interdigitated gold current collector by a modified bipolar electrochemistry method. Both time domain and frequency domain electrochemical performance of on-chip micro-supercapacitors (MSCs) were evaluated. An areal capacity of 640.9 $\mu F\ cm^{-2}$ at a scan rate of 2 mV s^{-1} and 239.31 $\mu F\ cm^{-2}$ at discharge current density of 25 $\mu A\ cm^{-2}$ was delivered with an excellent cyclability. Most importantly, the MSC exhibited a very fast response (cut-off frequency of 3486 Hz) and very close to ideal performance (phase angle reached -83.2°) at low frequencies.

For the first time, this dissertation reported the modified BPE method as a novel approach for three in one exfoliation, deposition and reduction of high-quality graphene with vertically aligned and porous structure. The unique design of the BPE cell enabled the author to study the BPE mechanisms and measure the bipolar current for the first time. The method could successfully be employed to fabricate fast response microsupercapacitors based on vertically aligned graphene nanosheets.

TABLE OF CONTENTS

LIST OF TABLES

TABLE PAGE

LIST OF FIGURES

FIGURE PAGE

1. Introduction

1.1 Overview

The recent boom in the development of renewable energy sources, mobile electronics, and electric vehicles has increased the demand for high-performance energy storage devices. Good cyclability, high energy density and power density, in addition to being environmentally friendly and cost-efficient, are usually considered as the main performance features for energy storage systems. However, the required characteristics of the devices are very specific due to their applications. Particularly about the miniaturized electronics such as implantable devices, wireless microsensors, energy harvesting and wearable devices, the required energy ranges from several hundred μWh to several hundred mWh while they need a power of several hundred μW to several hundred mW. The operation frequency of these devices usually ranges from some hertz to several hundred hertz [1, 2].

Supercapacitors which can provide high power density (fast charging and discharging) and also long cycle life with high-frequency responses have attracted the attention of scientists in both academia and industry for being used as the energy source of aforementioned devices and also in AC to DC converters and filtering circuits [3-5]. The development of new electrode materials with modified microstructures is one of the most promising approaches to improve the performance of these energy storage devices. From the electrode fabrication point of view, different two-dimensional (2D) materials with different nanostructures have been successfully employed to improve the performance of the

supercapacitors. However, developing a scale-up, cost-efficient, and environmentally friendly approach for the fabrication of high-performance electrodes is still demanded.

1.2 **Research Problems**

The ultimate goal of this dissertation is to develop a facile, cost-efficient, environmentally friendly, and scale-up bipolar electrochemistry process for the fabrication of high capacity and fast response electrochemical Micro/Macro supercapacitors based on graphene electrodes. Moreover, to have an insight into the performance of the fabricated electrode material, the capacity and frequency response of fabricated supercapacitors should be evaluated. The research problems encountered in this dissertation and their possible solutions are discussed as follows:

1- How to reliably fabricate high-quality graphene with controllable functionality?

The fabrication and also deposition of graphene oxide have been reported by the bipolar electrochemistry process. However, the deposited material did not show good conductivity and acceptable electrochemical performance before a further reduction process [6-8]. Modifying the geometry of the bipolar cell and other parameters can result in the deposition of graphene on both positive and negative feeding electrodes of the bipolar cell. Since reduction is the dominant reaction on the negative feeding electrode, this will help to reduce the deposited graphene. Therefore, by controlling the bipolar parameters, the properties of fabricated graphene can be controlled in a wide range, from highly reduced graphene oxide to the highly defected graphene oxide bonded with different functional groups.

2- What is the underlying exfoliation mechanism that occurred (anodic vs. cathodic) during the bipolar electrochemical process?

Research interest in the electrochemical exfoliation of graphene from graphite has significantly increased in the last decade. The exfoliation mechanism mainly depends on the graphite's polarity (positive or negative) and the present ions in the electrolyte. Both anodic and cathodic exfoliation of graphite has been reported in the literature. It has been reported that the properties of exfoliated graphene are highly dependent on these two factors. In the exfoliation of graphene by BPE, the graphite acts as the BE, which experiences both anodic and cathodic polarization at the same time. Therefore, in a conventional bipolar cell, it is not possible to find out the dominant exfoliation mechanism. To address this problem, a set of experiments should be designed in a way that can stop one of the exfoliation processes and keep the other one active and compare the results with the reverse condition.

3- How to integrate the exfoliated graphene on the microfabricated structures?

Recent developments in the fabrication of microelectronic devices rapidly increased the demand for micro energy storage systems that can be integrated with other microelectronic compounds. Micro supercapacitors (MSCs) are attractive candidates to be an alternate for bulky electrolytic capacitors or batteries in small device applications [9-15]. Recently, using nanostructured 2D materials such as carbon nanotube, graphene, Mxene, and phosphorene for the fabrication of MSCs resulted in significant improvements in their energy and power density [16, 17]. However, achieving a cost-efficient, reliable, environmentally friendly, and simple method to fabricate high-performance MSCs is still challenging [17-19].

To study the compatibility of the BPE process in the fabrication of MSCs, a gold-based MEMS with an in-plane interdigitated design can be used as the feeding electrode in the BPE process. Since the deposition is an electrophoretic phenomenon, the deposition should take place uniformly on the surface of the gold microelectrodes. However, some modifications should be done to compensate the decrease in the surface area of feeding electrodes.

1.3 Hypotheses

Bipolar electrochemistry is a promising method for fabricating high-quality graphene materials in a simple, cost-efficient, environmentally friendly, and controllable process. A deep understanding of the process and properties of fabricated graphene can leads to improve the applications of the BPE process for the fabrication of graphene-based devices. The particular hypothesis encountered in this thesis are as follows:

1- Single-step BPE technique could create enough potential on the graphite bipolar electrode to activate the exfoliation process and break the Van der Waals bonds of carbon layers in graphite. The exfoliated graphene nanosheets may have either a positive or negative charge, depends on the functional groups and ions bonded to the nanosheets. **Therefore nanosheets with different functionality and properties could be deposited on different sides of feeding electrodes**.

2- The positive polarization promotes the oxidation reactions, where reduction is the dominant electrochemical reaction on the electrode with negative polarization. **Therefore, the graphene deposited on the positive feeding electrode is expected to be at a higher**

level of oxidation compared to the one deposited on the negative feeding electrode. **Reducing effect at negative feeding electrode could produce rGO.**

3- Both anodic and cathodic electrochemical exfoliation of graphene is probable due to the applied potential to the graphite source and present ions in the electrolyte. In the fabrication of graphene through BPE, the BE (graphite rod) polarizes to both positive and negative potentials simultaneously; however, **either anodic or cathodic exfoliation could be the dominant exfoliation mechanism that controls the properties of fabricated graphene**.

4- Either the anodic or the cathodic exfoliation mechanism could be regulated by placing a platinum wire on the anodic or cathodic side of the bipolar electrode, respectively.

5- The unique porous and vertically aligned structure of the deposited graphene on microelectrodes can minimize the electric and ionic resistance of the supercapacitors and increase their response rate

6- Integration of vertically aligned graphene nanosheets into microsupercapacitors could significantly improve the performance of supercapacitors, which is favorable for high-frequency applications such as AC line filter circuits.

1.4 **Research Plan**

The research plan adopted for this dissertation is presented in Figure 1-1; the specific goals that were worked toward are as follow:

1- *Bipolar Exfoliation and in Situ Deposition of High-Quality Graphene.*

In an attempt to fabricate and deposit high-quality graphene on a conductive substrate, a graphite rod will be placed between two stainless steel feeding electrodes in deionized

water, which are connected to a DC voltage power supply. The next step is evaluation the formed material on both anode and cathode stainless feeding electrodes.

2- *Defining the dominant exfoliation mechanism*

A modified bipolar cell was developed to define the source of graphene, which was deposited on each of the electrodes. In this new configuration, a graphite rod that was electrically connected to a platinum wire will act as the bipolar electrode. Thus, either anodic or cathodic exfoliation of graphite was retarded in each experiment. Then, material properties of deposited graphene on the feeding electrodes when the graphite was polarized negatively or positively were investigated.

3- *Conducting BPE to deposit vertically aligned graphene to enable high performance* micro-supercapacitor *for AC-DC filtering applications*

In an attempt to develop a fast response and high capacity micro-supercapacitor (MSCs), a modified photolithography process was employed to fabricate in-plane interdigitated MEMS current collector. Then the fabricated MEMS was used as the feeding electrode of the bipolar process. The electrochemical performances of produced micro-supercapacitors were evaluated. The performance of MSCs for being used in AC line filtering circuits was also studied.

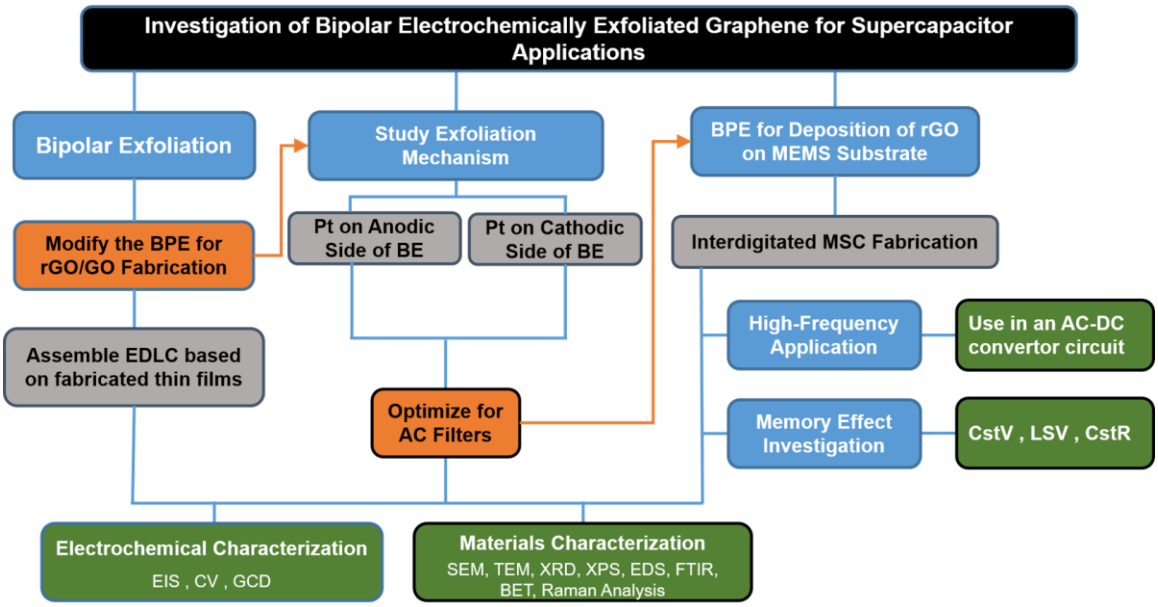

Figure 1-1. Flow chart of the research plan.

BE: Bipolar electrode
EIS: Electrochemical impedance spectroscopy
CV: Cyclic Voltammetry
GCD: Galvanostatic charge-discharge
CstV: Constant voltage
LSV: Linear sweep voltammetry
CstR: Constant resistance

1.5 Scope of the Dissertation

This dissertation consists of eight chapters. The first chapter highlights the research problems, hypothesis and research plan. Chapter 2 provides the literature review and the dissertation's background about supercapacitors, graphene fabrication as an exclusive electrode material and bipolar electrochemistry (BPE) as a new approach for the fabrication of graphene. Chapter 3 provides a detailed methodology for the adopted experimental techniques, including bipolar electrochemical exfoliation, microdevice fabrication, materials and electrochemical characterizations. Chapter 4 discusses the developed BPE

approach for the fabrication of graphene-based electrodes in addition to its electrochemical performance as a double-layer supercapacitor. Chapter 5 provides an in-depth study of the mechanistic pathways of exfoliation and deposition of graphene by bipolar. A modified BPE system has been developed to retard either anodic or cathodic exfoliation of graphene, and the differences between the materials deposited in either of these setups have been studied. In chapter 6, the BPE method has been used to integrate vertically aligned rGO into an interdigitated micro-current collector. The final product was a high-performance micro supercapacitor that could provide high specific capacitance and very high-frequency response. The fabrication process, both for micro current collectors and BPE process in addition to materials and electrochemical characterizations, have been discussed in detail. Chapter 7 provides a summary and possible future work direction of this dissertation. All of the refrences are listed in chapter 8.

2. Background and Literature Review

2.1 Historical Overview

The concept of double-layer capacitance was described by Hermann von Helmholtz in 1853 [20]. In 1957, General Electric company patented the first electrochemical double layer charge storage device developed based on porous carbon electrodes [21]. However, at that time, they did not clearly know that their device works based on double-layer charge storage mechanism. In 1978, Nippon Electric Company (NEC) marketed and commercialized the first electrochemical capacitor and named it "supercapacitors" [1]. In the late 1970s, B. Conway developed an electrochemical capacitor based on ruthenium oxide electrodes. This concept was the first reported supercapacitor that used "pseudocapacitive" mechanism to store charge. After that, the field of electrochemical supercapacitors showed great potential to reach much higher performances than traditional electrolytic capacitors. Therefore, in the 1990s, the electrochemical supercapacitor field is flourished and received growing attention from researchers since then.

The discovery of graphene in 2004 by Andre Geim and Konstantin Novoselov made a revolution in the field of Electrochemical Double Layer Capacitors (EDLCs). The high specific surface area, in addition to the excellent electrical conductivity and charge mobility, made graphene the most popular electrode material for the fabrication of high-performance EDLCs [22, 23]. Although from the performance point of view, many promising results have been reported by researchers worldwide, a study by A. Kauling and

C. Neto in 2018 revealed that the production of high-quality graphene is still challenging and a matter of debate[24].

Bipolar electrochemistry (BPE) is a novel approach for the fabrication and deposition of high-quality graphene. BPE was around for many years, and in the 1960s, it has been extensively used to apply a wireless potential to discrete conductive particles [25, 26]. Fabrication of 2D materials by BPE method was done for the first time in 2016 by A. Allagui. Since then, this method has been employed in the fabrication and deposition of different 2D materials such as graphene and phosphorene [6, 27-30].

2.2 Electrochemical Supercapacitors

Electrochemical capacitors (ECs), also known as supercapacitors, have received increasing attention from the scientific and engineering community according to their unique properties such as exceptional power performance (~10 kW kg^{-1}), moderate specific energy (~5 Wh kg^{-1}), excellent cycle life, and durability in harsh situations. These properties can bridge the gap between batteries and conventional electrolytic capacitors. Figure 2-1 shows the specific energy versus specific power (so-called Ragon plot) of ECs compared to other energy storage devices [31-34].

Based on the mechanism by which ECs store energy, they can be classified into three categories. (1) Electrochemical double-layer capacitors (EDLCs) which physically store charge in the double-layer formed at electrolyte/electrode interface. (2) Pseudocapacitive devices that store charge based on highly reversible and fast faradaic reactions. (3) Hybrid

capacitors, which comprised combined mechanisms from both EDLCs and pseudocapacitors [23, 31, 34].

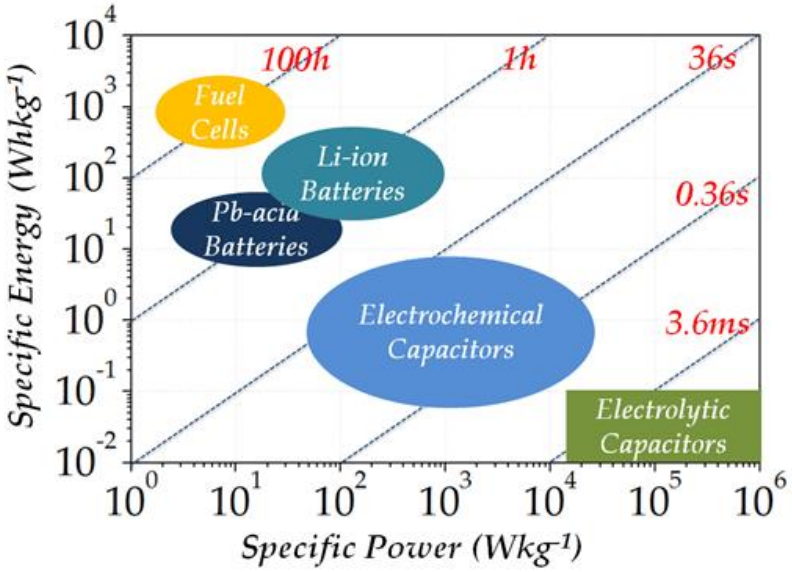

Figure 2-1. The plot of specific energy versus specific power density for different energy storage devices [1].

2.2.1 Electrochemical Double-layer Capacitors

In this group of supercapacitors, the charges accumulate on the surface of conductive electrodes where ions with the opposite charge are arranged close to the electrode surface in the electrolyte. The formed double layer by these two opposite charged species at electrolyte – electrode interface is called Helmholtz layer. Figure 2-2 schematically shows the formation of Helmholtz layer on the electrode-electrolyte interface [31, 34]. The thickness of Helmholtz layer and the electrode's surface area are the primary factors that control the performance of EDLCs. Typically the capacitance of EDLCs is about two orders of magnitude higher than electrolytic capacitors. Porous materials (including activated carbon, carbon nanotubes (CNTs), carbon nanofibers, graphene, MXene, etc.)

with very large specific surface areas have been extensively used as EDLCs' electrode material to achieve such a high performance [35-37].

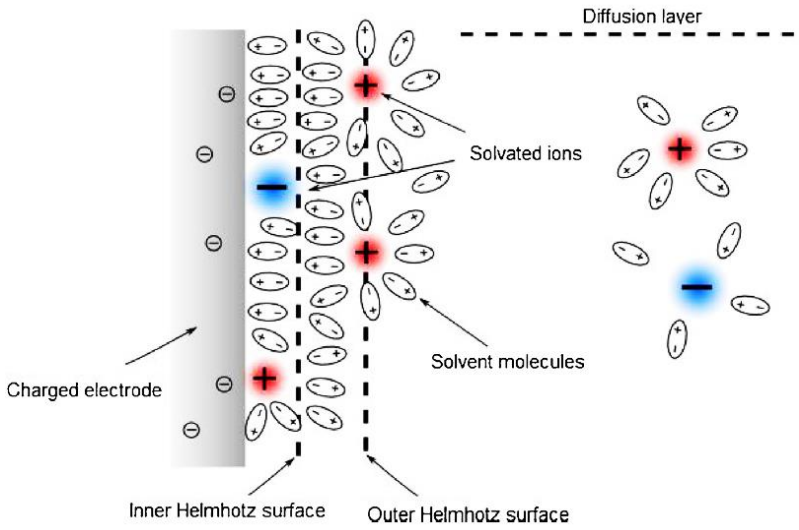

Figure 2-2 A schematic that shows the formation of Helmholtz double layer at the electrode-electrolyte interface [31].

2.2.2 Pseudocapacitors

Fundamental of this group of supercapacitors are similar to both batteries and EDLCs since a fast and highly reversible faradaic reaction is responsible for storing the charge. In other words, the electrons are transferring between the electrode and electrolyte and react with adsorbed ions in the solution. Although similar to batteries, the redox reactions occur during charge/discharge; the device behaves like capacitors since the reactions are very fast and reversible. However, due to the multi-step process of storing the charge, the capacitance of pseudocapacitors is usually significantly higher than EDLCs [1, 37]. The most widely used materials for fabrication of pseudocapacitors include conducting polymers (such as polypyrrole (PPY), polyaniline (PANI), polythiophene (PTH) and their

derivatives) and metal oxides (such as manganese oxide, ruthenium oxide, and nickel hydroxide) [1, 20, 37].

2.2.3 Hybrid Supercapacitors

As it can be understood from their name, both double layer and pseudocapacitive mechanisms are incorporating in the hybrid supercapacitors. This incorporation can be done based on either device configuration or material design. In the former type, one of the electrodes of the hybrid supercapacitor works based on double-layer capacitors, where the other one relies on the pseudocapacitive mechanism. On the other hand, the later type comprises composite electrodes, which means each electrode by itself containing a harmonious amalgamation of double layer and pseudocapacitive charge storage mechanisms.

2.3 Miniaturization of Supercapacitors

With the recent developments in the fabrication of microelectronic devices, miniaturized and portable electronics, microelectromechanical systems and their integrated microsystems, it is imperative to fabricate embedded micro-sized energy storage systems that can be directly integrated with other microelectronic compounds [16, 23, 38, 39]. Kim et al., for the first time, introduced the concept of microsupercapacitors (MSCs) in 2002 [40]. MSCs can be used as micro-energy storage devices to fill the gap between electrolytic capacitors and micro-batteries. Moreover, they can also be used for filtering applications, making them a promising alternative to the bulky electrolytic capacitors for on-chip

applications [9-15]. In addition, quite akin to the macro supercapacitors, MSCs can also be connected in parallel and/or in series to meet the required capacity, voltage, and current depending on the defined application [41].

From the fabrication and configuration point of view, MSCs can be classified into three sub-categories: (i) Fiber shaped structure, (ii) thin-film electrodes, (iii) planar interdigitated structure. Among these three, the last one is the most popular one due to the following advantages. First, this design does not need a separator, and the distances between the two electrode sides are very small; therefore, the ion transport resistance decreases, which increases the response frequency and power density of supercapacitors. Second, the interdigitated electrodes provide vast open edges and increase the contact area of the electrode materials and electrolyte, which leads to the improvement of the device's electrochemical performance. Third, the fabrication of in-plane MSCs is compatible with the on-chip micromanufacturing process, and the MSCs fabrication could directly be integrated with the fabrication of other components of Micro-Electro-Mechanical Systems (MEMS) [12, 23, 35, 42].

2.4 **Frequency Response of Supercapacitors**

In modern electronics, elimination of voltage fluctuations is necessary, specifically in AC (alternating current) to DC (direct current) converter devices. Since now, many different circuits have been designed and manufactured for these purposes. A brief look at this subject will show that high-frequency capacitors play an important role in any type of these

converters. Aluminum electrolytic capacitors (AECs) are the only commercialized group of capacitors that can provide high capacities and also can work at high frequencies. However, the replacement of these traditional capacitors that have bulky sizes and large equivalent series resistance is strongly demanded. Recently, some promising studies have been done to produce fast EDLCs that improved the probability of replacing AECs with EDLCs in the future. Among all types of supercapacitors, the graphene-based EDLCs showed the most promising behavior for being used at high frequencies [43, 44].

In [33], Miller demonstrated how using vertically aligned active electrode materials can minimize the electric and ionic resistance of the supercapacitors and increase their response rate. Up to now, a variety of methods have been employed to fabricate vertically aligned graphene for energy storage applications. Different types of plasma-enhanced chemical vapor deposition (CVD) (i.e., radiofrequency plasma-enhanced CVD, electron cyclotron resonance-plasma enhanced CVD, and microwave plasma-enhanced CVD) are the most successful techniques that have been employed for this purpose. However, the CVD technique is quite challenging for the fabrication of miniaturized MSCs, and all of these studies were focused on centimeter-sized devices. Moreover, the complexity and associated costs of the CVD method do not justify their scaling-up for commercial manufacturing [34, 43-50]. Thermal decomposition of SiC is another approach that has been used to fabricate vertically aligned graphene. However, the temperature needed for this process is 1600°C which makes serious challenges for scale-up fabrication through this method [47].

2.5 **Fabrication of Graphene**

Since its discovery by the scotch tape method [22, 51], graphene, which is comprised of a single, two-dimensional layer of sp^2-bonded carbon atoms arranged in a hexagonal lattice, has attracted growing interest due to its unique properties such as high surface area, high thermal conductivity, high charge carrier mobility, high optical transparency, broad electrochemical window and unconventional superconductivity [52, 53]. Many approaches have been demonstrated to produce graphene-based materials. The most popular ones are shown in Figure 2-3 and will be discussed briefly in the following. It should be noted that bipolar electrochemistry (BPE) has been recently introduced as a novel approach for the fabrication of graphene, which has not been shown in this figure and will be discussed later in section 2.6.

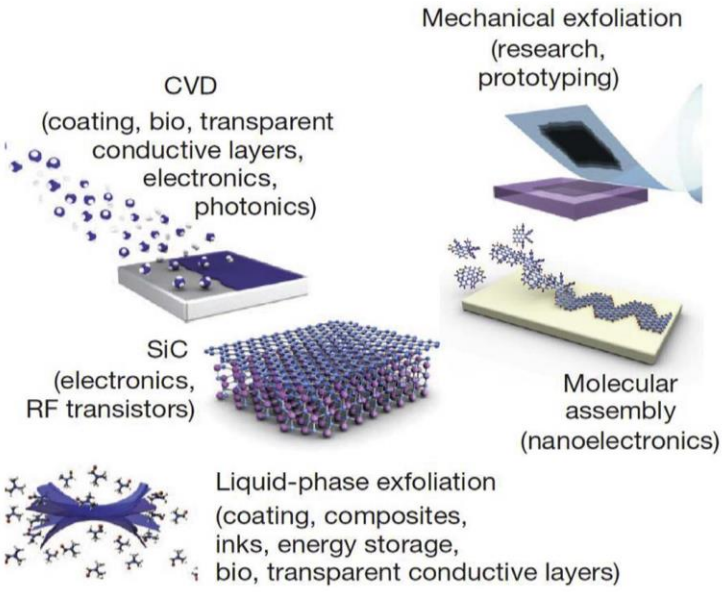

Figure 2-3. Different approaches in the production of graphene-based materials due to the application and required properties [54].

2.5.1 Mechanical Exfoliation

The first and simplest method for the fabrication of graphene is the direct mechanical exfoliation of graphite with adhesive tape [22]. The method is categorized as a top-down method, and the fabrication needs an external force of ~300 nN μm^{-2} in order to delaminate a single layer of graphene from graphite bulk material [55]. Several techniques can be used for mechanical exfoliation, including scotch tape [22], ultrasonication [56], AFM tip [57], and electrostatic force [58]. Although the quality of graphene fabricated by this method is usually very high, the method is not good in terms of repeatability. Also, it is not possible to scale up this method for industrial use [24, 55].

2.5.2 Chemical Vapor Deposition

In this method, a substrate exposes to a mixture of hydrocarbon gases, and as a result of a controlled process, the graphene forms and deposits on the substrate's surface. Some modifications such as using plasma-assisted chemical vapor deposition (CVD) process have also been successfully utilized to decrease the process temperature and increase the products' efficiency and quality [55]. Therefore, CVD became the most popular technique to create a continuous and thin film of high-quality graphene [59-61]. The source of carbon in CVD is hydrocarbon gases, and the process usually is done at elevated temperatures under a controlled atmosphere. Therefore, expensive vacuum and heating systems are usually involved, which decreased their popularity in many scale-up applications [59, 62, 63]. As a benchmark, the prices of the CVD equipment start as low as around $80,000 for applying graphene on small substrates and hundreds of thousands for large substrates. Moreover, fabrication of high loading materials is not possible with CVD, and this method

usually finds its application where a single and thin film of graphene is needed, such as the production of displays and touch panels [24, 62, 63].

2.5.3 Chemical Exfoliation and Reduction

Chemical exfoliation is another approach for the large-scale production of graphene-based materials. In this method, graphene-based materials fabricate through the breakdown of a bulk graphite source. In this technique, small ions such as alkali metals intercalate between the graphite sheets. Moreover, oxidation and functionalization of graphite also take place. These phenomena lead to increasing the interlayer spacing of graphite and breaking the van der Waals forces between the graphite layers. Therefore, the material fabricated by this method is highly oxidized (so-called graphene oxide (GO)) and contains various functional groups. One major challenge in this approach is the fabrication of graphene-based devices out of the fabricated GO. For this purpose, two separate steps should be employed. (i) Deposition of GO and assembling the device, (ii) Reducing GO to make the conductive form of graphene (reduced graphene oxide (rGO)) [55, 64].

Hummers method and modified Hummers method are the most well-known examples of chemical exfoliation process which extensively used for the production of GO. In these techniques, strong oxidizing agents like $KMnO_4$, $NaNO_3$, and $KClO_3$ in a strong acidic medium are typically used for the production of GO [65, 66]. In order to reduce the produced GO and fabrication of rGO, strong reducing agents such as hydrazine [67], hydrohalic acid [68], and L-ascorbic acid [69] are usually being used. These sets of reactions could introduce relatively high amounts of defects into the rGO sheets and produce toxic chemicals like ClO_2 and NO_2.

2.5.4 Electrochemical Exfoliation

The electrochemical techniques have been growingly employed in the mass production of graphene with the advantages of high production yield of relatively high purity products in simple and cost-effective ways [70]. As explained in section 2.5.3, the intercalant compounds can intercalate into the space between graphite layers and break their bonds, which results in the fabrication of graphene sheets. The electrochemical process is one of the methods which can force the ions to be adsorbed and intercalated to the graphite electrode. Based on this concept, some researchers used different electrochemical parameters and environments (different ions in the electrolyte) and reported successful exfoliation of graphite and fabrication of graphene nanosheets dispersed in the electrolyte [62, 71]. Figure 2-4 illustrates the electrochemical exfoliation process.

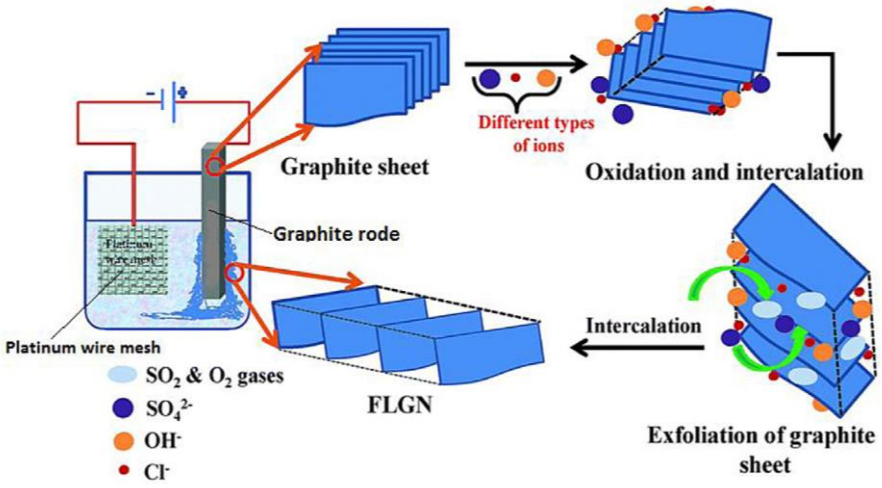

Figure 2-4. Schematic diagram of electrochemical exfoliation of graphite[63].

In most studies on electrochemical exfoliation, the graphite was used as the anode; however, successful exfoliation when graphite was used as the cathode is also reported [72]. Generally, in an electrochemical cell, oxidation and reduction reactions occur at the cathode and anode, respectively. Therefore, the nature of exfoliation is different where the polarity of the graphite is different. Based on the polarity of the graphite during the process, electrochemical exfoliation

method could be divided into two categories: (i) Anodic exfoliation (ii) cathodic exfoliation. Figure 2-5 schematically illustrates how these two mechanisms works and the role of cations and anions in these processes.

In brief, the potential of the graphite working electrode (either positive or negative) attracts oppositely charged intercalating ions and promotes the intercalation. If co-intercalating molecules are also present, their intercalation may also help the exfoliation of graphite. On the one hand, it has been reported that the anodic approach results in higher intercalation efficiency and, consequently, higher yield. On the other hand, the cathodic exfoliation results in the fabrication of higher quality products [53, 72, 73]. In this technique, it is possible to functionalize the fabricated graphene by adding functionalizing agents either during or after the exfoliation process.

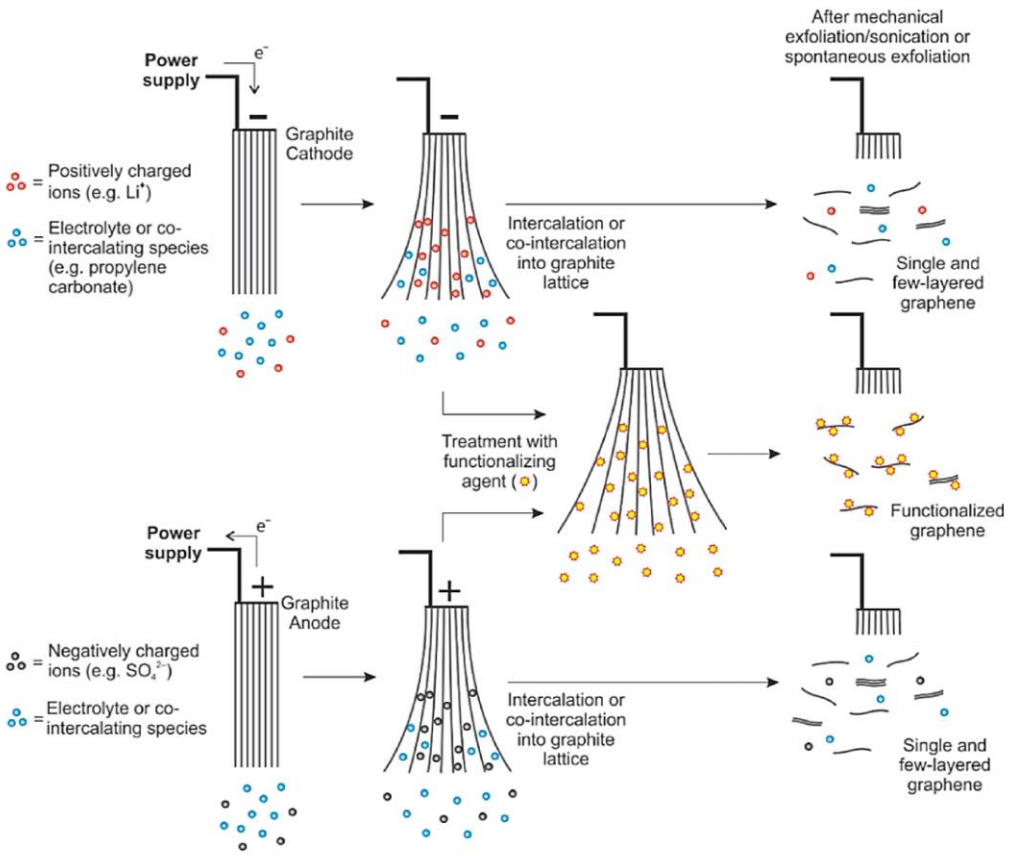

Figure 2-5. Schematic overview of cathodic and anodic exfoliation mechanisms [72].

2.5.5 Challenges in the Scale-up Application of Graphene

In 2018, Kauling et al. analyzed graphene samples from 60 different suppliers worldwide and reported that the quality of the commercially available graphene products is not optimal for applications [74]. It has been found that the majority of commercially available materials are actually graphite microplates with less than 10% graphene content, and none of the products had more than 50% graphene content.

It is worth noting that most of the commercially available graphene products are fabricated through liquid exfoliation approaches (either chemical exfoliation or electrochemical exfoliation). Besides the low quality of these products, further steps are needed to deposit

and reduce GO and fabricating rGO based devices, making the process more complicated and leading to even lower quality of final products [6, 75, 76]. None of the aforementioned methods in sections 2.5.1 to 2.5.4 can spontaneously combine exfoliation, reduction and deposition steps into an straightforward single-step device fabrication process.

2.6 **Bipolar Electrochemistry**

Bipolar electrochemistry (BPE) is a type of electrochemical cell dealing with wirelessly placed conductive objects (so-called bipolar electrode (BE)), which act as mixed electrodes in the presence of an applied electric field. Although the phenomenon of BPE is a well-known and well-established method that has been around for a long time, it attracted growing attention at the beginning of the 1960s when Fleischmann and his co-workers described fluidized bed electrodes. In this concept, a voltage is applied to the feeding electrodes of an electrochemical cell. The electric field in the electrolyte enables electrochemical reactions occurring at the edges of discrete conductive particles that were dispersed in the electrolyte [25, 77]. Since then, BPE found its application in different fields of science, including materials and chemical engineering, dispersing microelectrodes, as well as electrodeposition, electrosynthesis, water splitting, manipulation of dissymmetrical nanostructures, electroanalysis, chemical sensing, microelectronics, micro-objects propulsion, electrodeposition, generation of motion, improving the efficiency of electrosyntheses and photoelectrochemical cells, and fabrication of batteries, polymeric electrolyte membrane, fuel cells, confined nanoparticles, welded micro particles etc. [25, 26, 77-82].

Figure 2-6 shows a typical configuration of bipolar electrochemistry cell. A key point to understand the fundamental of BPE is that the poles of a BE are oriented in the opposite polarity of the feeding electrodes (Figure 2-6 (b)). As the schematic shows, driving (feeding) electrodes apply an electric field across the electrolyte solution. In the case of using a conductive BE, it remains almost isopotential where there is a potential gradient in the background electrolyte. Therefore, the BE experiences a potential difference (δ^+, δ^-) which is maximum at the farthest edges of BE. This voltage gradient in the BE results in the occurrence of faradaic anodic (blue arrow) and cathodic (red arrow) reactions at the two poles of BE. Specifically, the anodic process takes place at one extremity of the BE close to the negative feeding electrode. In contrast, the cathodic reduction takes place at the other extremity, i.e., close to the positive feeding electrode [6, 25, 26]. Therefore, both anodic and cathodic reactions can simultaneously happen on one conductive object. This is the most distinct difference between the BPE method and other standard two- or three-electrode electrochemical cells, where the cathode and the anode are physically separated [25, 26, 81].

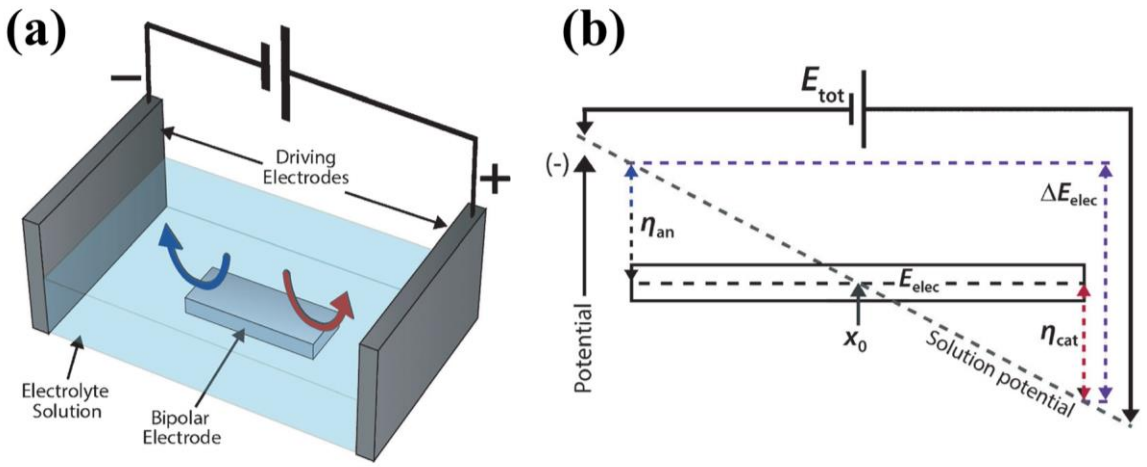

Figure 2-6. (a) A schematic of a bipolar cell and its components. (b) A schematic of the potential gradient in a bipolar cell [82].

2.6.1 Bipolar Electrochemistry for Graphene Fabrication

In 2016, for the first time, fabrication and deposition of reduced graphene oxide on a conductive substrate by bipolar electrochemistry had been reported by Allagui et al. [6, 7]. Their bipolar setup consisted of a graphite rod that was placed equidistantly between the electrodes of a regular electrochemical cell. Figure 2-7 shows the schematic of their setup for the fabrication and deposition of graphene. As illustrated in this schematic, due to the nature of bipolar electrochemistry, oxidation happens on one side of the graphite rod while at the same time on the other side, the reduction happens. This faradaic charge transfer mostly happens by water decomposition reactions. However, intercalation, exfoliation, and oxidation of graphite and graphene oxide formation are other possible reactions. It is worth noting, as explained in section 2.5.4, the exfoliation and production of graphene/graphene oxide nanosheets have been reported by both anodic and cathodic exfoliation process, and in these two studies ([6, 7]), the authors only assumed the anodic exfoliation was contributing in the exfoliation process.

In these studies, the deposited material on the positive driving electrode had been studied by Raman spectroscopy and X-Ray diffraction analysis (XRD) and the formation of partially reduced graphene oxide is confirmed. It has been claimed that the fabricated GO were charged particles, which could electrophoretically move and deposit on the surface of the feeding electrode with opposite polarity [6, 7].

Moreover, the fabricated GO was subjected to a further reduction process (one hour at 900˚C under vacuum). The electrochemical performances of fabricated electrodes before and after this reduction step have been reported. The results proved that the reduction could significantly improve the performance of the fabricated GO, which shows as-deposited graphene was highly oxidized.

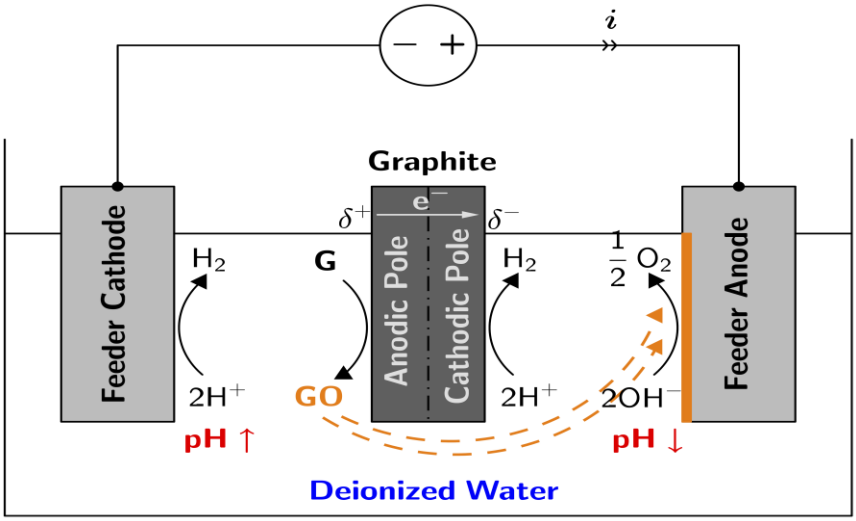

Figure 2-7. Illustration of the bipolar electrochemical cell used for fabrication and deposition of graphene on stainless steel [6].

2.6.2 Bipolar Electrochemistry for the Fabrication of Other 2D Materials

Exfoliation of other 2D materials through the BPE method has also been reported. Pumero and his co-workers reported the exfoliation of hexagonal boron nitride (hBN) [30], tungsten

disulfide (WS_2) [83], and molybdenum diselenide ($MoSe_2$) [84] by BPE. In their method, the BE materials were in the form of dispersed powder in the electrolyte, and a DC voltage was applied to the cell for less than one hour. After the BPE process, they evaluated the collected material from the electrolyte and compared the size of particles in the solution before and after the BPE process and proved that the BPE led to the breaking and exfoliation of particles. However, it is worth noting that because of the following reasons, it seems other factors were caused the exfoliation in their studies rather than bipolar electrochemistry: (i) conductivity of these particles are not high therefore they can not be concidered as bipolar electrodes. (ii) even if the particles were conductive, concidering the small size of particles and reletively low electrical field, the induced interfacial potential was not high enough to activate redox reactions which they proposed as the mechanism of bipolar exfoliation.

In another study by the same group [29], mechanical sonication followed by BPE has been reported to exfoliate black phosphorous into phosphorene nanosheets. TEM and XPS analysis confirmed the successful exfoliation of black phosphorous. A novel single-step BPE approach has been recently used to exfoliate and deposit phosphorene nanosheets on conductive feeding electrodes in DI water [28, 85]. In this study, a 1 cm length black phosphorous was placed between two SS feeding electrodes (the two were 2 cm apart) and a 30 VDC was applied to the system for 24 hours. The water electrolysis and intercalation of H^+ and OH^- ions led to the breaking of weak Van der Walls bonds of black phosphorous layers and the formation of exfoliated phosphorene nanosheets. At the same time, the electrophoresis phenomenon was taking place and resulted in the migration and deposition to the exfoliated nanosheets on the feeding electrodes.

Fabrication of high-quality graphene for different applications is still a matter of debate and has attracted growing interest in recent years. EDLCs are one of the energy storage devices that experienced a revolution when graphene was used as their electrode materials. The unique chemical, physical and electrochemical properties of graphene could improve the capacitance of EDLCs, and it could significantly increase their response frequency when specific microstructures of graphene were used. In this chapter, first we described the concept and clasification of supercapacitors. After that, the specifications and applications of high frequency supercapacitors and microsupercapacitors have been introduced. Then different fabrication methods of graphene as the most popular electrode material for EDLCs has been discussed. At the end, since the focous of this study, was on the fabrication of graphene by BPE, its concept and application for fabrication of 2D materials are presented.

3. Methodology

3.1 Introduction

In this chapter, the methodology adopted in this dissertation for materials synthesis, supercapacitors assembly, microdevice fabrication, as well as materials and electrochemical characterization is provided. The graphene synthesis was conducted through a modified bipolar electrochemistry technique. Swagelok cell was employed to assemble the macro supercapacitors. A modified photolithography method was developed to fabricate microdevices, and all the developed materials were evaluated by different electrochemical and materials characterization techniques.

3.2 Bipolar Electrochemical Exfoliation

In this study, materials synthesis was conducted by the bipolar electrochemistry (BPE) technique. Figure 3-1 (a) shows the schematic of the bipolar cell that was designed for the three-in-one exfoliation, deposition and reduction of graphene on conductive substrates. Unlike the conventional bipolar setup [6, 25, 26], in this study, two pieces of bipolar electrodes were electrically connected by an external wire. This modification enabled the author to monitor the amount of current that passes through the bipolar electrodes. Two 316 stainless steel electrodes with an active area of 2×1 cm^2, placed 9 cm apart in DI water as the feeding electrodes. The distance between the farthest edges of bipolar electrodes was 7 cm. The electrolyte of the cell was deionized (DI) water (Resistivity of 18 MΩ.cm and pH of 6.3). A N6705A DC Power Analyzer device was used to provide and record both

voltage and total current of the bipolar cell. Another channel of the device is also used to record the current passing through the bipolar electrodes.

The electric field in the cell depends on the applied potential (V) and the distance between the feeding electrodes (L). The value for the experiments in this dissertation is 5 V cm^{-1} ($^{45V}/_{9cm}$). Due to the basics of bipolar electrochemistry, in the case of using BE with much higher conductivity compared to that of the electrolyte, BE remains almost isopotential, and the electric field produces interfacial potential differences (δ^+, δ^-) between the BE and the electrolyte leading to the polarization of the BE edges. The interfacial potential difference depends on the length of BE and the electric field in the electrolyte. The calculated value for the experiments in this dissertation is 35 V ($5V.cm^{-1} \times 7cm$). The actual voltage measurement between the Pt and the graphite was around of 33 to 34 V. It should be noted that this apparent voltage is high enough to enable the electrochemical exfoliation of graphite and water electrolysis, resulting in the reduction of ions and oxidation of ions at the cathodic and anodic poles of the BE, respectively [5, 6, 53].

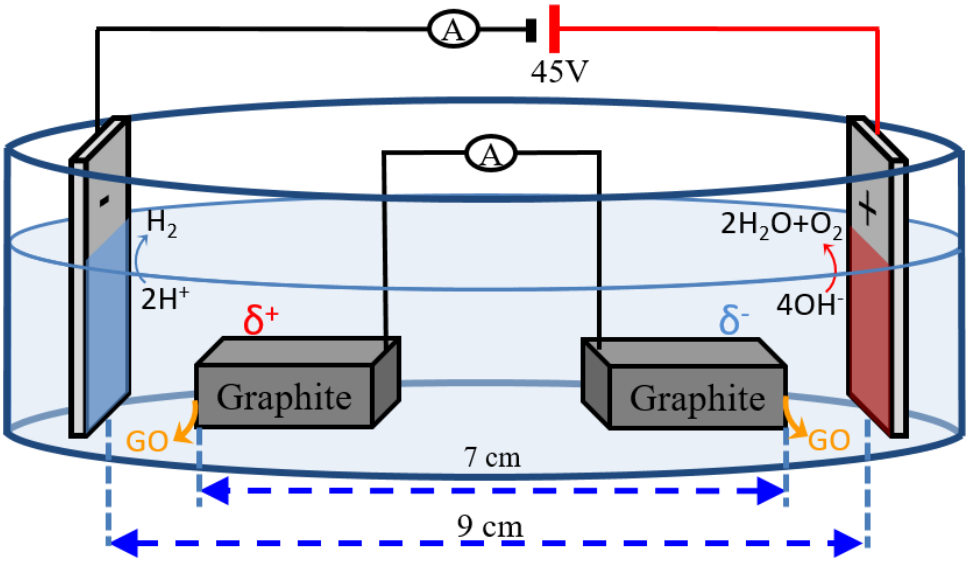

Figure 3-1: Schematic illustration of bipolar electrochemistry cell.

3.3 Microfabrication

The fabrication of gold interdigitated micro current collector was conducted by a modified photolithography process. Figure 3-2 schematically depicting the current collector fabrication process, which consists of the following steps:

1- A 4" Si/SiN (100) wafer was first spun coated by HMDS and then by AZ 1518 at a speed of 2900 rpm for 35 s.

2- Soft baking of the wafer was conducted for 60 s at a temperature of 100°C on a hot plate.

3- The wafer was then patterned by an OAI 800 mask aligner with a UV dose of 60 mJ cm^{-2}.

4- After the exposure step, the development of the photoresist was carried out using diluted AZ 400 MIF (4:1 volume ratio of DI water to the developer) for ~60 s.

5- The wafer was baked for 20 s at 65°C and 70 s at 115°C.

6- After hard bake, O_2 plasma cleaning was done by reactive ion etching (RIE) at 100-watt power for 60 s.

7- Then, e-beam evaporation was used for metallization of the wafer with Cr/Au (20/100 nm) using a CHA evaporator.

8- Lift-off in bath sonication was carried out using AZ EBR for 2 hours, followed by acetone and isopropyl alcohol rinsing and N_2 drying.

9- To avoid the lateral growth and deposition of graphene on the space between the microelectrodes, a sacrificial photoresist layer was deposited between the metallic

fingers. This process was carried out by repeating steps 1 to 5 on the wafer with fabricated gold microelectrodes.

Accordingly, the final product consisted of an interdigitated gold current collector (with a thickness of ~120 nm), with ~2 μm of AZ1518 photoresist patterned between the gold fingers. There are 32 interdigital fingers on each MEMS (16 for each electrode side) with length and width of 6040 μm and 100 μm, respectively.

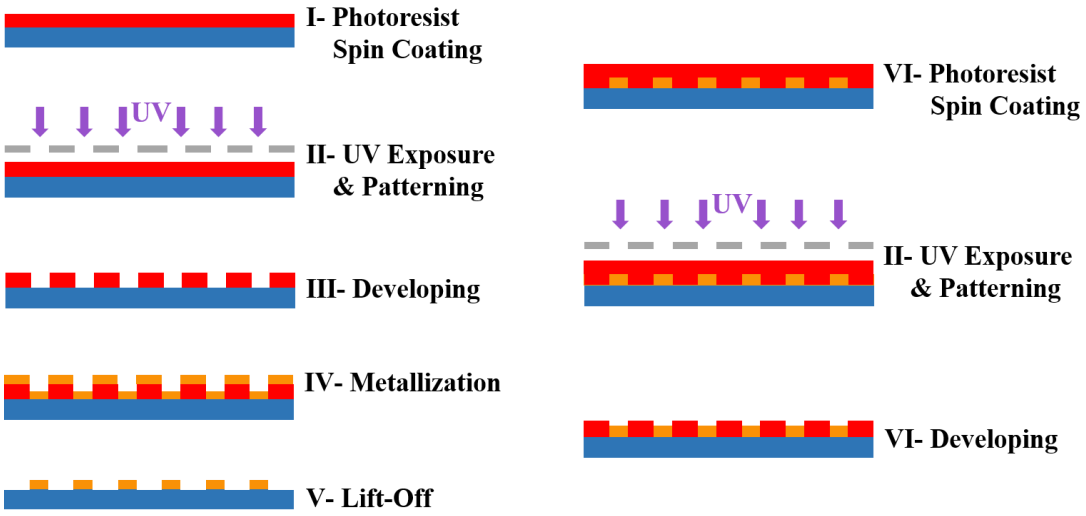

Figure 3-2: Illustration of the fabrication process of the interdigitated MEMS substrate.

3.4 Materials Characterization

The techniques employed in this dissertation for characterization of the materials are described in this section:

3.4.1 Scanning Electron Microscopy

Field-emission scanning electron microscopy (SEM) (JEOL 6330FE-SEM and JEOL FESEM 7000) has been used for evaluating the microstructure and morphology of

synthesized materials. The acceleration voltage was set from 5 to 15 kV with a working distance of 3 to 40 mm.

3.4.2 Transmission Electron Microscopy

Transmission electron microscopy (TEM) has been used to study the crystal structure and interlayer distance of graphene layers. High-resolution electron micrographs and selected-area electron diffraction (SAED) patterns of the deposited materials were obtained using a Philips CM-200 FEG TEM at an accelerating voltage of 200 kV using a field emission gun with a resolution of 2 °A. For sample preparation, a copper mesh was attached to the negative feeding electrode of the bipolar cell for 12 hours.

3.4.3 X-Ray Diffraction

In this dissertation, the crystallinity and the interlayer distance of graphene-based materials have been investigated by X-Ray diffraction (XRD) analysis. A Siemens D-5000 diffractometer with copper anode (Cu Kα, λ=0.154056 nm) was used for this purpose at the X-Ray source voltage and current of 40 kV and 40 mA, respectively.

3.4.4 Raman Spectroscopy

Raman spectroscopy is a versatile method to study the quality and defect proportion in the structure of graphene-based materials. This characterization method works based on the change of the vibrational quantum states of illuminated Raman active materials. The interaction of laser with the vibration of molecules results in a cheng to the energy of the light. Therefore a shift will be detected from the backscattered light, which gives information about the chemical bonds and vibrational mode of the chemical species. In this

dissertation, Raman scattering measurements were performed in the backscattering configuration using an argon-ion laser source (Spectra Physics Model 177, 514 nm, 400mW) and HoloSpec f/l.8i, Kaiser optical spectrograph.

3.4.5 Fourier Transform Infrared Spectroscopy

Fourier transform infrared (FTIR) spectroscopy is an accurate and quick method to obtain the infrared spectrum of the materials in a wide range of wavelengths. In this method, the sample is subjected to infrared light, and the absorbance or emission of the light will be evaluated. Each type of chemical bond absorbs a specific frequency of infrared light (depends on the chemical bond's energy) which will be reflected as a peak in the final spectra. Therefore, the method can be used to study the materials' molecular composition. In this dissertation, a JASCO FTIR-4100 equipped with an attenuated total reflectance (ATR) accessory between 500-4000 cm^{-1} was used to analyze the synthesized graphene-based materials.

3.4.6 X-ray Photoelectron Spectroscopy

X-ray photoelectron spectroscopy (XPS) is a quantitative spectroscopic technique that can analyze the surface elemental composition of materials. The method can be used for depth profiling or in-line profiling of the samples' chemical composition.

In this method, the sample is irradiated to the X-Ray beam, and the number of excreted electrons in addition to their energies are counted and recorded. The energy of the electrons is the fingerprint of chemical bonds, and the number of detected electrons can reveals the concentration of the chemical bonds. In this dissertation, a Physical Electronics 5400 ESCA instrument with Al Ka radiation (1486.6 eV) was employed for the XPS analyses.

3.5 Electrochemical Characterization

3.5.1 Cyclic Voltammetry

Cyclic voltammetry (CV) is a potentiodynamic electrochemical method that can be used in the study of the thermodynamics and reversibility of electrochemical reactions in addition to the calculation of the diffusion coefficient of ions and calculation of electrochemical capacitance of energy storage devices. In the first stage of CV test, the potential is swept to one direction (either anodic or cathodic) at a predefined constant scan rate (V/s) up to a predefined voltage; then, it is swept to the reversed direction at the same scan rate up to another predefined voltage. After that, the process is repeated for certain cycles. In this technique, the current is recorded as the response, and the results are plotted in a voltammogram graph which is the plot of current versus potential. Equation 3-1 can be used to calculate the capacitance of the EDLCs from the CV curves. In this equation, C, v , ΔV, i, and V are the device capacity, voltage scan rate, voltage window, measured current, and applied voltage, respectively. In this dissertation, CV tests were performed at room temperature using a VMP3 multichannel potentiostat (VMP3, Bio Logic, Knoxville, TN, USA) System.

$$C = \frac{1}{2v\Delta V}\int i(V)dV \qquad \text{Equation 3-1}$$

3.5.2 Galvanostatic Charge-discharge

Galvanostatic charge-discharge (GCD) is an electrochemical analysis to study the capacity and cyclability of the energy storage devices at different currents. A predefined constant

positive current is applied to the electrochemical cell in the charging step until reaching a predefined voltage. In the discharge step, the current is reversed (negative current) until the potential drop to another predefined voltage. Thus, the device's performance can be defined in a plot of the cell's potential (v) vs. time (s). The cyclability test can be conducted by repeating the charge-discharge cycles and comparing the device's performance at different cycle numbers. Equation 3-2 has been used to calculate the average discharge capacity of the capacitors at different current densities. In this equation, ΔV is the voltage window, which was 0.8 V for the experiments in this dissertation, and i_{dc} is the discharge current density. In this dissertation, GCD tests were performed at room temperature using a VMP3 multichannel potentiostat (VMP3, Bio Logic, Knoxville, TN, USA) System.

$$C = \frac{1}{\Delta V} \int i_{dc} dt \qquad \text{Equation 3-2}$$

3.5.3 Electrochemical Impedance Spectroscopy

Electrochemical impedance spectroscopy (EIS) has been used to study the frequency response of the supercapacitors. In this method, a sinusoidal potential (with small amplitudes in the order of some millivolts) is applied to the electrochemical system, and the current is measured as the response. The real and imaginary parts of the impedance can be calculated based on the current amplitude and the phase difference between the applied voltage and measured current. EIS is known as the most common method to study and evaluate the performance of capacitors at higher frequencies. A short description of the terms and parameters that have been used to assess the supercapacitors' performance is given in the following [86].

Phase angle at desire frequency: A device will behave like a pure capacitor as long as its phase angle is equal to -90°. All the commercial capacitors have some deviations from an ideal capacitor, and their phase angle is a function of their working frequency. So, the phase angle of the cell at any frequency can show the deviation of the device from ideal capacitance behavior. Plotting the Bode diagram (phase angle (ϕ) vs. frequency (f)) can directly present this characteristic of the supercapacitors.

Cut-off Frequency (f_0): The frequency at which the impedance phase angle reaches −45°. This is the frequency defining the boundary between the capacitive and the resistive behavior of the cell.

Relaxation time constant (τ_0): The minimum time which the device needs for discharging half of its maximum energy. This time can be calculated by inversing the cut-off frequency ($\tau_0 = {}^{1}/_{f_0}$).

In this dissertation, EIS analysis was performed to study the performance of supercapacitors using a VMP3 multichannel potentiostat (VMP3, Bio Logic, Knoxville, TN, USA) System.

4. Bipolar Exfoliation and In-situ Deposition of High-Quality Graphene for Supercapacitor Application

4.1 Introduction

Since its discovery by the scotch tape method [51], graphene, which is comprised of a single, two dimensional layer of sp^2-bonded carbon atoms arranged in a hexagonal lattice, has attracted an growing interest due to its unique properties such as high surface area, high thermal conductivity, high charge carrier mobility, high optical transparency, broad electrochemical window and unconventional superconductivity [52, 53]. Many approaches have been demonstrated to produce graphene-based materials, which can be divided into top-down and bottom-up approaches [87]. The top-down methods involve breaking the stacked layers of graphene in graphite into single or multi-layer graphene sheets, whereas the bottom-up methods consist of arranging carbon atoms on a substrate yielding the formation of two dimensional carbon structures [88]. The production of high-quality graphene has been reported by means of bottom-up approaches like chemical vapor deposition and epitaxial growth of graphene. However, expensive vacuum and heating systems are usually involved which decreased their popularity in many scale-up applications [62, 63].

Up to now, the commercially-available graphene/graphene oxide (GO) materials are mostly produced based on top-down wet chemical and/or electrochemical approaches for (i) exfoliation of GO from graphite sources and (ii) reduction of exfoliated GO into graphene or reduced graphene oxide (rGO) [63, 89]. In the wet chemical processes such as

Hummers method and modified Hummers method strong oxidizing agents like $KMnO_4$, $NaNO_3$, and $KClO_3$ in a strong acidic medium are typically used for the production of GO[65, 66]and strong reducing agents such as hydrazine[67], hydrohalic acid[68], and L-ascorbic acid [69]are typically used for the formation of rGO. These sets of reactions could introduce relatively high amounts of defects into the rGO sheets and produce toxic chemicals like ClO_2 and NO_2. Kauling et al. analyzed graphene samples from 60 different suppliers worldwide and reported that the quality of the graphene produced today is not optimal for applications [74]. The majority of commercially-available materials are actually graphite microplates with less than 10% graphene content, and none of the samples had more than 50% graphene content. On the other hand, the electrochemical techniques have been growingly employed in graphene mass production with the advantages of high production yield of relatively high purity products in simple and cost-effective ways [70]. The electrochemical approaches are typically based on intercalating molecules or charged ions (i.e., anionic or cationic species) between the graphene layers of a graphite electrode to facilitate the exfoliation and collection of the graphene nanosheets from the solution [71]. Although the anodic approach is more common due to the higher efficiency of intercalation and expansion, the cathodic exfoliation is more desired in order to avoid unwanted chemical functionalization and damage to the graphite basal plane that occur during the anodic exfoliation [53, 72, 73]. Nevertheless, while all these top-down approaches can successfully produce GO from graphite which necessitate then further steps of reduction or reduction/deposition of GO to form rGO [6, 75, 76], none of them can spontaneously combine exfoliation, reduction and deposition in a single step and in an environmental friendly manner to form directly functional graphene-based electrodes.

Recently, Allagui et al. reported an unconventional deposition approach to exfoliate and partially reduced graphene oxide using bipolar electrochemistry (BPE) method[6, 7]. The bipolar electrochemical cell consisted of a graphite rod that was placed equidistantly between two feeding electrodes in a low conductivity solution. The formation and deposition of partially reduced graphene oxide on the positive feeding electrode were achieved with promising areal capacitance of 55 μF cm^{-2} at a scan rate of 10 mV s^{-1} [6, 7]. BPE has been around since 1960s and refers to an approach to generate asymmetric reactions on a conductive object in a wireless fashion. BPE found many applications in electrosynthesis and microanalysis due to its advantages of low cost, ease of operation and simple instrumentation [25, 26]. Since in the BPE, oxidation occurs on one side of the conductive subject, while the reduction occurs simultaneously on the other side [25, 26, 90], it deserves to further examine any possible material formation on the negative feeding electrode.

In this study, a modified BPE approach was developed to exfoliate a graphite source electrode and deposit a few-layer graphene materials on conductive substrates. Material characterization confirmed the successful exfoliation and deposition of GO and rGO on the positive and negative electrodes, respectively. The electrochemical performance of the electrodes showed a specific capacitance of 1.932 mF cm^{-2} and a cutoff frequency at -45 deg. impedance angle of 1820 Hz which is adaptable for AC line filters. The results demonstrate the promising feasibility and scalability of our three-in-one approach for in-situ exfoliation, reduction and deposition of high surface area rGO with outstanding electrochemical performance.

4.2 Materials and Methods

4.2.1 Synthesis Process

Graphite rods (3cm in length and 6.15mm in diameter, Ultra "F" Purity 99.9995%) was purchased from Alfa Aesar. Two 2×1 cm^2 316 stainless steel electrodes, placed 9 cm apart in deionized water, were used as the feeding electrodes for bipolar electrochemical setup of this study (see Figure 4-1 (a)). Knowing that the ratio of the bipolar current to the total current is equal to the ratio of solution resistance by the sum of solution resistance plus bipolar electrode resistance, a high resistance solution would promote more faradic current through the floating graphite used in this study, which justifies the use of deionized water. A multi-channel Agilent Technologies N6705A DC Power Analyzer is used for applying a DC voltage of 45 V across the stainless steel electrodes for 24 hours, which resulted in an apparent electric field of 5 V cm^{-1}. The applied voltage and current is recorded as a function of time. In order to record the amount of bipolar current, two pieces of graphite rod serving as bipolar electrodes were connected to another channel of the power analyzer at current measuring mode.

To measure the thickness of the deposited rGO film on the negative electrode, a gold-coated glass was used as the feeding electrode. The processing time was increased to 72 hours to have more reliable measurement. The cross-sectional SEM image of the sample tilted by 45° is shown inFigure 4-5.

4.2.2 Material Characterization

Low resolution and high resolution electron micrographs of the deposited materials were obtained using a JEOL SEM 6330 and a Philips CM-200 FEG TEM, respectively. Cu mesh was attached to the negative electrode for 12 hours deposition in order to collect the deposited materials for TEM. The X-ray diffraction patterns were obtained using a Siemens D-5000 diffractometer (with Cu Kα radiation; λ=0.154056 nm). Fourier transform infrared spectroscopy was carried out on a JASCO FT/IR 4100 in order to study the functional groups of materials. Raman scattering measurements were performed in the backscattering configuration using a 514 nm laser source to study the defects and the degree of reduction of the deposited materials. X-ray photoelectron spectroscopy was performed to study the chemical composition of deposited material on negative feeding electrode using a Physical Electronics 5400 ESCA instrument (with Al Kα radiation).

4.2.3 Electrochemical Characterization

The electrochemical characterizations of the materials were carried out in a two-electrode configuration using a VMP3 Bio-Logic multichannel potentiostat. Two symmetrical devices based one on the materials formed on positive feeding electrodes and another on those formed on the negative feeding electrodes were assembled in Swagelok cells. 1 mol L^{-1} Na_2SO_4 solution was used as the electrolyte and Celgards 2400 microporous polypropylene was used as a separator. All the electrochemical parameters were normalized with the geometric footprint area of the electrodes. Time-domain cyclic voltammetry (CV) and galvanostatic charge/discharge (GCD), and frequency-domain electrochemical impedance spectroscopy (EIS) were used to study the electrochemical

properties of the fabricated devices. The spectral impedances of the devices were measured at 0 V DC with 10 mV-amplitude sinusoidal voltage of frequency varying from 1 MHz down to 1 mHz. The CV has been conducted at different scan rates from 2 to 10000 mV s^{-1} in the voltage window of 0 to 0.8 V. Different loading currents from 25 to 500 μA cm^{-2} were used in the GCD analysis.

4.3 Results and Discussion

4.3.1 Bipolar Electrochemical Exfoliation

Figure 4-1 (a) shows a schematic of the bipolar electrochemical cell that was designed for a three-in-one deposition of rGO on a conductive substrate. Unlike the conventional bipolar setup [6, 25, 26], in this study, two wired pieces of graphite were used in order to monitor the amount of current that passes through the bipolar electrode. Upon the application of the dc voltage across the stainless steel feeding electrodes, several electrical processes take place which can be discussed from the equivalent circuit shown in Figure 4-1 (b). The resistances between the two feeding electrodes are the resistance of the bipolar path (1), and the resistance of the solution path (2) (non-bipolar path), which are in parallel. The resistances of the bipolar path (1) consist of the charge transfer resistance $R_{C/S}$ of the surface reactions at the cathode feeding electrode, charge transfer resistance $R_{A/S}$ between anode feeding electrode and solution, charge transfer resistances $R_{G/S}$ and $R_{S/G}$ which are related to partially negative side of the bipolar electrode and partially positive side of the bipolar electrode, respectively, as well as R_{S1} and R_{S2} which are the solution resistances between feeding electrodes and two pieces of graphite. The solution resistance R_{S3} is the

resistance between the two stainless steel feeding electrodes. All these solution resistances, R_{S1}, $R_{S2,}$ and R_{S3}, should be proportional to the distance between the electrodes after the BPE is stabilized. Therefore, R_{S1} and R_{S2} should be 9 times smaller than R_{S3} according to the cell design. Compared to the above resistances, R_A, which is the sum of resistances of both bipolar electrodes, wirings and the amperemeter, is negligible. The total current flowing through the cell (Figure 4-1 (c)) is the sum of the currents passing through the bipolar path (1) and solution path (2). For the first two hours, the increase of currents of the path (1) and path (2) is most likely due to surface activation and nucleation. The total and bipolar currents increased with time while the current of the path (2) remained almost constant after the initial 2 hours. This demonstrates that in the growth stage the increase in the bipolar current caused the increase in the total current which can be explained as follows. Since the current of solution path (2) is a function of $R_{A/S}$, R_{S3}, and $R_{C/S}$ and it did not change with time, these resistances are most likely constant in the growth stage. In addition, because R_{S1} and R_{S2} are proportional to R_{S3}, we can consider that R_{S1} and R_{S2} remain also constant in the growth stage. Thus, the increase of the bipolar current with time in growth stage indicates that the sum of $R_{S/G}$+$R_{G/S}$ decreases with time given that R_A is negligible. These two charge transfer resistances are related to reactions that happen on the farthest points of the bipolar electrodes which are subjected to 35 V apparent potential difference (which is proportional to the distance) [6, 26]. These reactions are the oxidation and reduction of water, and exfoliation of graphite. Assuming the kinetic of water electrolysis to be stable with time, in growth stage the increase in bipolar current could be attributed to the acceleration of the exfoliation process. Since the conductivity of the

solution was not increased with time, corrosion induced ionic dissolution of the stainless steel feeding electrodes is very negligible.

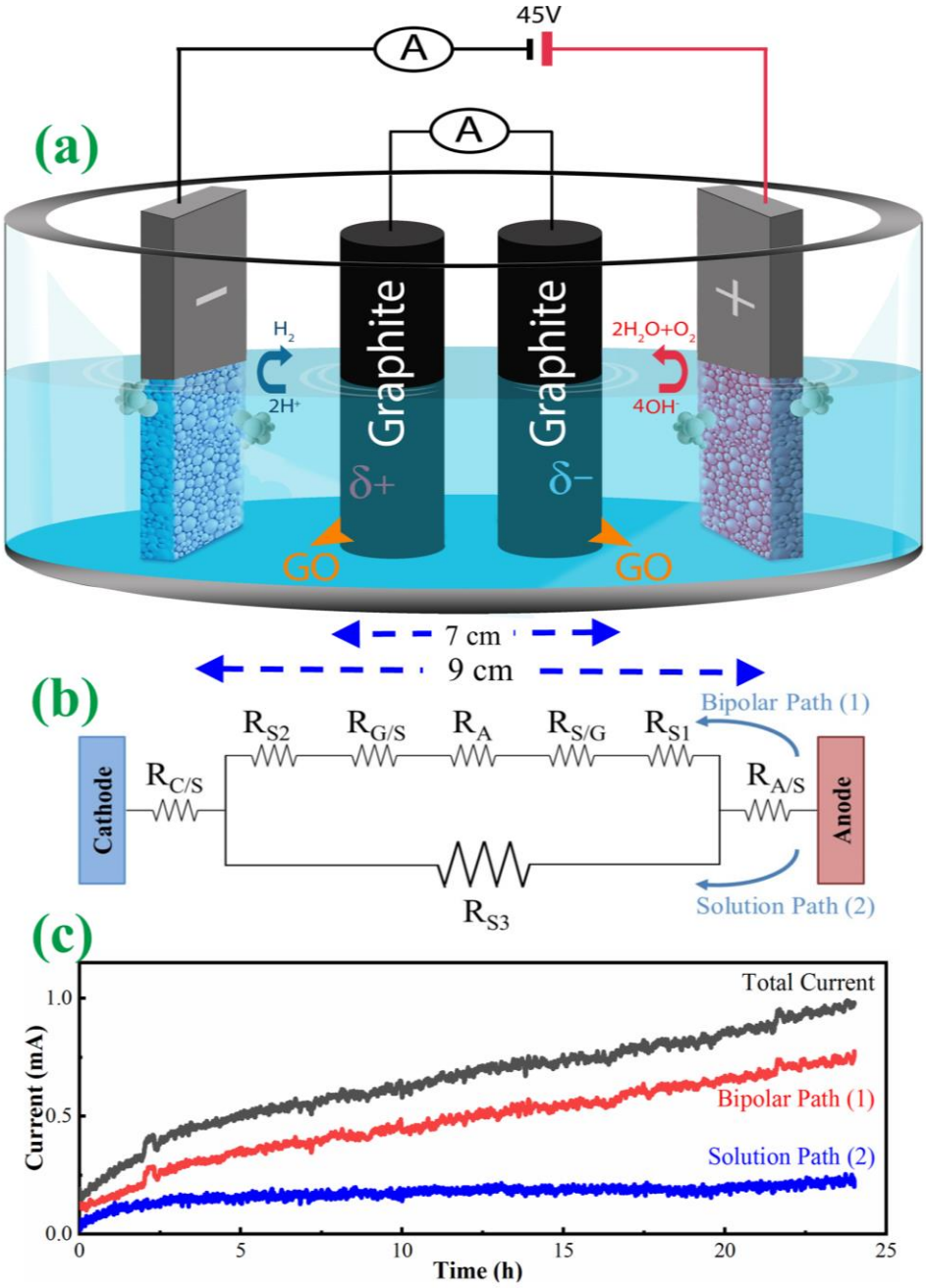

Figure 4-1. (a) Schematic of the bipolar electrochemical setup. (b) Equivalent resistance circuit of the cell. The resistances $R_{C/S}$, $R_{A/S}$, $R_{G/S}$, and $R_{S/G}$ represent the charge transfer resistances of the surface reactions at the cathode feeding electrode, anode feeding electrode, partially negative side

of the bipolar electrode, and partially positive side of the bipolar electrode, respectively. R_A is the sum of resistances of both bipolar electrodes, wirings, and the amperemeter, which is negligible. R_{S1}, R_{S2}, and R_{S3} denote the solution resistances between the stainless steel anode and bipolar graphite, bipolar graphite and stainless steel cathode, and between the two stainless steel electrodes, respectively. (c) Change of total current, bipolar current (path 1) and solution current (path 2, calculated by subtracting the bipolar current from the total current) as a function of time during the bipolar electrochemical process.

After deposition, a thick film on the positive electrode and a thin film on the negative electrode can be visualized. The deposition of graphene on the positive electrode by means of bipolar electrochemistry of carbon has been confirmed in previous studies [6, 7]. However, the deposition on the negative electrode has not been reported yet.

4.3.2 Materials Characterization

Fourier transform infrared spectroscopy (FTIR) technique was performed to study the functional groups of the samples deposited on both positive and negative stainless steel electrodes. The results are depicted in Figure 4-2 (a). The broad absorption peak around 3340 cm^{-1} for the positive SS electrode signals the presence of hydroxyl groups [91, 92]. The other significant peaks for the positive electrode were detected at 1600 cm^{-1} and 1430 cm^{-1} which are attributed to aromatic C=C stretching and C-H bending, respectively[91, 92]. The peaks at around 1330 cm^{-1} and 1040 cm^{-1} are ascribed to C-O stretching bands[93]. The presence of these functional groups shows that the deposited material is mostly GO. In contrast, there are less functional groups in the FTIR spectrum for the negative electrode in terms of peak numbers and intensities, indicating the level of oxidation for the material on the negative electrode is lower compared to the positive one. X-ray photoelectron spectroscopy (XPS) was also performed in order to study the chemical composition and

bonding structure of formed materials. The C1s peak can be fitted into three peaks which are sp2 (284.5 eV) bonded carbon, sp3 (285.4 eV) bonded carbon, carbonyl (C=O) functional group (287.7 eV) (Figure 4-3). The area of C=O peak is about 16.5 % out of the total area of C1s.

Further analysis of the materials was carried out by means of Raman spectroscopy as shown in Figure 4-2 (b). Prominent Raman peaks, typical for graphene-based materials, were detected in both samples: i.e. D-band centered at around 1350 cm^{-1}, G-band at around 1609 cm^{-1}, D+G peak around 2910 cm^{-1}, and 2G-band at around 3200 cm^{-1}. The spectra also reveal that the ratio I_D/I_G obtained from the positive electrode is almost 60% higher than the one from the negative electrode, which means that the graphene on the negative electrode has less structural defects and is in a more reduced state when compared to the graphene on the positive electrode [63, 94, 95].

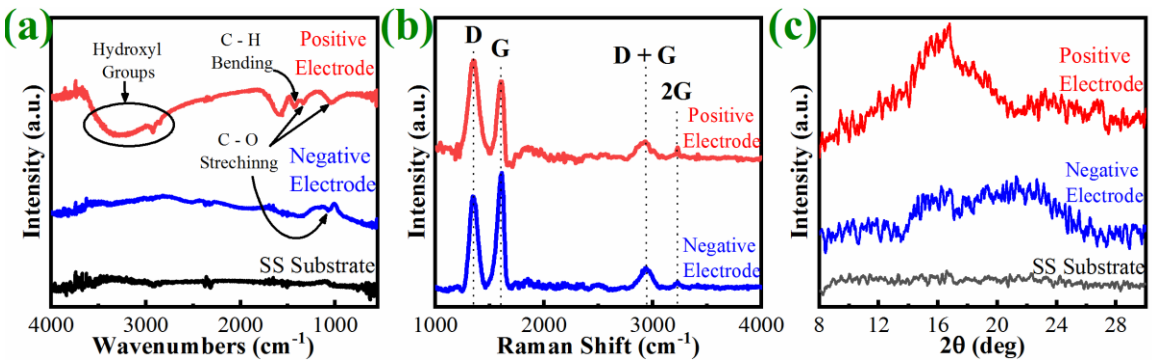

Figure 4-2. (a) FTIR spectra, (b) Raman spectra, and (c) XRD patterns of produced materials deposited on the positive and negative feeding electrodes.

As shown in the X-ray diffraction (XRD) patterns (Figure 4-2 (c)), broad diffraction bands centered around 17° for the positive electrode and around 20° for the negative electrode can be observed. According to Bragg's law of diffraction ($n\lambda=2d\sin\theta$, $n=1$, $\lambda=1.54056$ Å),

the diffraction angle (2θ) of the (002) planes in pure graphite is 26.5° with an interlayer spacing of 3.35 Å[96-98]. A diffraction angle of 11.4° was reported for fully oxidized GO [96]. It indicates the formation of partially reduced GO coating on both negative and positive electrodes. Furthermore, as the broad peak for the negative electrode shifted to higher values, which indicates that a higher level of reduction occurred on the negative electrode. It is worth noting that the reduction process is more favorable on the negative electrode of the cell, therefore, the production of highly reduced graphene oxide is more probable on the negative electrode than on the positive electrode. In addition, the exfoliation of graphene/graphene oxide can happen on both anodic and cathodic sides of the bipolar electrode. The hydrogen and oxygen production will also happen due to water electrolysis, however the amount of generated gases which is proportional to the electric charge should be relatively very small considering the low time-averaged cell current in Figure 4-1 (c).

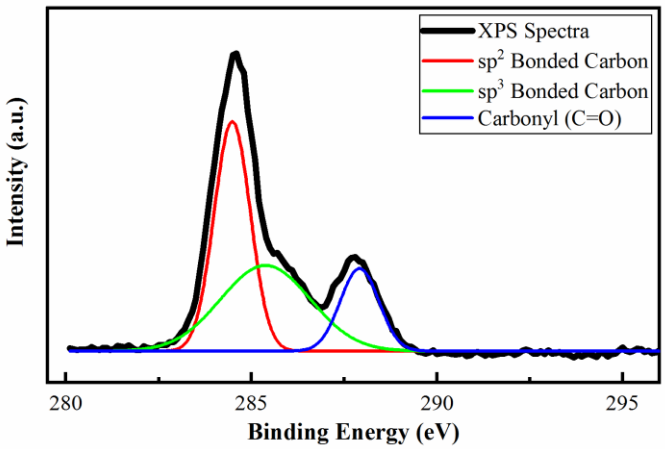

Figure 4-3. XPS (C1s) spectra of deposited material on negative feeding electrode.

Figure 4-4 (a, b, d, and e) shows typical SEM micrographs of the surface of the negative (a and b) and positive (d and e) electrodes after 24 hours of BPE process. It is clear that the

material formed on the negative electrode has a porous vertically aligned structure with pore size of around 100 nm, which could be more favorable for high surface area energy storage applications. The cross-sectional SEM image (Figure 4-5) reveals that the deposition rate on the negative feeding electrode is about 10 nm h^{-1}. In contrast, the graphene on the positive side has a bulky flat structure with deep cracks indicating preferential restacking in the growth stage. The TEM image and SAED patterns of the graphene on the negative electrode are shown in Figure 4-4 (c and f). It can be clearly seen that the thin graphene sheets examined (with some folds or overlaps) of about 400 nm size are formed after 12 hours deposition on the surface of TEM mesh. Single crystalline SAED patterns confirm the formation of low defected graphene sheets. Due to the absence of additional diffraction spots except those for corresponding to the graphite structure, no superlattice-type ordered arrays is observed even with or without any oxygen-containing functional groups present, which proves that the deposited graphene is highly reduced and pure [99, 100]. Furthermore, it has been reported that in the graphene-based materials when the number of stacked layers is more than one layer, the intensity of spots diffracted from $<2\bar{1}10>$ planes will be higher than the ones from $<1\bar{1}00>$ [99, 101]. In the SAED pattern of Figure 4-4 (c), the green marked spots (related to $<2\bar{1}10>$ planes) have a lower intensity than the red marked spots (related to $<1\bar{1}00>$ planes) which indicates that the examined graphene is most likely a single layer graphene. Interplanar spacing (d-spacing) of 0.205 nm can be extracted from the HRTEM image shown in Figure 4-4 (f), which is smaller than the typically reported d-spacing of GO [99].

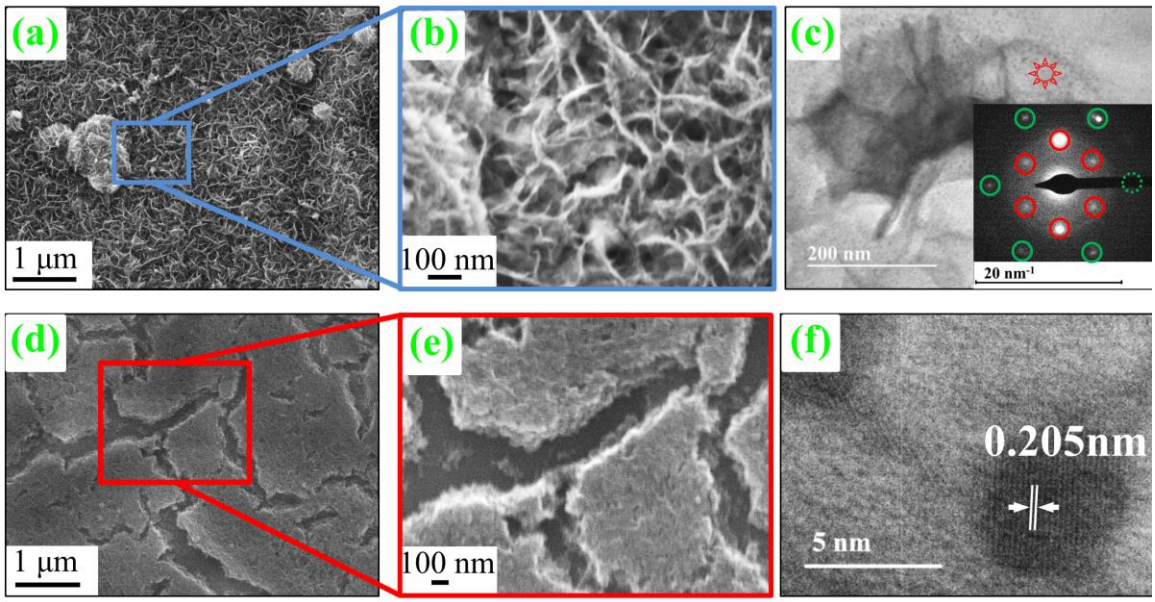

Figure 4-4. (a)-(b) SEM images, (c) TEM image (SAED patterns in inset, green spots are related to $<2\bar{1}10>$ planes and red spots are related to $<1\bar{1}00>$ planes) and (f) HRTEM image of deposited graphene on the negative electrode. (d) and (e) are SEM images of graphene on the positive electrode.

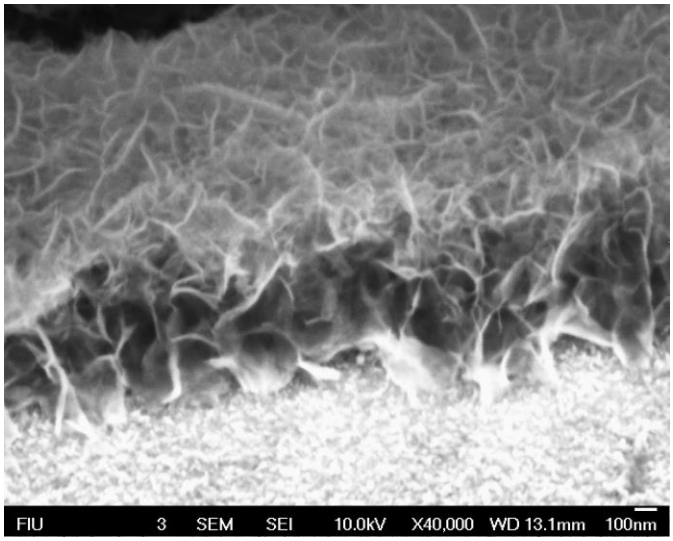

Figure 4-5. Cross-sectional SEM image (tilted by 45°) of the negative feeding electrode after 72 hours of BPE deposition. The thickness of resulted coating is about 700 to 800 nm.

4.3.3 Electrochemical Characterization

Considering the unique surface and structural properties of the binderless graphene-based materials deposited by BPE, their performance for electrical energy storage in supercapacitors was investigated. Figure 4-6 (a) and (b) show the results for the negative and positive electrodes, respectively, wherein the Y-axis the current has been normalized with respect to the scan rate so that it reads directly the areal device capacitance in mF cm^{-2} as a function of voltage. The cyclic voltammetry (CV) curves are almost rectangular in shape at different scan rates which demonstrates an electric double-layer capacitor (EDLC) behavior for both devices. The symmetry of the curves with respect to the zero y-axis shows the excellent reversibility of both devices. The average areal capacitance over the voltage window computed from the CV measurements using:

$$C = \frac{1}{2v\Delta V}\int i(V)dV \qquad (4\text{-}1)$$

is plotted in Figure 4-6 (c) as a function of the voltage scan rate v. In this equation V, i and ΔV are the applied voltage, measured current and voltage window, respectively. Comparing the values in this figure reveals that capacitances decrease with the increase of scan rate for both devices, which is a typical behavior for EDLCs. The capacitance of the negative electrode based device is much higher than the positive electrode based one; at 2 mV s^{-1} the areal capacitance of the negative electrode based device is about 4 times that of the positive electrode based device, and at 10 V s^{-1} it is about 2 times larger.

The performance of these devices was also studied by galvanostatic charge/discharge (GCD) test, as shown in Figure 4-6 (d) and (e). The electrical behavior of the device based on negative electrodes is closer to that of a capacitor since its GCD curves are highly

symmetric and linear with negligible ohmic losses. While the device based on positive electrodes showed more deviation from ideal capacitor given the asymmetry and nonlinearity of the GCD curves and the high ohmic drops. The average areal capacitance of the devices has been calculated for different currents and reported in Table 4-1 using:

$$C = \frac{1}{\Delta V}\int i_{dc}dt \tag{4-2}$$

In this equation, i_{dc} is the discharge current and ΔV is the voltage window of 0.8 V. Rate capability tests were conducted for both devices and the results are presented in Figure 4-6 (f). Both devices show excellent stability up to 30,000 cycles. It can be seen that for the device based on negative electrodes the discharge capacitances are around 0.6 (10000th cycle) and 0.3 (30000th cycle) mF cm^{-2} at 25 and 500 μA $cm^{-2,}$ respectively, while for the device based on positive electrodes the discharge capacitances are around 0.1 mF cm^{-2} (10000th cycle) and 0.04 mF cm^{-2} (30000th cycle) at the same rates. The higher capacitance and good rate capability of the negative electrode based device could be attributed to the unique porous structure with higher surface area and a higher level of reduction of the rGO as demonstrated from SEM/TEM, FTIR, Raman, and XRD results above.

Table 4-1. Discharge capacitances of negative and positive electrode based devices at different current rates.

Discharge Current (μA cm^{-2})	25	50	100	250	500
Negative Electrode Discharge Capacitance (μF cm^{-2})	702.8	599.5	512.6	405.8	323.0
Positive Electrode Discharge Capacitance (μF cm^{-2})	245.5	154.8	64.9	4.5	4.4

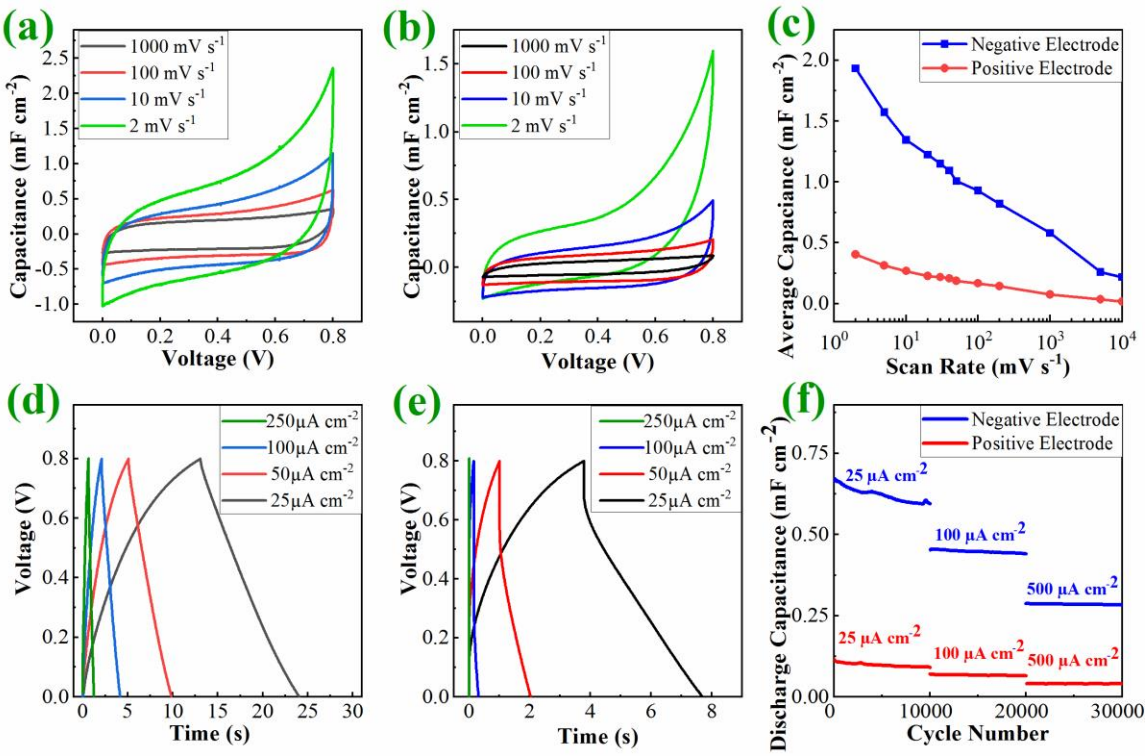

Figure 4-6. Cyclic voltammetry results of (a) negative electrode, and (b) positive electrode based devices at different scan rates. (c) The average areal capacitance of the negative and positive electrodes calculated from the voltammetry measurements at different scan rates. Constant-current charging/discharging results of (d) negative electrode, and (e) positive electrode based devices, (f) capacitances vs. cycle numbers at different charge/discharge currents for both devices.

Finally, the devices were analyzed using electrochemical impedance spectroscopy, and the results are presented in Figure 4-7. From the complex-plane representation of real vs. imaginary of impedance shown in Figure 4-7 (a) and impedance phase angle plot as a function of frequency shown in Figure 4-7 (b), it is clear that the responses of both devices deviate from that of ideal capacitors. An ideal capacitor is expected to show a constant -90° phase angle between the real and imaginary parts of impedance independently of the frequency and voltage. However, the impedance angles of both devices are relatively stable from 10 mHz to 100 Hz, i.e. -60.3° (R^2 = 0.561) and -58.2° (R^2 = 0.862) for the positive

and negative electrode based devices, respectively. Nonetheless, despite the deviation from ideal capacitor behavior, devices with similar responses were shown to be favorable for non-dc applications such as AC line filtering [7, 50, 102, 103] and low-frequency oscillators[104, 105]. Then, as the frequency is increased, the impedance angles tend quickly towards a resistive behavior as shown in Figure 4-7 (b). An angle of -45° at which the magnitude of resistance and reactance are equal is found to be at the frequencies of 1820 Hz and 1157 Hz for the positive and negative electrode based devices, respectively. This extended capacitive behavior can be attributed to the two-dimensional structure of the active electrode materials which facilitate fast charging and discharging of the devices.

To evaluate the performance metrics of the two devices, the impedance data have been modeled using a resistor (R_s) in series with a constant phase element (CPE). The CPE has a fractional-order impedance given by $Z_{CPE}(s) = 1/C_\alpha(j\omega)^\alpha$, where $C\alpha$ (in units of $F\ s^{\alpha-1}$) and α $(0 < \alpha < 1)$ are the CPE parameter and CPE exponent respectively, and $(j\omega)^\alpha = \omega^\alpha[cos(\alpha\pi/2) + j\ sin\ (\alpha\pi/2)]$ [7, 102, 103]. The phase angle of a CPE is constant and is equal to - απ/2 which makes it an intermediary element depicting intermediary behaviors between ideal capacitors and resistors [106, 107], which is the case in this study. The impedance fitting parameters $(R_s; C_\alpha; \alpha)$ for the positive electrode-based device (over the frequency range 48 kHz (intercept with $Im(Z) = 0$) to 10 mHz) and the negative electrode based device (over the frequency range 61 kHz to 10 mHz) were computed using complex nonlinear least-squares minimization and found to be (10.92 Ω, 0.087 mF $s^{\alpha-1}$, 0.683) and (11.28 Ω, 0.138 mF $s^{\alpha-1}$, 0.705), respectively. An effective frequency-dependent capacitance (C_{eff}) in Farads and frequency-dependent resistance (Reff) in Ohms can be computed by writing equation (4-3) which leads to equations (4-4) and (4-5) as follows:

$$Z = R_s + \frac{1}{(j\omega)^{\alpha} C_{\alpha}} = R_{eff} + \frac{1}{j\omega C_{eff}} \quad (4\text{-}3)$$

$$C_{eff} = \frac{\omega^{(\alpha-1)} C_{\alpha}}{sin(\alpha\pi/2)} \quad (4\text{-}4)$$

$$R_{eff} = R_s + \frac{cos(\alpha\pi/2)}{\omega^{\alpha} C_{\alpha}} \quad (5)$$

Instead of representing the real vs. imaginary of impedance as depicted in Figure 4-7 (a), one can represent the performance of the devices using a plot of C_{eff} vs R_{eff} as shown in Figure 4-7 (c). It is clear from this figure that in terms of energy storage in the frequency-domain the negative electrode based device outperforms the positive electrode based one, again attributed to the favorable structure of its electrodes materials for fast and effective electrical charge storage and ionic movement. Furthermore, the existence of a capacitance (even small) at high frequencies with low effective resistance makes both devices suitable for filtering applications. For instance, at 120 Hz, (C_{eff}, R_{eff}) were found to be about (22.2 μF cm^{-2}, 42.6 Ω) and (12.3 μF cm^{-2}, 72.2 Ω) for the negative and positive electrode based device, respectively.

Practical application of the EDLC as AC line filter was studied and compared with a commercial aluminum electrolytic capacitor (AEC). For this purpose, a sinusoidal wave (60Hz, V_{peak}=±1V) was applied to AC filter circuit using a four-Schottky-diodes bridge rectifier and a 39 kΩ resistor as the load. The voltage output without using smoothing EDLC was a pulsing full wave rectified signal (120Hz, V_{peak}=+0.82V), which is shown in Figure 4-7 (d). After the negative electrode based EDLC was connected to the filter circuit, the pulsing signal was flattened to 0.728 V. The same test was also conducted by using a

100 µF AEC; a dc signal of 0.735 V was obtained. These results demonstrated the excellent AC filtering function of our EDLC which is comparable to commercial AEC.

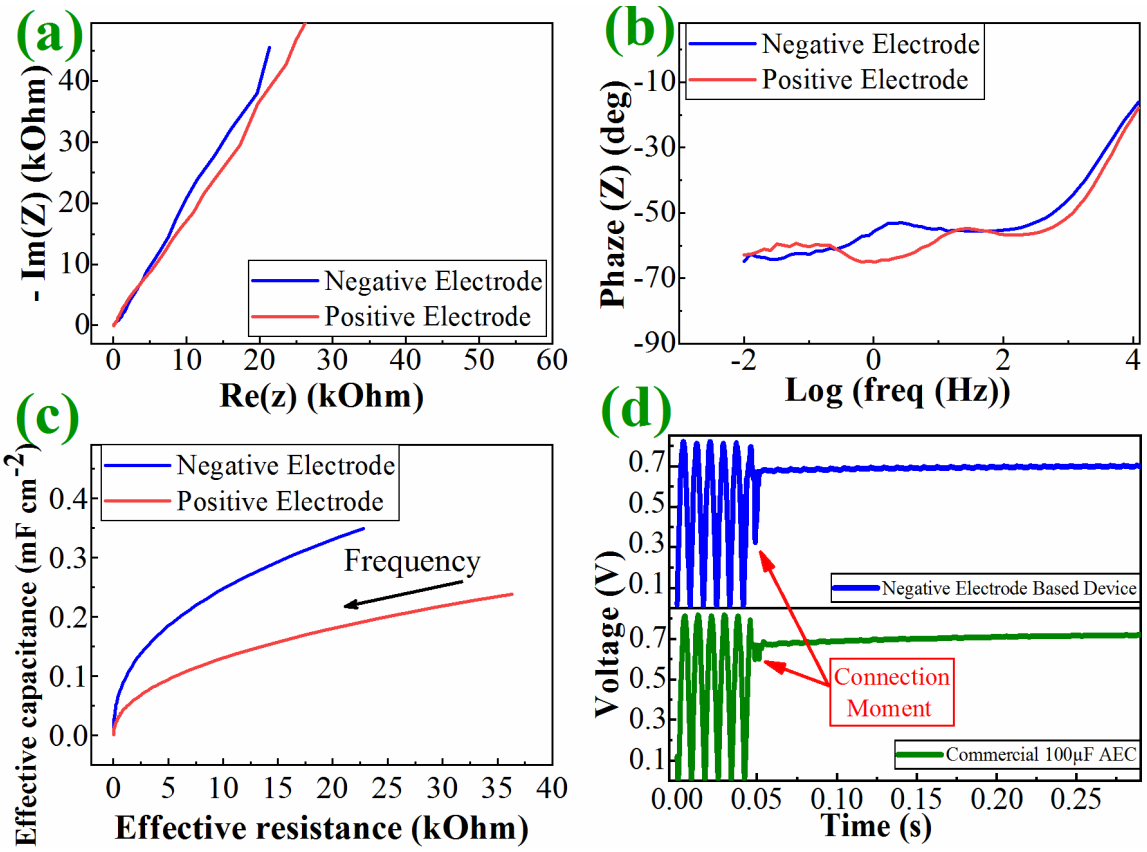

Figure 4-7. (a) Complex-plane representation of real vs. imaginary of impedance, (b) impedance phase angle plot as a function of frequency, and (c) effective capacitance vs effective resistance of the negative electrode and positive electrode based EDLCs. (d) Smoothing capability of the negative electrode based EDLC device in a full wave rectifier circuit compared to a commercial 100µF aluminum electrolytic capacitor.

According to the electrochemical results, the specific capacitance of EDLC fabricated by BPE at negative feeding electrode was ~2 mF cm^{-2} at the scan rate of 2 mV s^{-1} and ~ 0.7 mF cm^{-2} at a discharge current of 25 µA cm^{-2}, which is comparable with the previous studies. It has been reported that the areal capacitance is in the range of 0.021 to 2 mF cm^{-2} for few layer graphene based materials at the same or even lower scan rates or discharge

currents [7, 108-112]. Considering the capability of three-in-one exfoliation, deposition, and reduction process, high performance and high stability of the assembled devices, BPE is demonstrated as a promising technique for production of graphene-based EDLCs. BPE was shown to be environmentally-friendly and simple to operate, since it takes place at room temperature using deionized water without any additives and any other chemicals. Furthermore, compared to other materials synthesis methods using three-electrode systems or high-temperature/high-pressure reactors, BPE uses simple instrumentation (i.e., a single dc power supply). In principle different types and number of conductive materials can be coated simultaneously in one cell, which makes the BPE technique ideal for scale-up manufacturing of graphene based devices.

4.4 **Conclusion**

In this study, a three-in-one exfoliation, reduction, and deposition of graphene-based materials were conducted via BPE process. By evaluating the total and bipolar current in the fabrication process, it is clear that the exfoliation of graphite is promoted with time. Highly reduced graphene layers with porous structure were formed on the negative electrode. The electrochemical characterization revealed that the electrode has a high areal capacitance (~2 mF cm^{-2} at the scan rate of 2 mV s^{-1} and ~0.7 mF cm^{-2} at a discharge current of 25 µA cm^{-2}) with long-term cyclability which is important for supercapacitor applications. The device performance at high frequencies showed promising results for AC filtering of leftover ripples. In principle, different types and number of conductive substrate materials can be coated at once, which makes this technique ideal for scaling up purposes.

5. On the Mechanistic Pathways of Exfoliation-and-Deposition of Graphene by Bipolar Electrochemistry

5.1 Introduction

Bipolar electrochemistry (BPE) refers to an electrochemical phenomenon that wirelessly induces an asymmetric polarization and redox reactions on a conductive or semiconductive object, i.e. bipolar electrode (BE), in the existence of a sufficient electric field between two conductive feeding electrodes. In the case of using BE with much higher conductivity compared to that of the electrolyte, BE remains almost isopotential, and the electric field produces interfacial potential differences (δ^+, δ^-) between the BE and the electrolyte leading to the polarization of the BE edges. As a result of the spatial variation of the BE/solution potential, coupled reduction and oxidation reactions occur simultaneously on the two extremities of the BE. Specifically, the anodic process takes place at one extremity of the BE close to the negative feeding electrode, while the cathodic reduction takes place at the other extremity, i.e., close to the positive feeding electrode [6, 25, 26].

BPE has found many interesting applications in different fields of science and engineering, such as micro and nanofabrication [113, 114], propulsion of small objects in solution [115], and electroanalytical and sensing devices [116, 117]. Furthermore, by making use of both the spatial distribution of current and voltage across the BPE cell (Figure 5-8) and the possibility of electro-inducing displacements of charged particles, a new application for BPE was recently demonstrated, that is the two-in-one exfoliation-and-deposition of 2D Van der Waals materials, such as graphene and phosphorene [5-8, 28, 118]. Allagui et al.

were first to report the successful exfoliation of graphite into partially reduced graphene oxide (rGO) deposited on the positive feeding electrode in deionized (DI) water [6]. In a follow-up study [5], a modified BPE process was used for the fabrication of both vertically-aligned, high-quality rGO on the negative feeding electrode, and stacked layers of GO on the positive feeding electrode. Electrochemical properties and stability of deposited graphene after the electrochemical cycling test was studied in addition to detailed materials charactrization by XPS, XRD, and Raman spectroscopy. The results showed modified BPE method can deliver simultaneous exfoliation, reduction, and deposition of graphene-based materials in a simple, cost-efficient, and environmentally friendly technique[5].

The vertical arrangement of the deposited rGO nanosheets on the negative feeding electrode resulted in a high surface area morphology which is suitable for many electrochemical devices. As an example, an electrochemical double-layer capacitor (EDLC) using such structured electrodes was fabricated and demonstrated to hold charge with a high specific areal capacitance of 1.9 mF/cm^2 at 2 mV/s and a wide frequency response from dc to tens of Hz, which is useful for both dc energy storage and ac line filtering applications [5]. The BPE method was also used to develop a two-in-one process to exfoliate and deposit phosphorene nanosheets on conducting substrates using black phosphorous as the BE and DI water as the electrolyte. Likewise, the phosphorene electrode showed a high discharge energy of 22.8 nWh/cm^2 and high coulombic efficiency [118].

Although BPE was demonstrated to be a promising and environmentally-friendly method for exfoliation and deposition of 2D materials, there are still several open questions

regarding its mechanism and performance. The aim of this study, which is focused on the behavior of carbon graphite BE in BPE cell, is to provide some answers to the following questions: (i) What are the exfoliation mechanisms that take place during the BPE of graphite? (ii) Why are the reduction states of the deposited carbon films dissimilar at the two positive and negative feeding electrodes? and (iii) How the exfoliation mechanism can affect the morphology of deposited films. To do so, we designed a novel set of experimental configurations to overcome the limitations of conventional BPE setup, which allowed us to decouple the anodic and cathodic reactions and study the rule of each one on the properties of fabricated graphene by BPE.

5.2 Materials and Methods

5.2.1 Modified bipolar electrochemistry setup

Figure 5-1 (a, b) show the schematics of the modified BPE cells designed to evaluate the bipolar exfoliation mechanism. The negative and positive feeding electrodes were 2×1 cm^2 316 stainless steel sheets (from Maudlin & Son Mfg.Co) placed 9 cm apart in DI water (Resistivity of 18 MΩ.cm and pH of 6.3), and the applied voltage was set to 45 Vdc (by means of an N6705A DC Power Analyzer). As explained in [5], the increase in the electrolyte conductivity will decrease the ratio of bipolar current to the total cell current, which is detrimental in the BPE process for exfoliation of 2D materials. Therefore, DI water which has relatively high resistivity is used to maximize the ratio of bipolar current to the total cell current to ensure successful exfoliation of graphene.

In addition, a platinum (Pt) coil was used either as the cathodic (Figure 5-1 (a)) or anodic (Figure 5-1 (b)) pole of the BE system, whereas at the oppostite pole we used a graphite rod of 4 cm in length and 6.15 mm in diameter (Ultra "F" Purity 99.9995%, from Alfa Aesar). The two parts of the BE were electrically connected by a wire as shown in Figure 5-1 (a, b). The extremities of these poles across the electric field experience the bipolar effect, which gives an apparent potential difference of nearly 35 V due to the 5 Vcm^{-1} electric field and the 7 cm distance between the farthest point of the poles. The actual voltage measurement between the Pt and the graphite was in the range of 33 - 34 V. It should be noted that this apparent voltage is high enough to enable the electrochemical exfoliation of graphite and water electrolysis, resulting in the reduction of ions and oxidation of ions at the cathodic and anodic poles of the BE, respectively [5, 6, 53]. These two asymmetric configurations are designed to make the anodic and cathodic reactions more trackable, compared to the conventional BPE setup (Figure 5-8) in which the same material is used for both anodic and cathodic poles of the BE. Specifically, they give the opportunity to deactivate either the anodic or cathodic exfoliation of graphite and prevent any undesired side reactions to take place during the BPE process (Pt is known as one of the most inert conductive materials in DI water [119-121]). We denote by "G+ configuration" the setup in which the graphite is positively polarized, and the Pt is negatively polarized (Figure 5-1 (a)). With this configuration, only the anodic exfoliation is supposed to be taken place on the graphite. Similarly, we denote by "G– configuration" the setup in which the graphite is negatively polarized, and the Pt is positively polarized (Figure 5-1 (b)) where only the cathodic exfoliation is supposed to be taken place on the graphite.

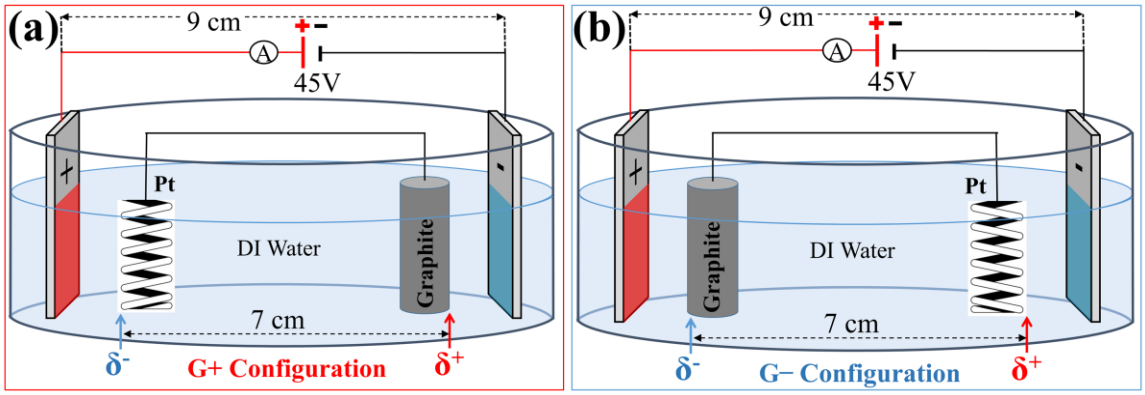

Figure 5-1: Schematic representations of the two bipolar electrochemical cells using coupled bipolar electrodes (graphite and Pt): (a) G+ configuration and (b) G– configuration.

The BPE experiments were conducted for different time durations (from 12 up to 72 hours), with and without magnetic stirring (magnet of about 1 cm in length and stirring speed of about 150 rpm) to better understand the BPE at transient and steady-state regimes. The cell current was measured via the potential drop across a precision resistor inserted in the electrochemical circuit. The cell temperature was constant at 24˚C for all experiments.

5.2.2 Materials characterization

Scanning electron microscopy (SEM) images of the feeding electrodes were obtained using a JEOL SEM 7000. The study of surface functional groups of deposited materials on the feeding electrodes and colloidal suspensions (collected by vacuum filtration of electrolytes using Ahlstrom filter paper grade 601) was carried out by Fourier transform infrared spectrometry (FTIR) on a JASCO FT/IR 4100.

5.3 **Results**

The G+ and G– configurations have been developed to decuple the anodic and cathodic exfoliation of graphite in the BPE process. In order to understand how graphite polarization and process time contribute to the morphological properties of the fabricated graphene, microstructural studies have been conducted at different time intervals for both configurations.

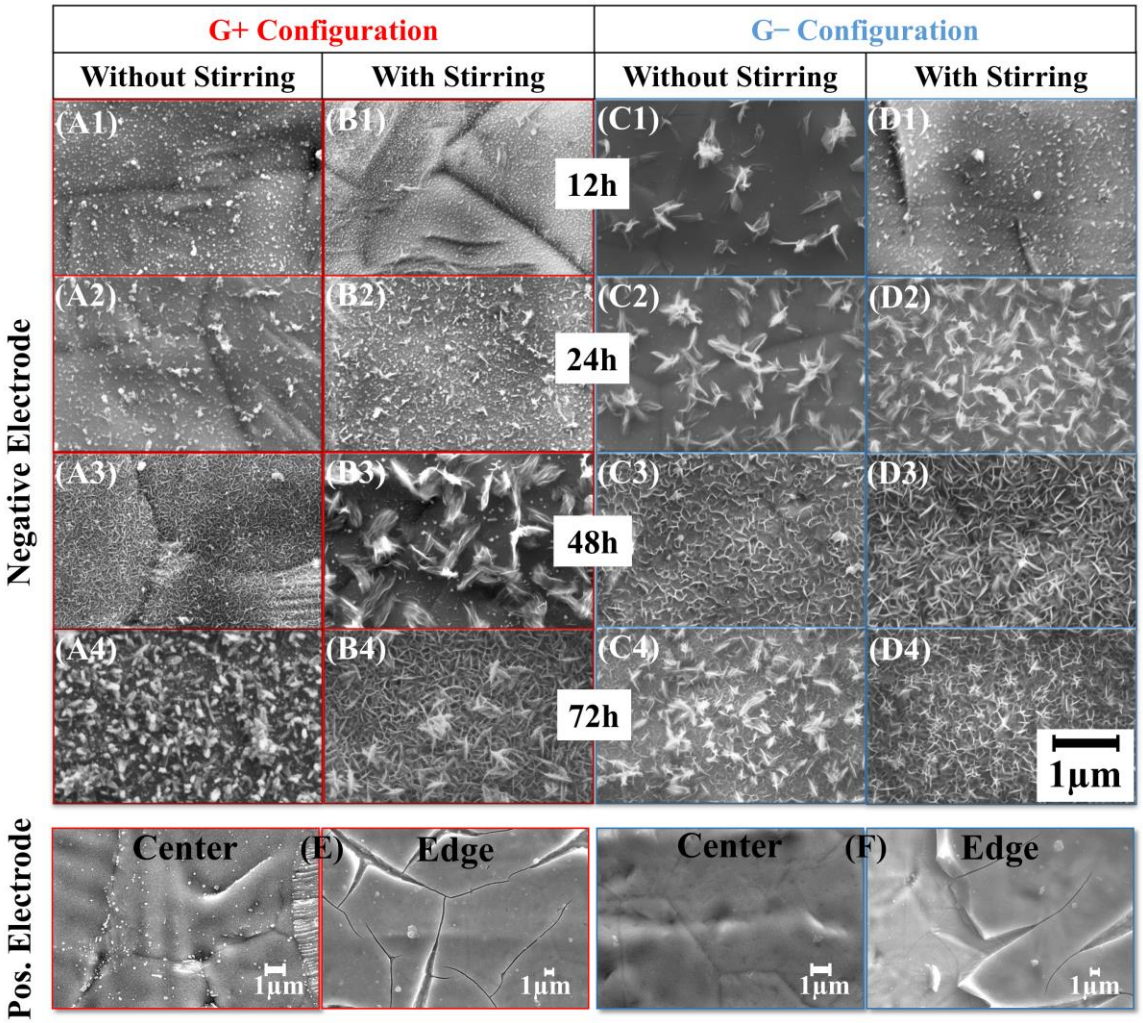

Figure 5-2: SEM micrographs of the negative feeding electrode taken chronologically from 12 to 72 hours of BPE operation for both G+ (circled in red frame) and G– (circled in blue frame)

configurations, without and with stirring (A1-D4 as indicated). E and F are typical SEM images of the positive feeding electrodes of both G+ and G– configurations, respectively.

For the case of G+ configuration, SEM micrographs of the negative feeding electrode without stirring for different durations of the BPE experiment, i.e., 12, 24, 48, and 72 hours, are shown in Figure 5-2 (A1-A4), respectively. The same are shown in Figure 5-2 (B1-B4) respectively for the situation when stirring is applied. As it can be seen, the deposition of graphene-based materials on the negative electrode took place in both arrangements with and without stirring. It is also evident that the amount of deposited material increases with time; however, the deposition rates vary with or without stirring. At the beginning of the process for G+ configuration (with and without stirring), only a small amount of material can be visualized from the SEM micrographs. It seems that seeding and nucleation of clusters , are what is mostly occurring within the first several hours of the process. The deposited material consists of uniformly dispersed small particles in the order of 50 nanometers in size. This can somehow be mapped with the overall cell current (Figure 5-3 (a)), which was found to be relatively flat and stable at around 0.2 mA for the first 9 hours of the experiment when the solution was undisturbed (no stirring). Similarly, when the solution was continuously stirred, the cell current remained almost stable around 0.15 mA, for the first 20 hours of the process. Furthermore, it can be seen that with time, the morphology, uniformity, and density of deposited material evolve very differently from the samples fabricated with and without stirring. The SEM of the deposited layer without stirring at t = 72 hours (Figure 5-2 (A4)) shows aggregated graphene sheets and dispersed particles with relatively higher thickness, whereas the deposited material when stirring is applied after the same duration (Figure 5-2 (B4)) led to the formation of a network-like

structure of thin graphene sheets with relatively large lateral size. As for the positive feeding electrode of the cell, typical SEM images are shown in Figure 5-2 (E) for 72 hours of operation time (taken from the center and lateral edge of the electrode), which reveal a uniform stacking and much denser layers of graphene materials compared to the negative feeding electrodes. The cell current for these two situations are shown in Figure 5-3 (a). The current of the setup without stirring shows some low-frequency fluctuations, whereas a quasi-smooth, lower-rate increase of the current is observed for the case when the solution was continuously stirred. These fluctuations are mainly attributed to the dynamics of bubble formation and bubble release on the surface of electrodes. When the bubble size reaches a critical value to overcome surface tension and other resistive forces, they can be detached from the electrodes and released from the solution by buoyancy. As a result, the effective surface of electrodes in direct contact with the electrolyte was continuously changing, resulting in the cell current fluctuation. It should also be mentioned that the cell current in this experiment was in the order of several microamperes to few milliamperes, which implies the stirring effect from bubble generation and evolution is negligible.

In contrast, the deposited materials were quite different for the case of the G– configuration. SEM images for the negative feeding electrode in the G– configuration, which were also taken chronologically from 12 to 72 hours without and with stirring, are depicted in Figure 5-2 (C1-C4) and 5-2 (D1-D4), respectively. When no stirring was used, the deposition of large graphene flakes in the form of either single or aggregated multiple sheets can be observed, even at the early stages of the process (see for instance, Figure 5-2 (C1) for SEM micrograph taken after 12 hours of deposition). For $t > 12$ hours, the deposition rate is also

increased when stirring was added to the G– configuration, which is evident by comparing Figure 5-2 (C2) and 5-2 (D2), as well as Figure 5-2 (C3) and 5-2 (D3).

The SEM images of the positive feeding electrode at t = 72 hours are shown in Figure 5-2 (F), depicting relatively the same uniform deposit as observed for the reverse configuration. The cell current (Figure 5-3 (b)) for the case when the solution was not stirred, shows an increase from 0.10 to 0.28 mA within the first two hours, and then an asymptotic stabilization of the current down to 0.20 mA for the remaining time. For the setup with stirring, the current increased very slowly from 0.05 mA to reach barely 0.27 mA after 72 hours of operation (Figure 5-3 (b)), which is about six times lower than the value of 1.6 mA for G+ configuration. The color of the electrolyte was more yellowish for the G+ configuration without stirring, which can be considered as a sign of a higher amount of exfoliated graphene in the solution due to higher total cell current.

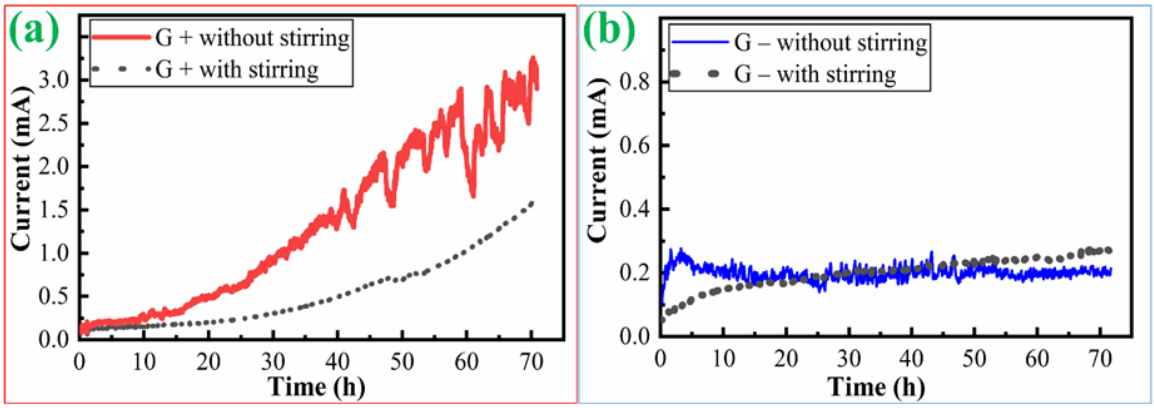

Figure 5-3: Cell current vs. time profiles for the two configurations G+ (a) and G- (b) with and without stirring of the solution. At t=60 h more DI water was added to the cell of G+ without stirring to compensate the electrolyte evaporation.

Figure 5-4 shows typical results of FTIR analysis of the deposited materials on the positive and negative feeding electrodes after 72 hours of BPE, in comparison with the spectral

response of the collected materials from the electrolyte for both the G+ and G– configurations. In general, the broad peak around 3000 to 3600 cm^{-1} indicates the presence of hydroxyl groups [91, 92, 122]. The peaks centered at wavenumbers of 2900 cm^{-1}, 1723 cm^{-1}, 1600 cm^{-1}, and 1430 cm^{-1} are attributed to the C-H bond stretching, C=O bond stretching, aromatic C=C bond stretching, and C-H bond bending, respectively [91, 92]. The peak at around 1330 cm^{-1} is ascribed to C-O bond stretching, and the one at 1055 cm^{-1} is attributed to the C-OH stretching [93]. The peaks at around 2300 cm^{-1} may originate from an interaction with the instrument and/or substrate since they were also detected from the bare stainless steel substrate.

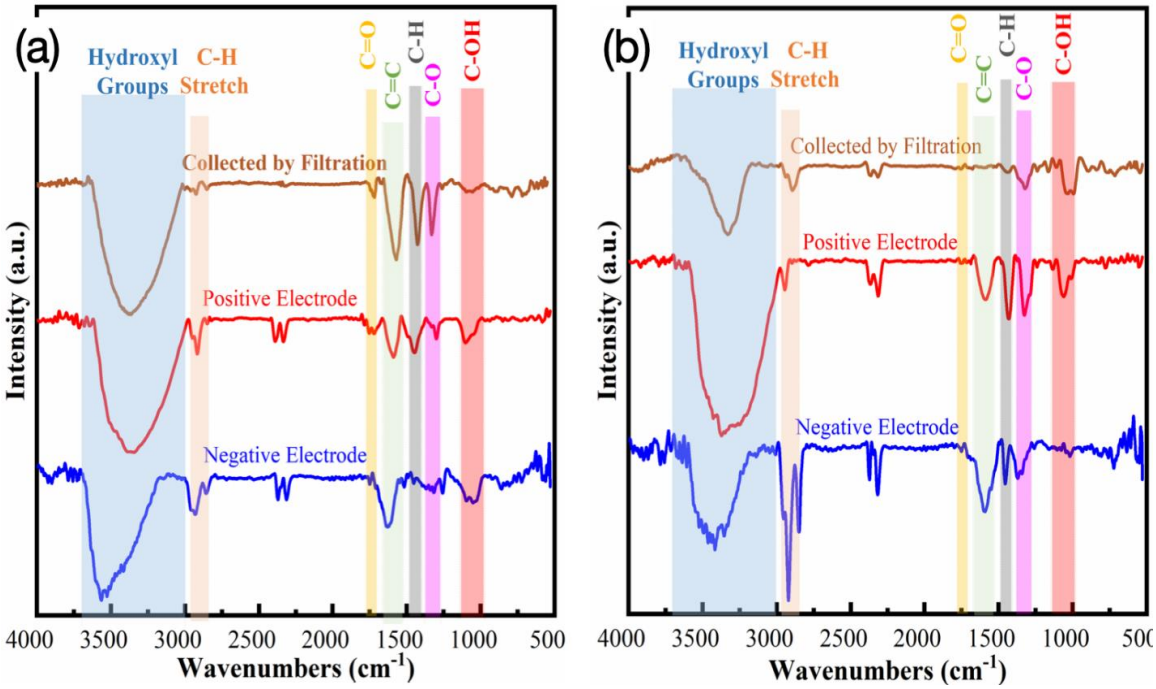

Figure 5-4: FTIR spectra of deposited materials on the negative and positive feeding electrodes, and of collected materials from the electrolyte when operating under the G+ (a) and G– (b) configurations after 72 hours of BPE

In the case of G+ configuration (Figure 5-4 (a)), it is clear that the most prominent peak is corresponding to hydroxyl group in addition to noticeable contributions from the C=C, C-H, and C-O bonds for the negative feeding electrode. For the positive feeding electrode, the hydroxyl group peak has the highest intensity, and weaker peaks related to C=C, C-H, C-O, and C=O functional groups. The FTIR results of collected materials from the electrolyte show all characteristic peaks of the C-OH, C=C, C-H, C-O, and C=O functional groups (listed in the order from high to low intensity). In the case of G– configuration (Figure 5-4 (b)), it is clear that the negative feeding electrode show an intense C-H stretching response and relatively strong peaks related to C-OH and C=C bond stretching and weaker C-O response. For the positive feeding electrode, high-intensity hydroxyl group peak and other characteristic peaks of C-H, C-O, C=C, and C-OH can be observed. For the collected free-standing materials from the electrolyte, C-OH, C-H, and C-O groups, in addition to the hydroxyl group, can be observed.

It should be noted that the deposition rate and the morphology of deposited material could be varied by changing the electric field (either by changing the distance or the applied voltage between the feeding electrodes), shape and size of of feeding electrodes and the bipolar electrode. Further studies on the effect of such variables on the deposition can be the subject of our future study.

5.4 FEM Model and Results

A FEM model has been developed to study the ion motion and electrochemical reactions that occurred in the BPE. The studied geometry is a simplification of the transverse plane

of the setup. A 2D model is adopted to simulate the aqueous electrolyte, including the feeding electrodes, anodic and cathodic poles of the BPE cell as described in section 2-1. The Nernst-Planck equations for all the ions and Poisson equation for the potential were coupled and solved using the COMSOL program in a finite element-based solution. Electric currents and transport of diluted species packages of COMSOL program were coupled together through the potential of the electrolyte solution. The basic conservation equation for the transport of diluted species "i" supports ionic species transport is described by the Nernst-Planck equation:

$$\frac{\partial C_i}{\partial t} + \nabla \cdot (-D_i \nabla C_i - z_i u_{m,i} F C_i \nabla V) = 0 \quad (5\text{-}1)$$

This equation combines the mass conservation with the ion flux due to diffusion and migration in an electric field. The diffuse flux vector can be expressed for such a situation as:

$$J_i = -D_i \nabla C_i - z_i u_{m,i} F C_i \nabla V \quad (5\text{-}2)$$

As for the electric potential, Poisson's equation considering the ion concentration can be written as:

$$\nabla \cdot (-\varepsilon \nabla \phi) = (C_+ - C_-)F \quad (5\text{-}3)$$

The main boundary conditions for this problem are the BPE cell potentials and the electrode reactions. The reaction rate density at the electrode-electrolyte interface was calculated based on the Butler–Volmer equation:

$$r = K_a c_M \, exp\left(\frac{\alpha_a F \phi_\Delta}{RT}\right) - K_c c_+ \, exp\left(\frac{-\alpha_c F \phi_\Delta}{RT}\right) \quad (5\text{-}4)$$

where K_a and K_c are the anodic and cathodic constants and α_a and α_c are the anodic and cathodic transfer coefficients. ϕ_Δ is the difference between the metal voltage and the reaction plane, i.e.:

$$\phi_\Delta = \phi_M - \phi \tag{5-5}$$

Numerical simulations were carried using COMSOL 5.4 using a free tetrahedral dominant mesh. At the interface between the electrolyte and electrodes/anodic and cathodic poles, a boundary layer mesh (prism mesh) is maintained to accurately solve the ion fluxes at the interfaces, as shown in Figure 5-5.

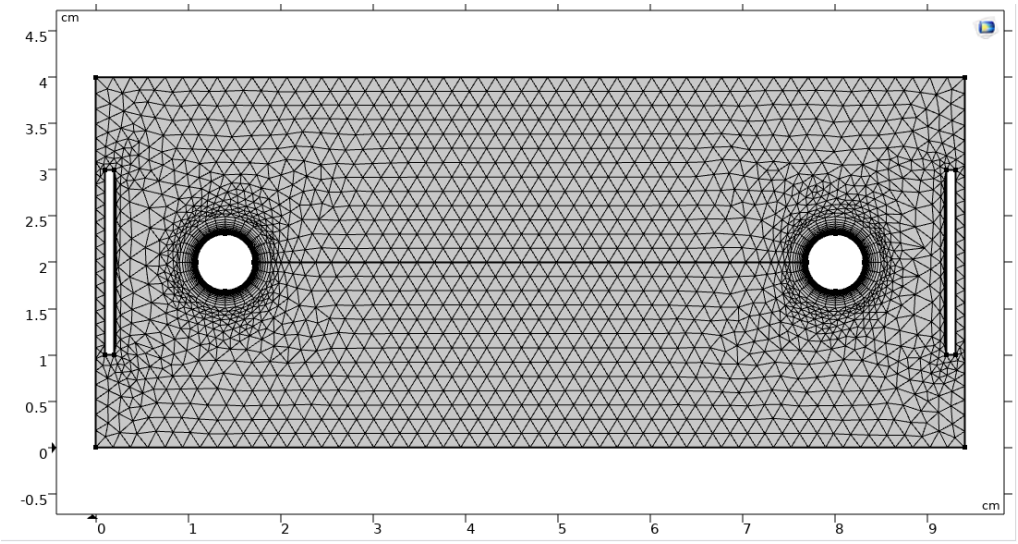

Figure 5-5: Computational domain and adopted mesh in the 2D FEM model

Steady-state computations were carried out to simulate the PNP equations with the BPE cell in a similar fashion to [123]. Figure 5-6 depicts the dimensionless concentration of both ions H^+ , and OH^- as well as the dimensionless voltage along the centerline of the BPE cell.

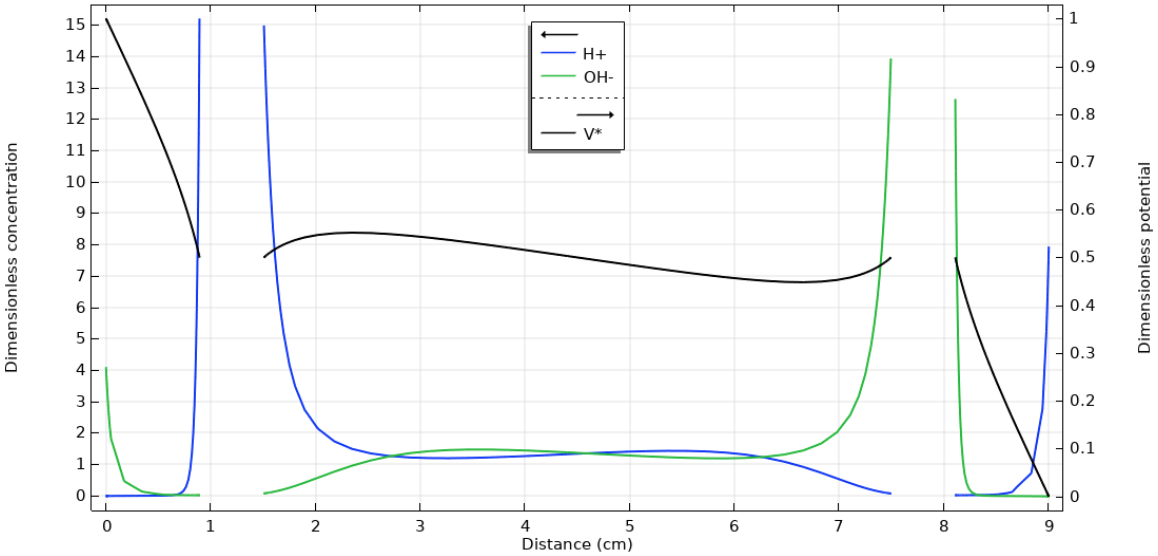

Figure 5-6: Dimensionless ion concentrations and potential profile along the centerline of the BPE cell.

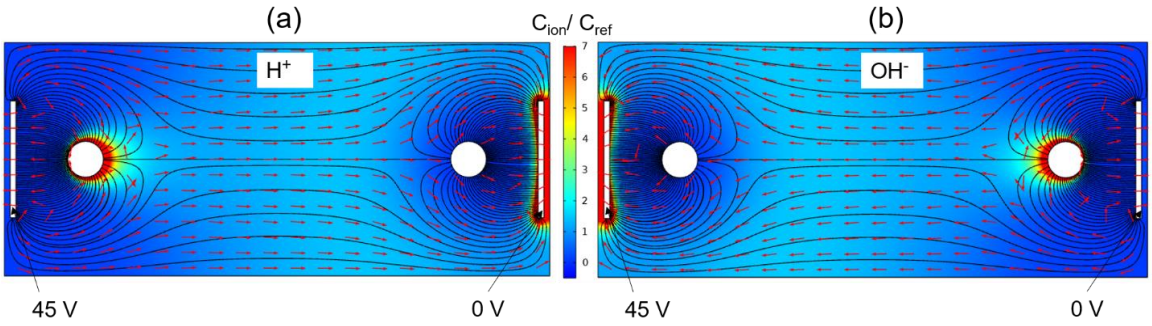

Figure 5-7: 2D representation of the ion concentration (color), flux (arrows), and electric field (lines) for a) H^+ , and b) OH^-.

5.5 **Discussion**

First, we recall that when considering a single bipolar planar substrate with dimensions of $L_0 \times l$ L$_0$ × lon which two different redox reactions can take place, i.e., $R_a \rightarrow Ox_a + n_a e^-$ and $Ox_c + n_c e^- \rightarrow R_c$, it can be shown from the treatment of Duval et al. [124] that the total

anodic current (I_a) and cathodic current (I_c) at the BE/electrolyte interfaces as a function of the background electric field E_b are given respectively by the Butler-Volmer equations. The usual notations are used for anodic and cathodic reactions' exchange current densities (j_a^0 and j_c^0), transfer coefficients (α_a and α_c), number of electrons transferred per molecule (n_a and n_c), and electrochemical standard potentials (E_a^0 and E_a^0). The variable E_m defines a mixed potential adopted by the BE in the absence of any external field and thus for an overall zero current (i.e., at x_0 which defines the border between the anodic and cathodic reactions on the BE, Figure 5-8). The thermal voltage is given by V_{th} = RT/F, where R is the ideal gas constant, T is the temperature, and F is Faraday's constant. Conceptually, the voltage and faradic current distribution profiles (anodic and cathodic) along the cell's centerline can be depicted as shown in Figure 5-8. The lateral variation of the BE/electrolyte potential provokes the coupled redox reactions, which can be controlled by the externally-applied voltage and the lateral size of the BE.

$$I_a = \frac{j_a^0 l V_{th}}{n_a(1-\alpha_a)E_b} \times \exp\left[n_a(1-\alpha_a)(E_m - E_a^0)/V_{th}\right] \times \left\{\exp\left[n_a(1-\alpha_a)E_b(L_0 - x_0)/V_{th}\right] - 1\right\} \quad (5\text{-}6)$$

$$I_c = \frac{j_c^0 l V_{th}}{n_c \alpha_a E_b} \times \exp\left[-n_c\alpha_c(E_m - E_c^0)/V_{th}\right] \times \left\{1 - \exp\left[n_c\alpha_c E_b x_0 / V_{th}\right]\right\} \quad (5\text{-}7)$$

The figure was drawn based on equations (5-6) and (5-7). The figure confirmed the bipolar current in the middle of the bipolar electrode is negligible compared to the current values on the edges of the bipolar electrode which indicates the effectiveness of using modified bipolar system for exfoliation of graphite

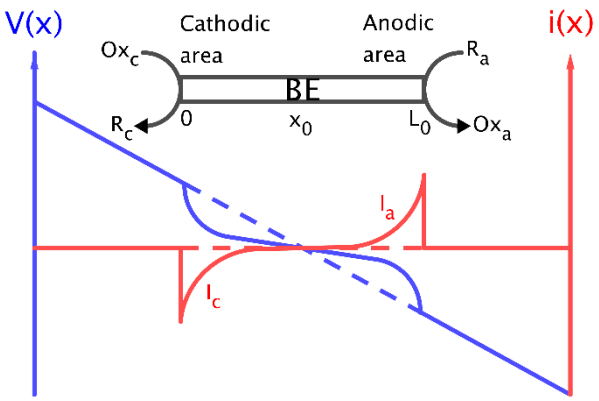

Figure 5-8: A schematic of conventional BPE setup showing the total anodic and cathodic currents at the BE/electrolyte interfaces and the voltage gradient in the BPE cell. The dashed blue line shows the voltage gradient without placing the BE in the cell.

In addition to these faradic processes, if the products of the redox reactions are charged particles, a coupled electro-induced flow of these particles may occur. This flow originates from the interaction of the applied electric field with the electric double layer located at the surface of the charged species, producing an effective slip velocity (u) [125, 126]. Once steady, the velocity of one dimensional and fully developed flow is given by the Helmholtz-Smoluchowski formula [125]:

$$u = -\frac{\varepsilon_0 \varepsilon_r \zeta}{\mu} E_l \qquad (5\text{-}3)$$

where ζ is the local zeta potential, i.e., the potential of the surface minus the potential just outside the double layer and E_l $\mathrm{E_l}$ is the local electric field. ε_0, ε_r and μ the permittivity of free space, relative permittivity, and the dynamic viscosity of the fluid, respectively. Both ζ and E_l $\mathrm{E_l}$ are affected by the rates of the bipolar reactions, and typical flow speed of the order of 100 μms^{-1} (1 mm min^{-1}) could be produced by a field of 100 V cm^{-1} [125]. In this study, the exfoliation and deposition of graphene materials on the feeding electrodes are the results of coexistent phenomena of generation of faradaic currents at the

BE/solution interface and electro-induced fluxes by the electric field driving force. The finite element method (FEM) analysis and results obtained from the solution of the (i) Poisson-Nernst-Planck equations and (ii) the Butler–Volmer equation, coupled with (iii) the diffusion and migration in an electric field for the H^+ H^+ and OH^- OH^- ionic movements (see Figure 5-6 and Figure 5-7) illustrate such coupled dynamics that can be used here to understand (at least phenomenologically) the exfoliation-and-deposition mechanisms during the BPE process.

As indicated by the SEM results (Figure 5-2), both anodic and cathodic exfoliation mechanisms can participate in the BPE process. Depending on the net charge accumulated on the exfoliated graphene-based materials (originating from both anodic and cathodic exfoliation), the suspensions are likely to be dragged and electro-deposited on both negative and positive feeding electrodes. From the analysis of (i) the SEM images of the negative feeding electrode reported in our previous study (24 hours of deposition) [5] where graphite was used in both anodic and cathodic poles of the BE as a coupled BPE process, and (ii) the SEM images of the negative feeding electrodes of both G+ and G– configurations (also for t = 24 hours) in this study (Figure 5-2 (A2) and 5-2 (C2)), it can be deduced that both of the setups of this study have relatively lower deposition rate. Therefore, both anodic and cathodic exfoliations of graphite were contributing to the coupled BPE process.

The mechanism of anodic/cathodic electrochemical exfoliation of graphene in the presence of different ions and intercalating agents is well-documented [71, 127, 128]. Let us first discuss the anodic exfoliation that is schematically illustrated in Figure 5-9 (a). In a typical anodic exfoliation of graphite, the anions from the electrolyte are absorbed by the graphite

anode and gradually intercalate into the graphene sheets [72]. In this study, the only present anion in the electrolyte was OH^- generated as the result of water decomposition. When the high-enough apparent positive potential is applied onto the graphite (on the anodic pole of BE (δ+)), absorption and oxidation of OH^- OH^- ($4OH^- \rightarrow 2H_2O + O_2 + 4e^-$) take place. The intercalation of OH^- OH^- ions in between the graphite sheets leads to the weakening of the Van der Waals bonds holding them together, which results in the degradation and exfoliation of graphite into graphene nanosheets (Figure 5-9 (a)). Furthermore, OH^- OH^- ions are known to be strong nucleophile species that can attack the sp^2 C=C bonds at grain boundaries and other crystallographic defects, and hence forming hydroxylic functional groups according to the reaction [72, 129, 130]:

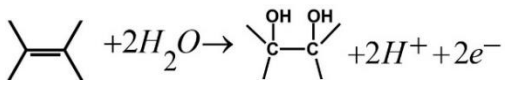

$+2H_2O \rightarrow$ $+2H^+ + 2e^-$ (a)

This is also confirmed by FTIR analysis of Figure 5-4 (a). The hydroxylic functional group causes an increase in the distance between adjacent sheets and, as such, volume expansion of the graphite's structure, which further helps the intercalation and exfoliation process [72, 129, 131]. In addition, the formation and bursting of oxygen gas (from $4OH^- \rightarrow 2H_2O + O_{2(g)} + 4e^-$) in the form of micro/nano bubbles in the vicinity of defects, and even between the sheets, can also help graphite exfoliation [129]. It is observed from the results of Figure 5-4 that the carbonyl functional groups were only detected on the positive feeding electrode and the free-standing sample collected from the solution, but not on the negative feeding electrode. The absence of carbonyl functional group on the

negative feeding electrode also indicates that the partial reduction occurred on the negative feeding electrode.

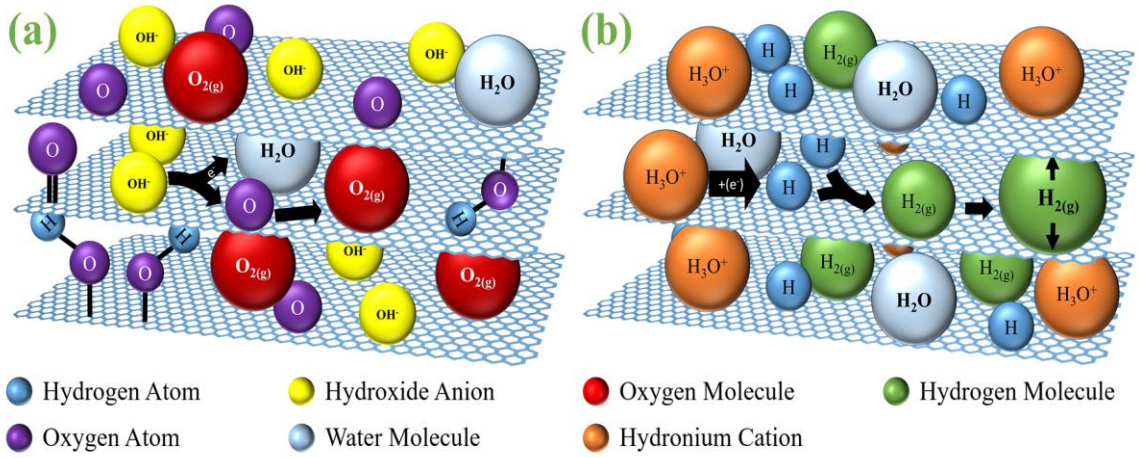

Figure 5-9: Schematic overview of the phenomena which cause the exfoliation of graphite at (a) anodic and (b) cathodic sites.

The proposed cathodic exfoliation mechanism is schematically shown in Figure 5-9 (b). In a typical cathodic exfoliation, cations from the electrolyte are absorbed by the graphite cathode and intercalate into the graphene sheets. In this study, the negative potential of the BE cathodic pole leads to the absorption of H^+ H^+ produced as the result of water decomposition, inserted into the graphite electrode sheets, and then contribute to the widening of adjacent sheets [132]. Moreover, the reduction of H^+ H^+ ions forms nascent hydrogen atoms through the hydrogen reduction ($2H^+ + 2e^- \rightarrow 2\dot{H}$) The hydronium cations or generated hydrogen atoms ($r = 0.12nm$ which is smaller than the interlayer distance of graphite sheets (0.334 nm)) may also intercalate into the graphite sheets. These intercalated species evolve to form larger hydrogen molecules and even gaseous nanobubbles (Figure 5-9 (b)). Similar to the anodic configuration, the development of the

bubbles and their eventual collapsing and bursting are expected to participate into the exfoliation.

During this process, the H^+ ions are consumed by the hydrogen evolution reaction ($2H^+ + 2e^- \rightarrow H_2$), and as a consequence, the localized pH is increased. As demonstrated in the SEM analysis, the deposition of thin and large graphene sheets on the negative feeding electrode started in the early stages of BPE process, which continuously assemble into thin nanosheets 3D graphene structures. This is in good agreement with previous studies that claimed that the cathodic exfoliation process results in the fabrication of thinner graphene sheets with fewer structural defects compared to the anodic exfoliation [72, 133-135]. As it can be understood from Figure 5-6, in this cell design, the large pH gradient makes it difficult to measure the accurate pH values on the surface of BE. Therefore, the quantitative study of pH effect on the properties of fabricated materials needs a purposely designed bipolar cell to be conducted in future studies.

Furthermore, the alkyl (C-H) group was found to be the dominant functional group on the negative feeding electrode of G– configuration (Figure 5-4 (b)), while hydroxyl (C-OH) peak had the highest intensity in the spectra of the samples fabricated in G+ configuration (Figure 5-4 (a)). In addition, the carbonyl (C=O) functional groups were not detected on either positive electrode, negative electrode, or free-standing materials fabricated using the G– configuration, but were detected in the samples of the G+ configuration. This indicates that a lower level of oxidation occurred during the cathodic exfoliation of graphite compared to the anodic one. The same observation has also been reported for the exfoliation of graphene through the conventional cathodic exfoliation process [133, 134, 136].

It is worth noting that the exfoliated graphene nanosheets could have either negative or positive charges depending on the dominant functional groups that are added to their structure. Based on the FTIR results, we found the exfoliated freestanding graphene in DI water is mainly GO. Typically GO is negatively charged, which is well studied by different research groups []. When these negatively charged nanosheets migrate towards the positive feeding electrode electrophoretically, they will be adsorbed and deposited on the positive feeding electrode in a layer-by-layer assembly fashion (either on the stainless steel or on top of the previously deposited graphene layers). This could explain the graphene restacking that occurred on the positive feeding electrode of the BPE cell. On the other side, although negatively charged nanosheets tend to electrophoretically migrate against negative feeding electrode, the diffusion still makes it probable to find negatively charged nanosheets close to the negative electrode (based on the statistical interpretation of entropy [137]). Once they reach to the surface, electrochemically reduction can partially reduce the nanosheets and cause them to be deposited on the surface. Once the partially reduced graphene gets attached on the negative feeding electrode, the net negative charge will expel the free standing GO nanosheets which can contribute to the vertical aligning of the rGO on the negative feeding electrode to minimize the repulsive forces.

Finally, from the current-time curves (Figure 5-3), the cell current of the G+ configuration increased significantly over time, whereas it stayed almost constant for the G– configuration. To explain the reason behind this difference, first, it should be noted that in our previous study, we showed that the rise in the current is mainly due to the acceleration of graphite exfoliation [5]. Second, it should be pointed out that in the vicinity of graphite in the G+ configuration (anodic pole of BE), the localized concentration of OH^- OH^- ions

as well as pH decrease over time due to the consumption of OH^- on the BE surface during the water electrolysis ($4OH^- \rightarrow 2H_2O + O_2 + 4e^-$) [6, 138]. Third, Su et al. reported that the decrease in pH could accelerate graphite exfoliation [71]. By considering these three points, the increase in the total cell current could be attributed to the decrease of local pH value and acceleration of the exfoliation rate. Moreover, and as expected, the increase in the current and deposition rate were smaller when stirring was added to the G+ configuration (Figure 5-3 (a)) since stirring retards the localized change in pH. In contrast, for the case of G– configuration, H^+ ions had less impact on the exfoliation process compared to OH^- in terms of total current and deposition rate, which could be attributed to pH-dependent exfoliation of graphite.

5.6 Conclusion

In summary, a modified BPE system has been developed to decouple the anodic and cathodic exfoliation processes by using an electrically-connected graphite-platinum couple. In this configuration, either anodic or cathodic exfoliation of graphite was halted depending on the polarization of the platinum. The exfoliation mechanisms are discussed and the results showed that graphene was exfoliated from the graphite rod and deposited on feeding electrodes regardless of the graphite polarization (i.e. in both G+ and G– configurations); however, the morphology, total cell current, and the deposition rate vary due to exfoliation time, polarity of the graphite and stirring/non-stirring. Our results show either anodic, cathodic, or a combination of these two exfoliation mechanisms can be utilized to manipulate the exfoliation and surface condition of fabricated graphene through

BPE. The anodic exfoliation provides graphene with a broader range of functional groups. The cathodic exfoliation resulted in the deposition of thinner and larger graphene sheets. The combination of these two mechanisms could increase the exfoliation and deposition rate.

6. In-Situ Exfoliation and Integration of Vertically Aligned Graphene for High-Frequency Response On-Chip Microsupercapacitors

6.1 Introduction

Given the recent developments in the fabrication of microelectronic devices, embedded micro-sized energy storage systems that can be directly integrated with other microelectronic compounds are becoming more and more in demand [16, 38, 39]. Micro-supercapacitors (MSCs) are considered as promising alternatives to bulky electrolytic capacitors or batteries for on-chip applications given their simplicity in design, long lifetime, low heating effects, and safety considerations [9-15]. In addition, being two-terminal devices, MSCs can be connected in parallel and/or in series to meet the required capacity, voltage, and current of the intended load [41]. Supercapacitors can be categorized into three groups, i.e, electrical double-layer capacitors (EDLCs), pseudocapacitors and hybrid capacitors, based on the charge storage mechanisms [23, 31, 34], and as such, their specifications and applications vary accordingly [15, 23]. EDLCs store the electrical charge in the double-layer structure formed at the electrolyte/electrode interface and exhibit much faster response when compared to the other two types [31, 34, 41, 42]. However, the frequency response of EDLCs, which is typically in the range of several hundred milliseconds to several seconds, is still lagging behind that of conventional aluminum electrolytic capacitors (AEC), which is typically in the range of several milliseconds. When applied to MSCs, even though the short diffusion paths between the microelectrodes lower their time constants, the mechanistic weakness still limits their high-frequency on-chip

applications, which necessitates exploring alternative strategies to further enhance the frequency response of MSCs.

Among all the different available and demonstrated approaches [15, 33, 34, 43, 44, 46, 50], supercapacitors made by vertically aligned graphene electrodes, showed the most remarkable performance at high frequencies since this unique microstructure can minimize the electronic and ionic resistances and therefore increase the response rate of the device. Vertically aligned graphene electrodes have been successfully fabricated by various plasma-enhanced chemical vapor deposition techniques [45, 139-141] or thermal decomposition of SiC [47]. However, the complexity, associated costs, and the elevated temperatures and vacuum system requirements make these methods challenging for device fabrication [34, 47, 50]. Particularly, and to the best of our knowledge, no studies have been reported vertically aligned graphene on miniaturized interdigitated supercapacitors. As an alternative, bipolar electrochemistry (BPE) has been recently developed as an in-situ three-in-one exfoliation, reduction, and deposition method to fabricate high quality layered or vertically aligned 2D materials (graphene [5-7, 142, 143] and phosphorene [28, 85, 143]) in DI water at room temperature which is environmentally friendly, simple, and cost-effective.

Typically, a BPE cell consists of a conductive material (bipolar electrode (BE)) placed wirelessly between two feeding electrodes of a conventional cell. When the conductivity of the BE is higher than that of the electrolyte, an interfacial potential difference (IPD) appears between the farthest edges of the BE. The magnitude of this IPD linearly depends on the distance between the farthest edges of the BE and the electric field in the solution. In the case that the IPD value is high enough, it can initiate redox reactions on the (anodic

and cathodic) edges of BE [77, 81] or electrochemical exfoliation of the BE if it is made of layered Van der Waals materials, such as graphite or black phosphorous [5-7, 28, 85, 131, 142, 143].

Motivated by the capabilities and versatility of the BPE method (e.g., vertically aligned reduced graphene oxide (rGO) on the negative feeding electrode [5]) and our better understanding of the mechanistic pathways of the exfoliation and deposition sequences [143], in this work we investigate the compatibility of BPE with other semiconductor processing for the development of high-performance on-chip MSC with unique vertically aligned graphene microstructure. First, gold interdigitated micro-current collectors (Au-MCC) were fabricated using photolithography method. BPE was then used to in-situ exfoliate and deposit vertically aligned rGO on Au-MCC. The electrochemical performance of the fabricated MSCs in the time domain and frequency domain has been investigated, and the results showed outstanding capacitive storage capability at high frequencies (e.g., ~ 65.2 μF cm^{-2} at 120 Hz and 55 μF cm^{-2} at 1000 Hz). The MSC device has been tested and validated in a practical AC line filtering circuit which is promising for on-chip microelectronic applications.

6.2 Materials and Methods

6.2.1 Fabrication of Au-MCC

The fabrication of gold interdigitated MCC was conducted by photolithography. Figure 6-1 (a) schematically depicts the fabrication process, which consists of the following steps: (1) A 4" Si/SiN (100) wafer was first spin-coated by hexamethyldisilazane (HMDS) as the

adhesion promoter and then by AZ 1518 (from Microchemicals) at a rotational speed of 500 rpm for 10 s and then 2900 rpm for 30 s. (2) Soft baking of the wafer was conducted for 60 s at 100°C on a hot plate. (3) The wafer was then patterned by an OAI 800 mask aligner with a UV dose of 60 mJ cm^{-2}. (4) After the exposure step, the development of the photoresist was carried out using diluted AZ 400 MIF (4:1 volume ratio of DI water to the developer) for ~60 s. (5) The wafer was baked for 20 s at 65°C and 70 s at 115°C. (6) Next, O_2 plasma cleaning was conducted to remove the remaining photoresist by reactive ion etching (RIE) at 100 W power for 60 s. (7) Then, e-beam evaporation was used for metallization of Cr/Au (20/100 nm) using a CHA evaporator. (8) Lift-off was carried out in sonication bath using AZ EBR solvent for 2 hours, followed by acetone and isopropyl rinsing, and then N_2 drying. (9) To avoid the lateral growth and deposition of graphene in between the microelectrodes, a sacrificial photoresist layer was applied and patterned between the interdigitated electrodes by repeating steps 1 to 5 on the wafer with fabricated gold microelectrodes. The optical microscopic checkout confirmed the fidelity of pattern transfer with interdigitated Au-MCC (thickness of ~120 nm) separated by sacrificial photoresist patterns (thickness of ~2 μm). There are 32 interdigital fingers in total on each Au-MCC (16 for each electrode side) with lengths and widths of 6040 μm and 100 μm, respectively. This gives the geometrical surface area of 9.66 mm^2 on each side of Au-MCC. Based on the footprint area and the thickness of the electrodes, the device occupied as low as ~0.04 mm^3 without packaging. In addition to Au-MCC, carbon cloth and interdigitated carbon microelectromechanical systems (C-MEMS) with 3D structure have also been used as the current collector to confirm the versatility of BPE process for deposition of rGO on

different substrates. The experimental details about C-MEMS fabrication procedure have been reported in our previous studies [9-11].

6.2.2 Graphene Synthesis and Deposition

Figure 6-1 (b) shows a schematic drawing of the modified BPE cell in DI water employed for deposition of vertically aligned rGO on the Au-MCC, which is mounted on the negative side of feeding electrode (stainless steel 316, 2×1 cm^2). The distance between the two feeding electrodes is 9 cm. Two graphite rods were placed between the feeding electrodes in a way that the distance of the farthest edges of the two was 7 cm. These two graphite rods were electrically wired outside of the electrolyte. The BPE cell was designed and 3D printed (using PLA filament). A direct current (DC) voltage of 45 V was applied across the feeding electrodes for a duration of 24 hours. Magnet stirring was added to the cell during the BPE process using a 1 cm magnet rod with a rotational speed of about 150 rpm. By the end of the BPE process, the MSCs were detached from the stainless steel feeding electrode and immersed in AZ EBR for 120 s to remove the sacrificial photoresist between the fingers. Finally, the substrates were thoroughly rinsed in isopropyl and DI water, and then dried with N2 gas.

6.2.3 Materials Characterization

The morphology of the deposited graphene on the gold interdigitated micro current collector was analyzed on a JEOL 7000 scanning electron microscopy (SEM). Raman analysis was carried out on a Raman spectrometer (in backscattering configuration) equipped with an argon-ion laser (Spectra Physics Model 177, 514 nm, 400mW) and HoloSpec f/l.8i, Kaiser optical spectrograph.

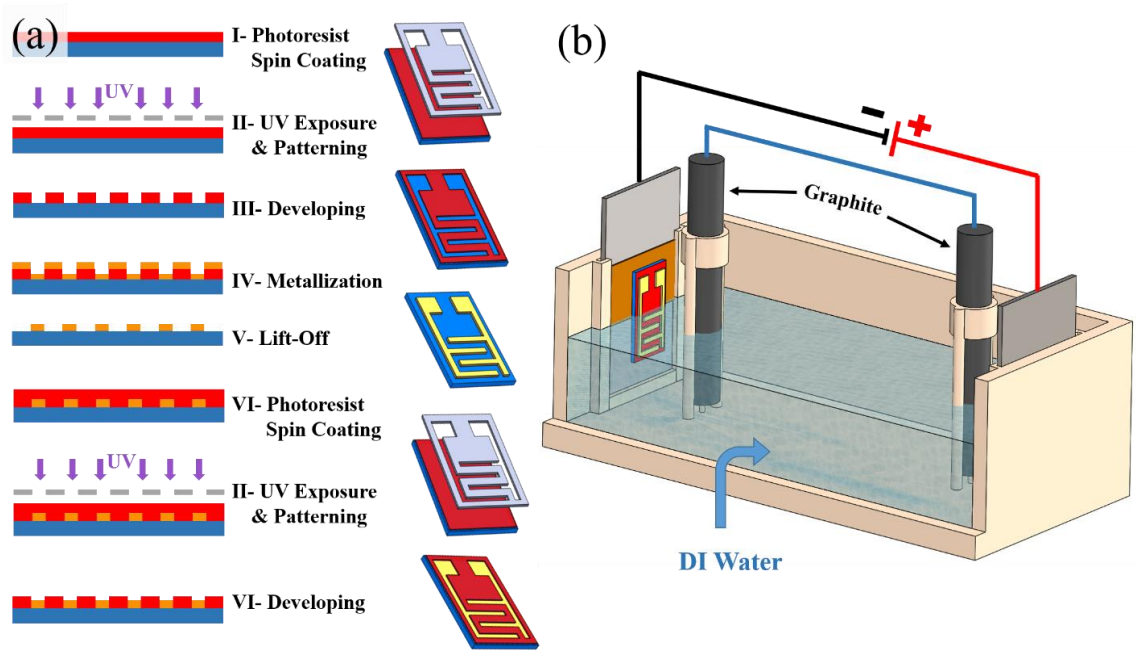

Figure 6-1: (a) Illustration of the fabrication process of the interdigitated Au-MCC. (b) Schematic drawing of the BPE setup.

6.2.4 Electrochemical Characterization of MSCs

A VMP3 Bio-Logic multichannel potentiostat was used to evaluate the electrochemical performance of fabricated devices using cyclic voltammetry (CV), galvanostatic charge/discharge (GCD), and electrochemical impedance spectroscopy (EIS) techniques. The CV tests were conducted at scan rates from 2 to 5000 mV s^{-1}, and the GCD tests at loading currents from 25 to 250 µA cm^{-2}, both with the potential limits 0 to 0.8 V. For EIS measurements, the fully discharged MSCs (the DC voltage was around 0 V) were subjected to a 30 mV amplitude sinusoidal voltage with stepped frequencies from 1 MHz down to 100 mHz (6 frequency points per decade). The reported current and capacitance are normalized by the surface area of the microelectrodes, i.e., 9.66 mm^2.

6.2.5 AC line Filtering Circuit

To evaluate the performance of MSC as an AC line filter, it was used in standard AC to DC circuit in which an input 60 Hz, V_{peak}=±1.0 V sinusoidal wave was rectified through a diode bridge resulting in a 120 Hz, V_{peak}≃+0.8 V rectified wave. Both open circuit and loaded circuit (with a 39 kΩ resistor) were used for validating the filter performance. The MSC was separated by a switch from the rest of the circuit, so that the change in the output waveform of the filter could be monitored. Reference experiments were carried out using a commercial AEC (rated 10 μF, 16 V).

6.3 Results and Discussion

Figure 6-2 (a) shows a low-magnification SEM micrograph of the finger-like microelectrodes. Figure 6-2 (b) presents a high magnification SEM of the deposited graphene by BPE, which shows the formation of high surface area and porous structure of vertically aligned graphene nanosheets. It can be seen that graphene sheets (with the dimension of several hundred nanometers) formed a porous network on the current collector. Such geometrical features are expected to be favorable for the high-frequency response and power performance of MSC devices by facilitating the rapid mitigation of ionic species. Figure 6-2 (c) presents the Raman spectrum of the deposited graphene on the Au-MCC substrates, depicting typical Raman peaks of graphene materials (i.e., D-band at ~1350 cm^{-1}, G-band at ~1609 cm^{-1}, 2D peak at ~2700 cm^{-1}, and D+G peak ~2910 cm^{-1}). It can be seen that the intensity related to D-band is lower than the one of the G-band, which confirms the formation of highly reduced graphene oxide (rGO) on the surface (the

I_D to I_G ratio is about 0.78) [5, 63, 94, 95]. Similar results have been reported in our previous study for the graphene deposited on the stainless steel on the negative feeding electrode of the BPE setup [5].

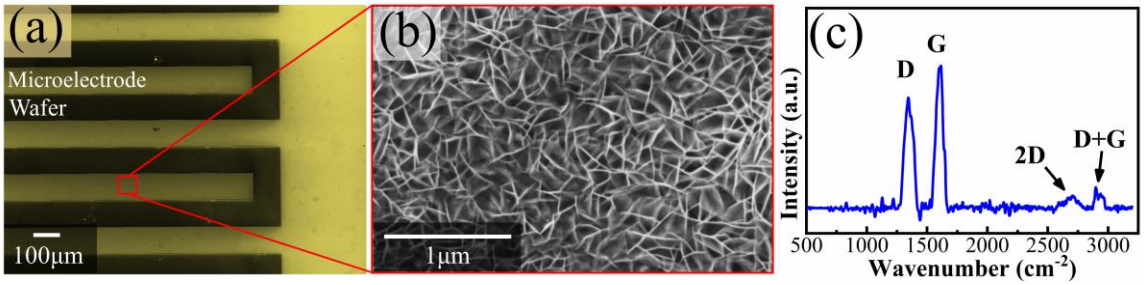

Figure 6-2: (a) low magnification SEM image of microelectrodes. (b) SEM image of the vertically aligned graphene nanosheets deposited on the microelectrodes. (c) Raman spectra of deposited graphene.

In addition to the gold microelectrode substrate, carbon cloth (
Figure 6-3 (a) and (b)) and C-MEMS microelectrodes (
Figure 6-3 (c) and (d)) have also been tried as current collectors in the BPE process. It is clear from the figures that vertically aligned graphene nanosheets were successfully deposited on all of these substrates, indicating the BPE process's compatibility and versatility for depositing rGO on various types of conductive substrates.

the microdevice fabrication procedure was modified in a way that the MCC ended up with a thick sacrificial photoresist layer between the gold microelectrodes. To illustrate the reason for this modification, a sample without this extra layer of photoresist was prepared and used in the BPE cell. The SEM image of this sample after deposition of rGO is provided in Figure 6-4, which clearly shows the lateral growth of rGO between the gold fingers on top of the silicon nitride wafer (non-conductive material). The morphology and distribution of these rGO nanosheets reveal that the deposited material on the wafer acted itself as a

conductive substrate favorable for the electrophoretic deposition of incoming nanosheets. The lateral growth of rGO nanosheets between adjacent microelectrodes will eventually cause short-circuiting when employed as MSC electrodes. Figure 6-5 (a) shows an SEM micrograph of a sample that was prepared by the modified photolithography method developed in this study. The SEM was taken at the edge of a gold microelectrode after the completion of the BPE process and before dissolving the sacrificial photoresist layer. It is evident that graphene's lateral growth also took place for this sample, and rGO nanosheets were also deposited on top of the photoresist in addition to the gold microelectrode. Figure 6-5 (b) shows the SEM image of the same sample after dissolving the photoresist in the AZ EBR solvent. It proves that applying the sacrificial photoresist between the electrodes followed by lift-off is an effective way to eliminate unwanted depositions.

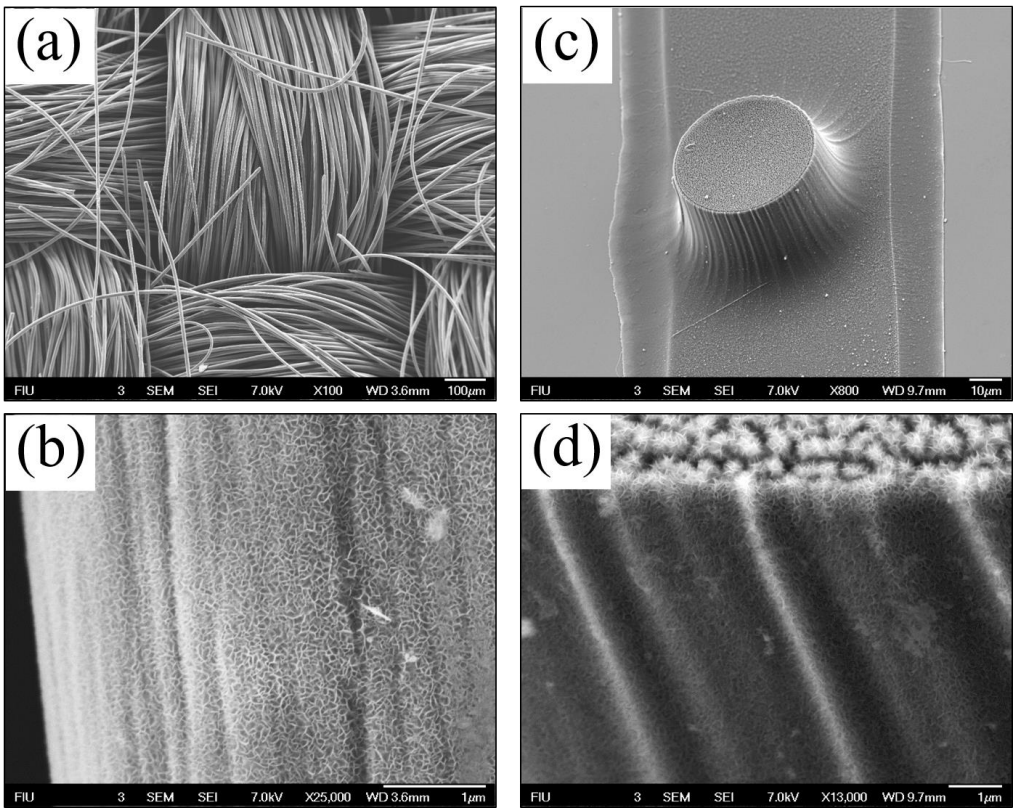

Figure 6-3: SEM image of the substrate and vertically aligned graphene nanosheets deposited on (a) and (b) carbon cloth, (c) and (d) C-MEMS microelectrode.

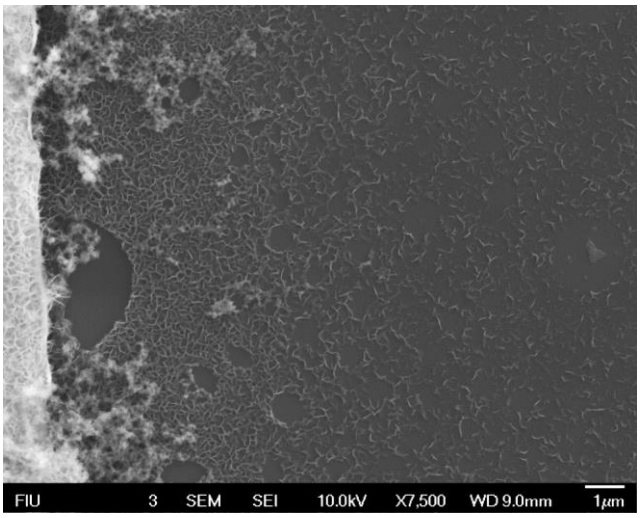

Figure 6-4: SEM image of deposited graphene between the gold fingers.

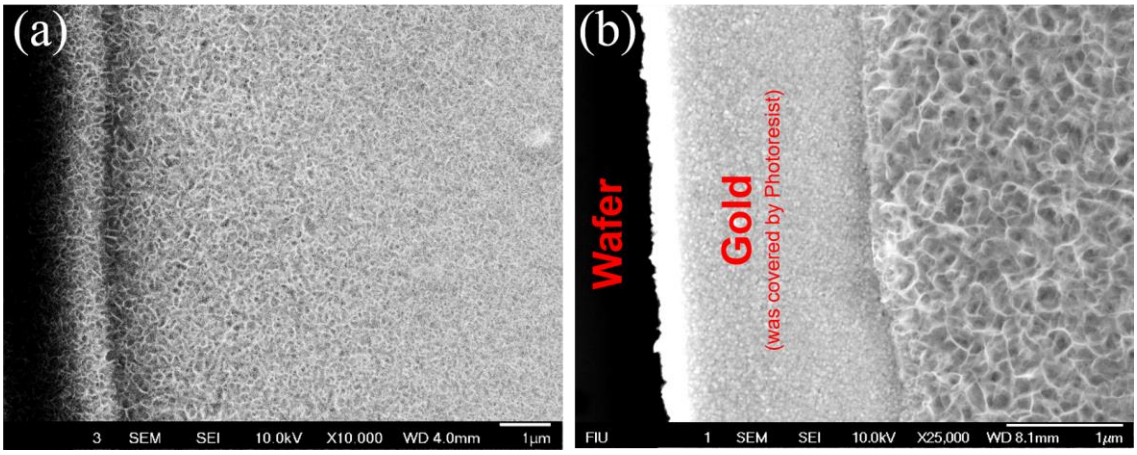

Figure 6-5: SEM image of deposited graphene on the microdevice fabricated by modified photolitography process, (a) after BPE process, (b) after lift-off process.

CV, GCD, and EIS measurement techniques were conducted to study the time domain and frequency domain performance of rGO-MSC, and as-is Au-MCC substrate for comparison. Figure 6-6 (a) and Figure 6-7 (a) present the CVs results of rGO-MSC and Au-MCC, respectively. The shapes of the curves are almost rectangular without any detectable

current peaks over the covered voltage window from 0 to 0.8 V. This indicates that no faradic reactions were taking place on the electrodes of these devices and that the charge storage mechanism is predominantly physical through the formation of double-layer structure (as expected for carbon-based electrodes). An increased tilting of the CV profiles with respect to the x-axis at higher charging/discharging rates was also remarked, which is indicative of increased resistive behavior in the device at the expense of capacitive energy storage.

The GCD results of rGO-MSC and Au-MCC at different current densities are shown in Figure 6-6 (b) and Figure 6-7 (b), respectively. The GCD curves show relatively symmetric and quasi-triangular shapes at all tested current densities indicating close-to-ideal capacitive behavior of both rGO-MSC and Au-MCC. In the GCD test, the sudden voltage drop at the beginning of the discharge curve is typically associated with the irreversible ohmic losses (iR_s drop) in the series resistance of the MSCs. The GCD curves obtained in this study do not show a substantial voltage drop for any of the current densities we applied, indicating relatively low internal resistance of the MSCs. A comparison between the discharge time of the Au-MCC and rGO-MSC devices reveals the deposition of rGO by BPE technique can significantly increase the capacity of the MSCs for storing the charge. It is evident that discharge time increased by about 30 times (from 0.126 s to 3.829 s) at the discharge current of 25 $\mu A\ cm^{-2}$.

The non-ideal capacitive features in the current-voltage and voltage-time profiles are well-known for electrochemical capacitive devices, i.e., nonlinear charge-voltage profiles and thus non-constant, voltage, and rate-dependent characteristic capacitance function [144-146]. In response to an applied voltage, a net charge is accumulated on the surface of an

electrode, which brings electrolytic counterions from the immediate vicinity of the electrode surface to rearrange themselves accordingly to balance this charge. The layer of charge in the electrolyte is then balanced by the formation of a second layer of concentration-dependent, diffuse charge. Subsequently, when the electrode voltage is changed (and depending on its rate), as is the case of CV tests, for instance, the ions in the double-layer structure rearrange and generate a current. Therefore, from the current-voltage dynamics (CV) and voltage-time profiles (GCD) it is difficult to estimate a characteristic capacitive function as commonly done in the literature from the simple division of charge by voltage. Nonetheless, for the sake of comparison, we computed the ratio $\bar{\mathrm{C}} = 2\int \mathrm{i(V)dV}/(v\Delta \mathrm{VA})$ (in units of $\mathrm{C.V^{-1}cm^{-2}}$) using data from the CV curves, where $\bar{\mathrm{C}}$ can be viewed as averaged value relating the voltage-averaged current (expressed by $\bar{\mathrm{I}} = \Delta \mathrm{V^{-1}} \int \mathrm{i(V)dV}$) to the voltage scan rate v, and normalized with respect to the microelectrode's geometric area A on each side of the MSCs. The computed values of $\bar{\mathrm{C}}$ at the different scan rates of 2, 10, 50, 100, 200, 1000 and 5000 mV s^{-1} were found to be 640, 454, 346, 315, 281, 194, and 161 $\mathrm{C.V^{-1}cm^{-2}}$ (equivalent to μF cm^{-2}) respectively for rGO-MSC, and 61, 27, 12, 9, 8, 7 and 5 $\mathrm{C.V^{-1}cm^{-2}}$ (equivalent to μF cm^{-2}) respectively for Au-MCC device. Applying the cyclic triangular excitation in CV with the voltage scan rates of 2, 10, 50, 100, 200, 1000 and 5000 mV s^{-1} is similar to exciting the device at the fundamental frequencies of 1.25 mHz, 6.25 mHz, 31.25 mHz, 62.5 mHz, 125 mHz, 625 mHz, and 3.125 Hz respectively, which explains the decrease in values of $\bar{\mathrm{C}}$ as the scan rate is increased, as will be discussed further in the EIS results below.

In order to investigate the capacity retention and cyclic performance of the fabricated devices, an rGO-MSC was charged and discharged 50,000 successive times at the current

density of 25 μA cm^{-2}. Figure 6-6 (c) shows a plot of discharge capacity vs. cycle number; the relative increase of about 12 % in the capacity from the first to the last cycle without fading indicates an excellent stability performance of the device. Such behavior has been reported in other research studies [10] and can be explained by the electrochemical activation of the carbon materials during the charge-discharge process and/or an increased wettability of the electrodes.

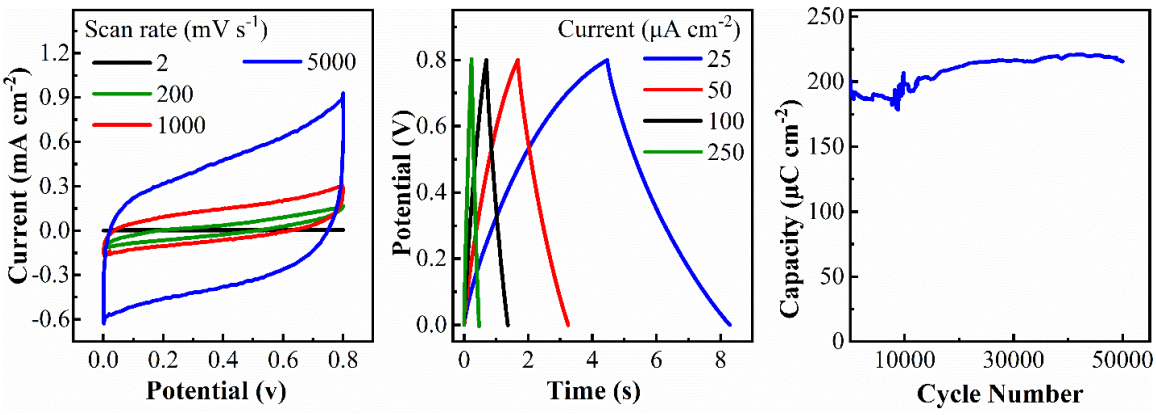

Figure 6-6: (a) Cyclic voltammetry at different scan rates, (b) galvanostatic charge-discharge results at different current densities, and (c) the cycling performance (charge-discharge at 25 µA cm^{-2}) of the fabricated rGO-MSC.

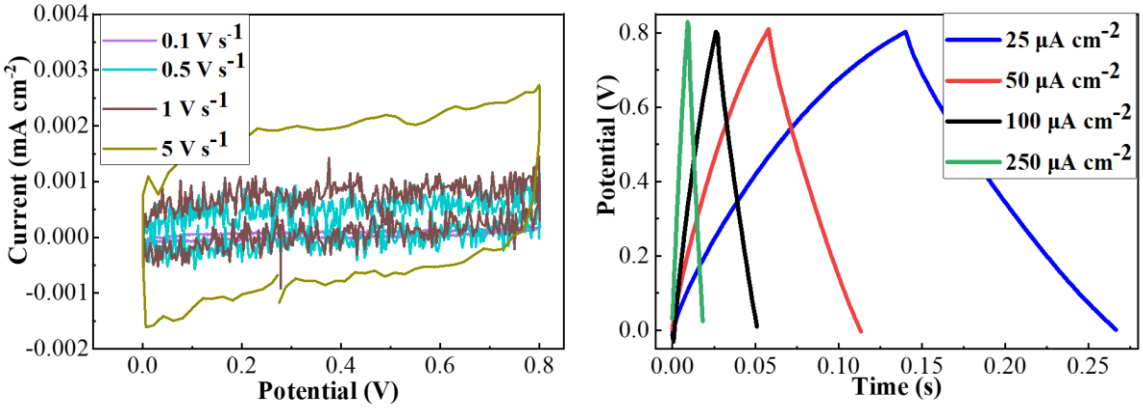

Figure 6-7: (a) Cyclic voltammetry at different scan rates, (b) galvanostatic charge-discharge results at different current densities of the Au-MEMS current collector.

EIS analysis was conducted to study the performance of the MSCs as a function of frequency. The Nyquist plots, which are the illustration of the imaginary (-Im(Z)) versus real (Re(Z)) parts of the impedance, are presented in Figure 6-8 (a). The impedance of an ideal capacitor is purely imaginary and does not have a real part (i.e., $Z=-j/(\omega C)$ with C being the capacitance and ω the angular frequency), i.e., vertical line parallel to the y-axis. Both Au-MCC and rGO-MSC (fresh or after 50000 of charge/discharge cycles) showed

some small deviations from the ideal capacitive behavior without any sizable, diffusion-related Warburg region. Therefore, we used an equivalent circuit model of a series resistance R_s with a constant phase element (CPE) of total impedance being [5, 106, 107]

$$Z = R_s + \frac{1}{(j\omega)^{\alpha} C_{\alpha}} \tag{6-1}$$

to fit the data from 100 mHz to about 50 kHz. In this model, the value of α is between 1 and 0, C_{α} is a positive constant in units of F s^{a-1}, and $j^{\alpha} = \cos\left(\frac{\alpha\pi}{2}\right) + j\sin\left(\frac{\alpha\pi}{2}\right)$ (Euler formula) [5, 106, 107]. At the limiting values of 1 and 0 for α, the impedance function simplifies to that of an ideal capacitor and a resistor, respectively. Using equation 1, and by manually setting the values of R_s taken from the high-frequency intercepts of the impedance data with the real axis, we found an impedance phase angle $-\frac{\alpha\pi}{2} = -83$ deg for Au-MCC device, whereas the phase angle for rGO-MSC is -73 deg before cycling and -78 deg after cycling.

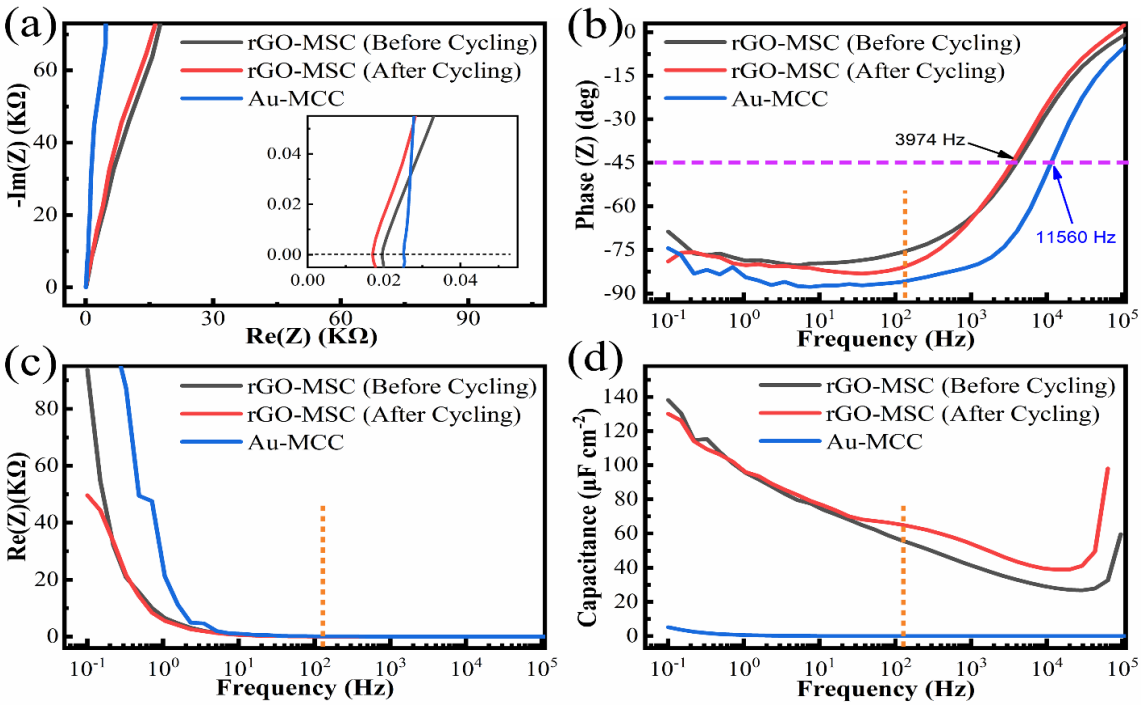

Figure 6-8: (a) Complex-plane representation of real vs. imaginary part of impedance (Nyquist plot), (b) impedance phase angle as a function of frequency (bode phase plot), (c) the device resistance as a function of frequency, and (d) specific areal capacitance as a function of frequency, for Au-MCC and rGO-MSC before and after cycling.

This can also be illustrated from the Bode phase plots in Figure 6-8 (b), knowing that the phase angle for an ideal capacitor is −90 deg, independently of the frequency and voltage. As it can be seen, all of the devices showed some deviations from the ideal capacitive behavior with relatively constant phase angle in the low-frequency region (lower than ~1000 Hz for rGO-MSCs and lower than ~5000 Hz for Au-MCC). The minimum phase angle for rGO-MSC after cycling and Au-MCC were -83.2 deg and -87.7 deg, respectively. Moreover, as the frequency increased, the phase angles tended quickly towards the resistive behavior of zero impedance phase angle. When the phase angle is between -90 deg and -45 deg, the imaginary part of the impedance is larger than the real part. The frequency at which the imaginary and real parts become equal (i.e., phase angle is -45 deg) is called cut-

off frequency or characteristic frequency (f_0) that is commonly used as a figure of comparison between devices (Table 6-1). This parameter reveals up to what frequency range the device can be more effectively used as capacitive energy storage, albeit with some resistive losses that depend on the extent of the dispersion coefficient α. The inverse of the cut-off frequency is referred to the relaxation time constant ($\tau_0=1/f_0$), which is the minimum time needed to discharge all the energy from the device with an efficiency greater than 50% [9, 147]. From Figure 6-8 (b), the cut-off frequency for Au-MCC was found to be as high as 11560 Hz. For rGO-MSC we found a frequency of 3974 Hz for the freshly prepared device, whereas, after 50000 consecutive charge/discharge cycles with 25 μA cm^{-2}, that value dropped to just 3486 Hz, attesting to the excellent (mechanical and chemical) stability of the rGO material and the adopted MSC design and fabrication technique. The corresponding relaxation time constants are 8.6 μs for Au-MCC, and 251 μs and 286 μs for the rGO-MSC before and after cycling, respectively. Compared to other microcapacitors [18, 19, 148-151], our results indicate that BPE based vertically aligned rGO delivered one of the shortest time constants.

The real part of the impedance as a function of frequency for the tested devices is plotted in Figure 6-8 (c). All devices show very low resistance (0.03 kΩ) at frequencies higher than 1 Hz. Specifically, at 120 Hz, the devices show mostly capacitive behavior with negligible resistive behavior. The capacitance of MSCs at different frequencies can be computed from $\mathrm{Im}(Z)=-j/(\omega C)$, where $\omega = 2\pi f$, which has been further normalized with respect to the geometrical area of the current collector at each side. The plot is provided in Figure 6-8 (d). At the frequencies of 0.1 Hz, 1 Hz, and 1250 Hz, the corresponding capacitance for rGO-MSC after 50000 of GCD cycles was found to be 130 μF cm^{-2}, 96 μF

cm^{-2}, and 52 μF cm^{-2} respectively, whereas for Au-MCC it was 5.29 μF cm^{-2}, 0.59 μF cm^{-2} and 0.0011 μF cm^{-2} , respectively. These results are consistent with those of CV and GCD tests.To put things into perspective, some recently reported performances of MSC designed to operate at high frequencies and AC filtering applications are summarized in table 6-1. The data is summarized based on the characteristic frequency (f_0), the phase angle at 120 Hz (φ_{120}), and specific areal capacitance computed at 120 Hz either using frequency domain analysis or at 200 V s^{-1} (i.e., the fundamental frequency of 100 Hz for a voltage window of 1 V). One can appreciate that the rGO-MSC fabricated in this study are one of the best performing devices. It is worth noting that, as reported recently in [144-146], the frequency-domain definition of capacitance being the division of frequency-domain charge by voltage is better recommended for characterizing non-ideal capacitive devices as it is in line with the definition of impedance. Furthermore, if one assumes such a definition, we believe the appropriate way for computing the corresponding time-domain capacitance function is by deconvolution (convolution theorem of the Fourier transform) and not the division of charge by voltage as done for the computation of $\bar{C}$.

Table 6-1: The performance of different micro-supercapacitors fabricated to operate in AC line filtering application

Materials	$\boldsymbol{\varphi_{120}}$ **(°)**	$\boldsymbol{f_0}$ **(Hz)**	$\boldsymbol{C_A}$ **(μF cm^{-2})**	**Ref**
Azulene-bridged coordination polymer framework (PiCBA)	-73	3620	0.014[a,b] (at 120 Hz)	[152]
direct laser writing of graphene made from chemical vapor deposition	-76.2	2025	15[a] (at 200 V s^{-1})	[19]

Charge transfer salt and graphene heterostructure-based	-73.2	3056	151 (at 120 Hz)	[148]
Metallic 1T-Phase MoS_2	-79 [a]	1221	NA	[149]
RIE reduced graphene oxide	-68 [a]	3579	13.5 (at 200 V s^{-1})	[18]
Composite of MXene and MWCNT	-79 [a]	2000 [a]	600[a] (at 120 Hz)	[150]
Inkjet-Printed NiO	-25 [a]	33	NA	[151]
Catechol-coordinated framework film (Cu-DTHAB film)	-84	16374	0.96[a,b] (at 120 Hz)	[153]
High aspect ratio 3D nanoporous gold	-61	250 [a]	800 [a] (at 200 V s^{-1})	[154]
Oriented coordination polymer (Cobalt benzenetetramine tetrahydrochloride)	-78.6	6812	9 [a,b] (at 120 Hz)	[155]
Reduced Graphene Oxide and Carbon Nanotube Composites	-62	208	NA	[15]
B/N-Enriched semi-conductive polymer film	-67	1910	28 [a,b] (at 200 V s^{-1})	[156]
Present work	**-81.2**	**3486**	**65.2 (at 120 Hz)**	

a: Extracted from a graph of the original article, which may have caused some minor errors in the data readout

b: The data is converted from volumetric specific capacitance to the specific areal capacitance.

Finally, in order to evaluate the practical application of the fabricated rGO-MSC at high frequencies, it has been tested in an AC - DC filtering circuit (Figure 6-9 (a), see section 2.5 for more details). The voltage output when the rGO-MSC device was not connected to any load (R=∞) is illustrated in Figure 6-9 (b). As evident, the pulsing 120 Hz, Vpeak≃+0.8 V rectified signal was perfectly flattened when the rGO-MSC was connected to the circuit (switch on). However, it is worth noting that it is essential to have a parallel load to the capacitive device in order to evaluate its performance in proper AC filtering

applications. The flattening can be done at open circuit conditions with any device that has even a parasitic capacitance at the target frequency. In contrast, when a load is connected to the circuit, it will drain the stored energy from the capacitor at the moment where the input voltage is lower than that across the capacitor. In this situation, the magnitude of the fluctuations (ripple) in the flattened signal will change as a function of the stored capacity at that specific frequency. For this reason, the proper performance of the rGO-MSC device as a filtering capacitor was evaluated when a resistor (R=1 kΩ, 39 kΩ, and 100 kΩ) was added to the circuit as a working load. The typical filtering performance with a 39 kΩ resistor is plotted in Figure 6-9 (c), proving that the rGO-MSC could successfully filter the pulsing signal even when a resistor simultaneously discharged it. The same experiment has been conducted using a 10 μF AEC, as shown in Figure 6-9 (d). Although the nominal capacitance of the AEC was almost three times higher than that of the rGO-MSC device (10 μF vs. 3.13 μF at 120 Hz), their filtering effects are similar. However, the AEC (volume of about 215 mm^3) is much bulkier compared to the miniaturized on-chip MSC.

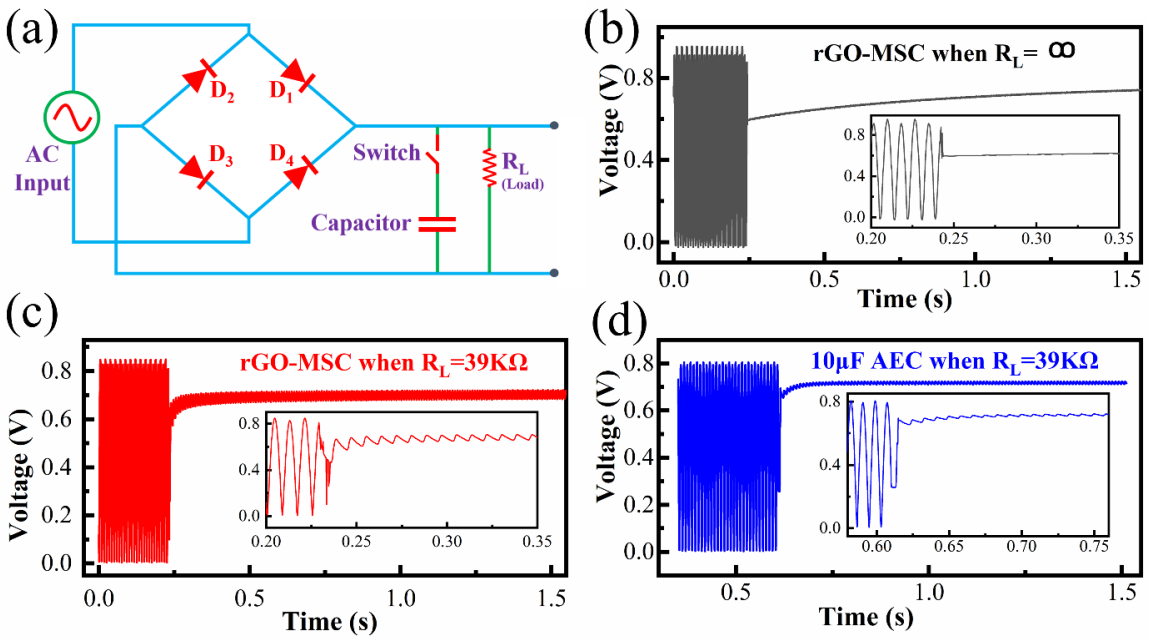

Figure 6-9: (a) Schematic of the circuit which is used as the AC to DC convertor. The smoothing capability of the rGO-MSC subjected to a rectified 120 Hz wave (b) when no load was connected to the circuit, (c) when a 39 KΩ resistor was connected to the circuit as a load, (d) when MSC was replaced by a 10 μF commercial AEC for comparison.

The high-frequency response of rGO-MSC can be attributed to the miniaturized MSCs design, and thus shorter length for ionic diffusion in response to external excitations, in addition to the highly structured, and stable vertically aligned rGO electrodes obtained by BPE, which permits high charge storage capabilities. It should also be noted that BPE has excellent compatibility with semiconductor processing and could be applied to not only graphene but also other 2D layered materials for forming morphogenic materials and interfaces with controllable morphologies, orientation, and structures. In principle, the ease of fabrication of microstructured electrodes and devices by the versatile, cost-efficient, and environmentally-friendly BPE process can be applied for fabricating other micro-sized

electronic devices such as batteries, sensors, electrochemical transistors, and memristors to cite a few.

6.4 **Co**nclusion

In summary, we demonstrated a new strategy and approach for preparing vertically aligned graphene-based MSCs for high-frequency applications. A modified BPE process was employed to deposit vertically aligned and highly reduced rGO nanosheets on an Au-MCC current collector. The lateral growth of graphene sheets between the gold fingers that can occur during the BPE process has been prevented by adding a sacrificial layer of photoresist between the fingers. The time-domain and frequency-domain electrochemical analysis of the rGO-MSC devices demonstrated excellent stability and high performance for both energy storage at close-to-dc- frequencies as well as filtering capabilities for AC line filtering applications. In particular, from EIS results, we showed that not only the deviation from ideal capacitive behavior was very small at low frequencies, but also promising capacitive performance at the high frequencies was observed. The use of rGO-MSCs in a standard AC filtering circuit showed that the device accomplished excellent flattening performance comparable to a relatively bulky and massive off-the-shelf AEC.

7. Summary and Future Works

7.1 Summary

This dissertation presents a new bipolar electrochemistry (BPE) concept that was developed for simultaneous exfoliation, deposition and reduction of graphene nanosheets on conductive substrates. Both material characteristics and electrochemical performance of the fabricated materials were evaluated and reported. Several fabrication methods have been introduced for graphene fabrication; however, none of them can do all of the aforementioned three steps together. Moreover, the method is cost-efficient, easy to control, and environmentally friendly, making it suitable for scale-up fabrication. The major findings of this dissertation are summarized as follows:

A modified BPE process was developed to exfoliate graphene nanosheets from a graphite source and electrophoretically deposit them on either positive or negative feeding electrodes of the BPE system. Further characterizations showed that the material deposited on the positive feeding electrode was highly oxidized graphene with different functional groups. On the other hand, the material deposited on the negative feeding electrode was highly reduced graphene oxide with much lower structural defects and a porous morphology. Electrochemical characterization when the materials were used in EDLCs showed high specific areal capacitance (~2mF cm^{-2} at a scan rate of 2 mV s^{-1}) with a very fast response rate (cut-off frequency of 1157 Hz) for the material deposited on the negative feeding electrode.

A novel BPE system was designed to study the mechanism of exfoliation and deposition of graphene nanosheets in the BPE system. The results proved that both anodic and cathodic exfoliation mechanisms were participating in the exfoliation of graphene nanosheets from graphite. However, the morphology, total cell current, and deposition rate vary due to exfoliation time, graphite polarity, and stirring/non-stirring. It was found that the graphene fabricated by the anodic exfoliation process had a broader range of functional groups. Moreover, it has been reported that the cathodic exfoliation of graphite resulted in the deposition of thinner and larger graphene sheets with fewer added functional groups.

Finally, a modified photolithography technique was employed to fabricate interdigitated gold micro-current collectors that had photoresist between the gold fingers. Then, the developed BPE method in the first phase of this study was employed to deposit vertically aligned graphene on the interdigitated micro-current collector. After graphene deposition, the photoresist was lifted off, and the device's performance as a micro supercapacitor was investigated in both time domain and frequency domain. The device could deliver a specific capacitance of ~640 $\mu F\ cm^{-2}$ at a scan rate of 2 $mV\ s^{-1}$. More importantly, the device showed very close to ideal behavior at frequencies lower than 1000 Hz. Particularly the phase angle could reach a low as – 83.2˚ and was -81˚ at 120 Hz.

Based on the finding in this dissertation, BPE method can be considered as a cost-efficient and environmentally friendly method to deposit high-quality graphene on any conductive substrate. The high surface area and vertically aligned microstructure of deposited graphene nanosheets can lead to the fabrication of high-performance and fast response EDLCs. The method also has the capability of being used for microdevice fabrication.

7.2 Future Works

The present work has introduced a novel approach to fabricate high-quality graphene-based electrodes for different applications such as energy storage devices and sensors. Based on the current work, the following works are recommended for future studies:

1. **Investigating the effect of different intercalating ions in the BPE process:** In this study, DI water was used as the electrolyte for the BPE process to maximize the bipolar current and simplification of mechanisms study. However, to accelerate the exfoliation process and therefore increase the yield and efficiency of the process for scale-up applications, some cathodic (Li^+, Et_3NH^+, K^+, etc.) or anodic (SO_4^{2-}, HCl^-, PO_4^{3-}, NO_3^-, ClO_4^-, Br^-, etc.) intercalation ions can be employed in the BPE process. On the one hand, each one of these ions can accelerate one of the exfoliation mechanisms; however, on the other hand, they can affect the quality and morphology of fabricated graphene, which needs more investigation.
2. **Investigating the BPE fabricated graphene for battery and sensors applications**: In the present work, the fabricated graphene electrodes were only used in supercapacitor applications; however, the unique microstructure and high quality of fabricated graphene by BPE, nominate it to be used for other applications. Graphene-based electrodes have been widely used in the fabrication of electronic devices (MOSFET transistors), electrochemical sensors (aptamer sensors, gas detection sensors) and other energy storage devices (anode for Li-Ion Batteries). The author believes if future studies prove the graphene fabricated by BPE can deliver high performance in energy storage systems and high sensitivity in electrochemical sensors,

the method can be widely used for scale-up fabrication since it is a cost-efficient and environmentally friendly approach.

3. **Co-deposition of graphene nanosheets with other 2D materials:** The synergistic effect and achieving high-performance electrodes when two different 2D materials are coupled, have been shown in literiture. BPE can be used to exfoliate and deposite varius 2D materials such as Phosphorene and MXene. Therefore, the author belives a composite of different 2D materials can be fabricated by either layer by layer deposition or co deposition approaches (using different bipolar electrodes in a BPE system). Study the possibility of composite fabrication and their performance will be helpful.

References

[1] R. Agrawal, Hybrid Electrochemical Capacitors: Materials, Optimization, and Miniaturization, (2018).

[2] R. Agrawal, E. Adelowo, A.R. Baboukani, M.F. Villegas, A. Henriques, C. Wang, Electrostatic spray deposition-based manganese oxide films—From pseudocapacitive charge storage materials to three-dimensional microelectrode integrands, Nanomaterials 7(8) (2017) 198.

[3] C. Zhong, Y. Deng, W. Hu, J. Qiao, L. Zhang, J. Zhang, A review of electrolyte materials and compositions for electrochemical supercapacitors, Chemical Society Reviews 44(21) (2015) 7484-7539.

[4] A. González, E. Goikolea, J.A. Barrena, R. Mysyk, Review on supercapacitors: Technologies and materials, Renewable and Sustainable Energy Reviews 58 (2016) 1189-1206.

[5] I. Khakpour, A. Rabiei Baboukani, A. Allagui, C. Wang, Bipolar Exfoliation and in Situ Deposition of High-Quality Graphene for Supercapacitor Application, ACS Applied Energy Materials 2(7) (2019) 4813-4820.

[6] A. Allagui, M.A. Abdelkareem, H. Alawadhi, A.S. Elwakil, Reduced graphene oxide thin film on conductive substrates by bipolar electrochemistry, Scientific reports 6 (2016) 21282.

[7] A. Allagui, J.M. Ashraf, M. Khalil, M.A. Abdelkareem, A.S. Elwakil, H. Alawadhi, All‐Solid‐State Double‐Layer Capacitors Using Binderless Reduced Graphene Oxide Thin Films Prepared by Bipolar Electrochemistry, ChemElectroChem 4(8) (2017) 2084-2090.

[8] H. Hashimoto, Y. Muramatsu, Y. Nishina, H. Asoh, Bipolar anodic electrochemical exfoliation of graphite powders, Electrochemistry Communications 104( ) (2019) 106475.

[9] M. Beidaghi, C. Wang, Micro-supercapacitors based on three dimensional interdigital polypyrrole/C-MEMS electrodes, Electrochimica Acta 56(25) (2011) 9508-9514.

[10] M. Beidaghi, W. Chen, C. Wang, Electrochemically activated carbon micro-electrode arrays for electrochemical micro-capacitors, Journal of power sources 196(4) (2011) 2403-2409.

[11] E. Adelowo, A.R. Baboukani, O. Okpowe, I. Khakpour, M. Safa, C. Chen, C. Wang, A high-energy aqueous on-chip lithium-ion capacitor based on interdigital 3D carbon microelectrode arrays, Journal of Power Sources 455 (2020) 227987.

[12] P. Huang, C. Lethien, S. Pinaud, K. Brousse, R. Laloo, V. Turq, M. Respaud, A. Demortiere, B. Daffos, P.-L. Taberna, On-chip and freestanding elastic carbon films for micro-supercapacitors, Science 351(6274) (2016) 691-695.

[13] D. Pech, M. Brunet, P.-L. Taberna, P. Simon, N. Fabre, F. Mesnilgrente, V. Conédéra, H. Durou, Elaboration of a microstructured inkjet-printed carbon electrochemical capacitor, Journal of Power Sources 195(4) (2010) 1266-1269.

[14] B. Dousti, Y.I. Choi, S.F. Cogan, G.S. Lee, A High Energy Density 2D Microsupercapacitor Based on an Interconnected Network of a Horizontally Aligned Carbon Nanotube Sheet, ACS Applied Materials & Interfaces 12(44) (2020) 50011-50023.

[15] M. Beidaghi, C. Wang, Micro‐supercapacitors based on interdigital electrodes of reduced graphene oxide and carbon nanotube composites with ultrahigh power handling performance, Advanced Functional Materials 22(21) (2012) 4501-4510.

[16] F. Bu, W. Zhou, Y. Xu, Y. Du, C. Guan, W. Huang, Recent developments of advanced micro-supercapacitors: design, fabrication and applications, npj Flexible Electronics 4(1) (2020) 1-16.

[17] F. Wang, X. Wu, X. Yuan, Z. Liu, Y. Zhang, L. Fu, Y. Zhu, Q. Zhou, Y. Wu, W. Huang, Latest advances in supercapacitors: from new electrode materials to novel device designs, Chemical Society Reviews 46(22) (2017) 6816-6854.

[18] Z.S. Wu, K. Parvez, X. Feng, K. Müllen, Graphene-based in-plane micro-supercapacitors with high power and energy densities, Nature communications 4(1) (2013) 1-8.

[19] J. Ye, H. Tan, S. Wu, K. Ni, F. Pan, J. Liu, Z. Tao, Y. Qu, H. Ji, P. Simon, Direct laser writing of graphene made from chemical vapor deposition for flexible, integratable micro‐supercapacitors with ultrahigh power output, Advanced Materials 30(27) (2018) 1801384.

[20] P. Sharma, T. Bhatti, A review on electrochemical double-layer capacitors, Energy conversion and management 51(12) (2010) 2901-2912.

[21] H. Becker, Low voltage electrolytic capacitor, Google Patents, 1957.

[22] K.S. Novoselov, A.K. Geim, S.V. Morozov, D. Jiang, Y. Zhang, S.V. Dubonos, I.V. Grigorieva, A.A. Firsov, Electric field effect in atomically thin carbon films, Science 306(5696) (2004) 666-669.

[23] B. Lu, X. Jin, Q. Han, L. Qu, Planar Graphene‐Based Microsupercapacitors, Small (2021) 2006827.

[24] A.P. Kauling, A.T. Seefeldt, D.P. Pisoni, R.C. Pradeep, R. Bentini, R.V. Oliveira, K.S. Novoselov, A.H. Castro Neto, The Worldwide graphene flake production, Advanced Materials 30(44) (2018) 1803784.

[25] S.E. Fosdick, K.N. Knust, K. Scida, R.M. Crooks, Bipolar electrochemistry, Angewandte Chemie International Edition 52(40) (2013) 10438-10456.

[26] L. Koefoed, S.U. Pedersen, K. Daasbjerg, Bipolar electrochemistry—A wireless approach for electrode reactions, Current Opinion in Electrochemistry 2(1) (2017) 13-17.

[27] A. Rabiei Baboukani, I. Khakpour, V. Drozd, C. Wang, Liquid‐Based Exfoliation of Black Phosphorus into Phosphorene and Its Application for Energy Storage Devices, Small Structures (2021) 2000148.

[28] A.R. Baboukani, I. Khakpour, C. Wang, Bipolar exfoliation of black phosphorous into phosphorene, Google Patents, 2020.

[29] C.C. Mayorga-Martinez, N. Mohamad Latiff, A.Y.S. Eng, Z.k. Sofer, M. Pumera, Black phosphorus nanoparticle labels for immunoassays via hydrogen evolution reaction mediation, Analytical chemistry 88(20) (2016) 10074-10079.

[30] Y. Wang, C.C. Mayorga-Martinez, X. Chia, Z. Sofer, M. Pumera, Nonconductive layered hexagonal boron nitride exfoliation by bipolar electrochemistry, Nanoscale 10(15) (2018) 7298-7303.

[31] J. Libich, J. Máca, J. Vondrák, O. Čech, M. Sedlaříková, Supercapacitors: Properties and applications, Journal of Energy Storage 17 (2018) 224-227.

[32] P.T. Moseley, J. Garche, Electrochemical energy storage for renewable sources and grid balancing, Newnes2014.

[33] J.R. Miller, Perspective on electrochemical capacitor energy storage, Applied Surface Science 460 (2018) 3-7.

[34] J.R. Miller, Engineering electrochemical capacitor applications, Journal of Power Sources 326 (2016) 726-735.

[35] R. Agrawal, C. Chen, Y. Hao, Y. Song, C. Wang, Graphene for supercapacitors, the book Graphene-Based Energy Devices, ed. by Rashid bin Mohd Yusoff, Wiley-VCH, Weinheim (2015).

[36] I. Khakpour, A.R. Baboukani, A. Allagui, C. Wang, Bipolar Electrochemically Exfoliated Graphene for Supercapacitor Application, Meeting Abstracts, The Electrochemical Society, 2019, pp. 656-656.

[37] A. Afif, S.M. Rahman, A.T. Azad, J. Zaini, M.A. Islan, A.K. Azad, Advanced materials and technologies for hybrid supercapacitors for energy storage–a review, Journal of Energy Storage 25 (2019) 100852.

[38] R. Agrawal, C. Wang, On-Chip Asymmetric Microsupercapacitors Combining Reduced Graphene Oxide and Manganese Oxide for High Energy-Power Tradeoff, Micromachines 9(8) (2018) 399.

[39] J. Zhang, G. Zhang, T. Zhou, S. Sun, Recent developments of planar micro‐supercapacitors: fabrication, properties, and applications, Advanced Functional Materials 30(19) (2020) 1910000.

[40] H.-K. Kim, T.-Y. Seong, J.H. Lim, Y.-W. Ok, W.i. Cho, Y.H. Shin, Y.S. Yoon, Correlation between the microstructures and the cycling performance of RuO 2 electrodes for thin-film microsupercapacitors, Journal of Vacuum Science & Technology B: Microelectronics and Nanometer Structures Processing, Measurement, and Phenomena 20(5) (2002) 1827-1832.

[41] M. Beidaghi, Y. Gogotsi, Capacitive energy storage in micro-scale devices: recent advances in design and fabrication of micro-supercapacitors, Energy & Environmental Science 7(3) (2014) 867-884.

[42] M. Beidaghi, Z. Wang, L. Gu, C. Wang, Electrostatic spray deposition of graphene nanoplatelets for high-power thin-film supercapacitor electrodes, Journal of Solid State Electrochemistry 16(10) (2012) 3341-3348.

[43] Z. Fan, N. Islam, S.B. Bayne, Towards kilohertz electrochemical capacitors for filtering and pulse energy harvesting, Nano Energy 39 (2017) 306-320.

[44] N. Islam, M.N.F. Hoque, W. Li, S. Wang, J. Warzywoda, Z. Fan, Vertically edge-oriented graphene on plasma pyrolyzed cellulose fibers and demonstration of kilohertz high-frequency filtering electrical double layer capacitors, Carbon 141 (2019) 523-530.

[45] D. Premathilake, R.A. Outlaw, S.G. Parler, S.M. Butler, J.R. Miller, Electric double layer capacitors for ac filtering made from vertically oriented graphene nanosheets on aluminum, Carbon 111 (2017) 231-237.

[46] M. Cai, R.A. Outlaw, R.A. Quinlan, D. Premathilake, S.M. Butler, J.R. Miller, Fast response, vertically oriented graphene nanosheet electric double layer capacitors synthesized from C2H2, Acs Nano 8(6) (2014) 5873-5882.

[47] S. Zheng, Z. Li, Z.-S. Wu, Y. Dong, F. Zhou, S. Wang, Q. Fu, C. Sun, L. Guo, X. Bao, High packing density unidirectional arrays of vertically aligned graphene with enhanced areal capacitance for high-power micro-supercapacitors, ACS nano 11(4) (2017) 4009-4016.

[48] W. Kuang, H. Yang, C. Ying, B. Gong, J. Kong, X. Cheng, Z. Bo, Cost-effective, environmentally-sustainable and scale-up synthesis of vertically oriented graphenes from waste oil and its supercapacitor applications, Waste Disposal & Sustainable Energy (2021) 1-9.

[49] D. Aradilla, M. Delaunay, S. Sadki, J.-M. Gérard, G. Bidan, Vertically aligned graphene nanosheets on silicon using an ionic liquid electrolyte: towards high performance on-chip micro-supercapacitors, Journal of Materials Chemistry A 3(38) (2015) 19254-19262.

[50] J.R. Miller, R. Outlaw, B. Holloway, Graphene double-layer capacitor with ac line-filtering performance, Science 329(5999) (2010) 1637-1639.

[51] K.S. Novoselov, D. Jiang, F. Schedin, T.J. Booth, V.V. Khotkevich, S.V. Morozov, A.K. Geim, Two-dimensional atomic crystals, Proceedings of the National Academy of Sciences of the United States of America 102(30) (2005) 10451-10453.

[52] Y. Cao, V. Fatemi, S. Fang, K. Watanabe, T. Taniguchi, E. Kaxiras, P. Jarillo-Herrero, Unconventional superconductivity in magic-angle graphene superlattices, Nature 556(7699) (2018) 43.

[53] A. Abdelkader, A. Cooper, R. Dryfe, I. Kinloch, How to get between the sheets: a review of recent works on the electrochemical exfoliation of graphene materials from bulk graphite, Nanoscale 7(16) (2015) 6944-6956.

[54] V.B. Mohan, K.-t. Lau, D. Hui, D. Bhattacharyya, Graphene-based materials and their composites: A review on production, applications and product limitations, Composites Part B: Engineering 142 (2018) 200-220.

[55] A. Adetayo, D. Runsewe, Synthesis and fabrication of graphene and graphene oxide: a review, Open journal of composite materials 9(02) (2019) 207.

[56] L. Ci, L. Song, D. Jariwala, A.L. Elías, W. Gao, M. Terrones, P.M. Ajayan, Graphene shape control by multistage cutting and transfer, Advanced Materials 21(44) (2009) 4487-4491.

[57] X. Lu, M. Yu, H. Huang, R.S. Ruoff, Tailoring graphite with the goal of achieving single sheets, Nanotechnology 10(3) (1999) 269.

[58] X. Liang, A.S. Chang, Y. Zhang, B.D. Harteneck, H. Choo, D.L. Olynick, S. Cabrini, Electrostatic force assisted exfoliation of prepatterned few-layer graphenes into device sites, Nano letters 9(1) (2009) 467-472.

[59] A. Reina, X. Jia, J. Ho, D. Nezich, H. Son, V. Bulovic, M.S. Dresselhaus, J. Kong, Large area, few-layer graphene films on arbitrary substrates by chemical vapor deposition, Nano letters 9(1) (2009) 30-35.

[60] K.S. Kim, Y. Zhao, H. Jang, S.Y. Lee, J.M. Kim, K.S. Kim, J.-H. Ahn, P. Kim, J.-Y. Choi, B.H. Hong, Large-scale pattern growth of graphene films for stretchable transparent electrodes, nature 457(7230) (2009) 706-710.

[61] P.W. Sutter, J.-I. Flege, E.A. Sutter, Epitaxial graphene on ruthenium, Nature materials 7(5) (2008) 406-411.

[62] J. Phiri, P. Gane, T.C. Maloney, General overview of graphene: Production, properties and application in polymer composites, Materials Science and Engineering: B 215 (2017) 9-28.

[63] N. Parveen, M.O. Ansari, M.H. Cho, Correction: Simple route for gram synthesis of less defective few layered graphene and its electrochemical performance, RSC Advances 6(21) (2016) 17384-17385.

[64] C. Vallés, C. Drummond, H. Saadaoui, C.A. Furtado, M. He, O. Roubeau, L. Ortolani, M. Monthioux, A. Pénicaud, Solutions of negatively charged graphene sheets and ribbons, Journal of the american chemical society 130(47) (2008) 15802-15804.

[65] J. Chen, B. Yao, C. Li, G. Shi, An improved Hummers method for eco-friendly synthesis of graphene oxide, Carbon 64 (2013) 225-229.

[66] D.C. Marcano, D.V. Kosynkin, J.M. Berlin, A. Sinitskii, Z. Sun, A. Slesarev, L.B. Alemany, W. Lu, J.M. Tour, Improved synthesis of graphene oxide, ACS nano 4(8) (2010) 4806-4814.

[67] S. Park, J. An, J.R. Potts, A. Velamakanni, S. Murali, R.S. Ruoff, Hydrazine-reduction of graphite-and graphene oxide, Carbon 49(9) (2011) 3019-3023.

[68] S. Pei, J. Zhao, J. Du, W. Ren, H.-M. Cheng, Direct reduction of graphene oxide films into highly conductive and flexible graphene films by hydrohalic acids, Carbon 48(15) (2010) 4466-4474.

[69] J. Zhang, H. Yang, G. Shen, P. Cheng, J. Zhang, S. Guo, Reduction of graphene oxide via L-ascorbic acid, Chemical Communications 46(7) (2010) 1112-1114.

[70] S.Y. Toh, K.S. Loh, S.K. Kamarudin, W.R.W. Daud, Graphene production via electrochemical reduction of graphene oxide: synthesis and characterisation, Chemical Engineering Journal 251 (2014) 422-434.

[71] C.-Y. Su, A.-Y. Lu, Y. Xu, F.-R. Chen, A.N. Khlobystov, L.-J. Li, High-quality thin graphene films from fast electrochemical exfoliation, ACS nano 5(3) (2011) 2332-2339.

[72] P. Yu, S.E. Lowe, G.P. Simon, Y.L. Zhong, Electrochemical exfoliation of graphite and production of functional graphene, Current opinion in colloid & interface science 20(5-6) (2015) 329-338.

[73] K.S. Rao, J. Senthilnathan, Y.-F. Liu, M. Yoshimura, Role of peroxide ions in formation of graphene nanosheets by electrochemical exfoliation of graphite, Scientific reports 4 (2014) 4237.

[74] A.P. Kauling, A.T. Seefeldt, D.P. Pisoni, R.C. Pradeep, R. Bentini, R.V. Oliveira, K.S. Novoselov, A.H. Castro Neto, The Worldwide Graphene Flake Production, Advanced Materials (2018) 1803784.

[75] D. Wei, L. Grande, V. Chundi, R. White, C. Bower, P. Andrew, T. Ryhänen, Graphene from electrochemical exfoliation and its direct applications in enhanced energy storage devices, Chemical communications 48(9) (2012) 1239-1241.

[76] Y. Zhang, Y. Xu, J. Zhu, L. Li, X. Du, X. Sun, Electrochemically exfoliated high-yield graphene in ambient temperature molten salts and its application for flexible solid-state supercapacitors, Carbon 127 (2018) 392-403.

[77] C.A. Sequeira, D.S. Cardoso, M.L.F. Gameiro, Bipolar electrochemistry, a focal point of future research, Chemical Engineering Communications 203(8) (2016) 1001-1008.

[78] M. Fleischmann, J. Ghoroghchian, D. Rolison, S. Pons, Electrochemical behavior of dispersions of spherical ultramicroelectrodes, The Journal of Physical Chemistry 90(23) (1986) 6392-6400.

[79] Y.V. Litovka, V. Mikheev, Numerical calculation of the electric field in an electroplating bath with bipolar electrodes, Theoretical Foundations of Chemical Engineering 40(3) (2006) 305-310.

[80] N. Ivanova, A. Gerasimchuk, N. Vlasenko, Kinetics of Copper (II) electrodeposition from dilute electrolytes with a bipolar electrode, Russian Journal of Applied Chemistry 75(7) (2002) 1079-1081.

[81] G. Loget, D. Zigah, L. Bouffier, N. Sojic, A. Kuhn, Bipolar electrochemistry: from materials science to motion and beyond, Accounts of chemical research 46(11) (2013) 2513-2523.

[82] C. Ulrich, O. Andersson, L. Nyholm, F. Björefors, Formation of molecular gradients on bipolar electrodes, Angewandte Chemie International Edition 47(16) (2008) 3034-3036.

[83] C.C. Mayorga‐Martinez, B. Khezri, A.Y.S. Eng, Z. Sofer, P. Ulbrich, M. Pumera, Bipolar Electrochemical Synthesis of WS2 Nanoparticles and Their Application in Magneto‐Immunosandwich Assay, Advanced Functional Materials 26(23) (2016) 4094-4098.

[84] R.J. Toh, C.C. Mayorga-Martinez, Z.k. Sofer, M. Pumera, MoSe2 nanolabels for electrochemical immunoassays, Analytical chemistry 88(24) (2016) 12204-12209.

[85] A.R. Baboukani, I. Khakpour, V. Drozd, A. Allagui, C. Wang, Single-step exfoliation of black phosphorus and deposition of phosphorene via bipolar electrochemistry for capacitive energy storage application, Journal of Materials Chemistry A 7(44) (2019) 25548-25556.

[86] H. Ertl, J.W. Kolar, F.C. Zach, A novel multicell DC-AC converter for applications in renewable energy systems, IEEE Transactions on industrial Electronics 49(5) (2002) 1048-1057.

[87] V. Singh, D. Joung, L. Zhai, S. Das, S.I. Khondaker, S. Seal, Graphene based materials: past, present and future, Progress in materials science 56(8) (2011) 1178-1271.

[88] P. Avouris, C. Dimitrakopoulos, Graphene: synthesis and applications, Materials today 15(3) (2012) 86-97.

[89] P. Mahanandia, F. Simon, G. Heinrich, K.K. Nanda, An electrochemical method for the synthesis of few layer graphene sheets for high temperature applications, Chemical Communications 50(35) (2014) 4613-4615.

[90] G.M. Crouch, D. Han, S.K. Fullerton-Shirey, D.B. Go, P.W. Bohn, Addressable direct-write nanoscale filament formation and dissolution by nanoparticle-mediated bipolar electrochemistry, ACS nano 11(5) (2017) 4976-4984.

[91] M.G. González, J.C. Cabanelas, J. Baselga, Applications of FTIR on epoxy resins-identification, monitoring the curing process, phase separation and water uptake, Infrared Spectroscopy-Materials Science, Engineering and Technology, InTech2012.

[92] J. Coates, Interpretation of infrared spectra, a practical approach, Encyclopedia of analytical chemistry 12 (2000) 10815-10837.

[93] V. Ţucureanu, A. Matei, A.M. Avram, FTIR spectroscopy for carbon family study, Critical reviews in analytical chemistry 46(6) (2016) 502-520.

[94] A.C. Ferrari, D.M. Basko, Raman spectroscopy as a versatile tool for studying the properties of graphene, Nature nanotechnology 8(4) (2013) 235-246.

[95] A. Kaniyoor, S. Ramaprabhu, A Raman spectroscopic investigation of graphite oxide derived graphene, Aip Advances 2(3) (2012) 032183.

[96] Y. Shao, J. Wang, M. Engelhard, C. Wang, Y. Lin, Facile and controllable electrochemical reduction of graphene oxide and its applications, Journal of Materials Chemistry 20(4) (2010) 743-748.

[97] S.J. An, Y. Zhu, S.H. Lee, M.D. Stoller, T. Emilsson, S. Park, A. Velamakanni, J. An, R.S. Ruoff, Thin film fabrication and simultaneous anodic reduction of deposited graphene oxide platelets by electrophoretic deposition, The Journal of Physical Chemistry Letters 1(8) (2010) 1259-1263.

[98] S. Park, J. An, I. Jung, R.D. Piner, S.J. An, X. Li, A. Velamakanni, R.S. Ruoff, Colloidal suspensions of highly reduced graphene oxide in a wide variety of organic solvents, Nano letters 9(4) (2009) 1593-1597.

[99] N.R. Wilson, P.A. Pandey, R. Beanland, R.J. Young, I.A. Kinloch, L. Gong, Z. Liu, K. Suenaga, J.P. Rourke, S.J. York, Graphene oxide: structural analysis and application as a highly transparent support for electron microscopy, ACS nano 3(9) (2009) 2547-2556.

[100] K. Krishnamoorthy, M. Veerapandian, K. Yun, S.-J. Kim, The chemical and structural analysis of graphene oxide with different degrees of oxidation, Carbon 53 (2013) 38-49.

[101] J. Meyer, A. Geim, M. Katsnelson, K. Novoselov, D. Obergfell, S. Roth, C. Girit, A. Zettl, On the roughness of single-and bi-layer graphene membranes, Solid State Communications 143(1-2) (2007) 101-109.

[102] A. Allagui, A.S. Elwakil, M.E. Fouda, A.G. Radwan, Capacitive behavior and stored energy in supercapacitors at power line frequencies, Journal of Power Sources 390 (2018) 142-147.

[103] A. Allagui, Z. Said, M.A. Abdelkareem, A.S. Elwakil, M. Yang, H. Alawadhi, DC and AC performance of graphite films supercapacitors prepared by contact glow discharge electrolysis, Journal of The Electrochemical Society 164(12) (2017) A2539-A2546.

[104] A. Allagui, A.S. Elwakil, Z. Said, M.A. Abdelkareem, D. Zhang, Band‐Pass Filter and Relaxation Oscillator using Electric Double‐Layer Capacitor, ChemElectroChem 5(23) (2018) 3793-3798.

[105] A. Elwakil, A. Allagui, B. Maundy, C. Psychalinos, A low frequency oscillator using a super-capacitor, AEU-International Journal of Electronics and Communications 70(7) (2016) 970-973.

[106] A. Allagui, T.J. Freeborn, A.S. Elwakil, M.E. Fouda, B.J. Maundy, A.G. Radwan, Z. Said, M.A. Abdelkareem, Review of fractional-order electrical characterization of supercapacitors, Journal of Power Sources 400 (2018) 457-467.

[107] A. Allagui, T.J. Freeborn, A.S. Elwakil, B.J. Maundy, Reevaluation of performance of electric double-layer capacitors from constant-current charge/discharge and cyclic voltammetry, Scientific reports 6 (2016) 38568.

[108] M. Kaempgen, C.K. Chan, J. Ma, Y. Cui, G. Gruner, Printable thin film supercapacitors using single-walled carbon nanotubes, Nano letters 9(5) (2009) 1872-1876.

[109] J.J. Yoo, K. Balakrishnan, J. Huang, V. Meunier, B.G. Sumpter, A. Srivastava, M. Conway, A.L. Mohana Reddy, J. Yu, R. Vajtai, Ultrathin planar graphene supercapacitors, Nano letters 11(4) (2011) 1423-1427.

[110] J. Xia, F. Chen, J. Li, N. Tao, Measurement of the quantum capacitance of graphene, Nature nanotechnology 4(8) (2009) 505.

[111] Z.S. Wu, Z. Liu, K. Parvez, X. Feng, K. Müllen, Ultrathin Printable Graphene Supercapacitors with AC Line‐Filtering Performance, Advanced Materials 27(24) (2015) 3669-3675.

[112] G.S. Gund, J.H. Park, R. Harpalsinh, M. Kota, J.H. Shin, T.-i. Kim, Y. Gogotsi, H.S. Park, MXene/Polymer Hybrid Materials for Flexible AC-Filtering Electrochemical Capacitors, Joule 3(1) (2019) 164-176.

[113] J.-C. Bradley, H.-M. Chen, J. Crawford, J. Eckert, K. Ernazarova, T. Kurzeja, M. Lin, M. McGee, W. Nadler, S.G. Stephens, Creating electrical contacts between metal particles using directed electrochemical growth, Nature 389(6648) (1997) 268-271.

[114] C. Warakulwit, T. Nguyen, J. Majimel, M.-H. Delville, V. Lapeyre, P. Garrigue, V. Ravaine, J. Limtrakul, A. Kuhn, Dissymmetric carbon nanotubes by bipolar electrochemistry, Nano letters 8(2) (2008) 500-504.

[115] G. Loget, A. Kuhn, Electric field-induced chemical locomotion of conducting objects, Nature communications 2(1) (2011) 1-6.

[116] S. Munktell, M. Tydén, J. Högström, L. Nyholm, F. Björefors, Bipolar electrochemistry for high-throughput corrosion screening, Electrochemistry communications 34 (2013) 274-277.

[117] S.E. Fosdick, R.M. Crooks, Bipolar electrodes for rapid screening of electrocatalysts, Journal of the American Chemical Society 134(2) (2012) 863-866.

[118] A.R. Baboukani, I. Khakpour, V. Drozd, A. Allagui, C. Wang, Single-Step Exfoliation of Black Phosphorus and Deposition of Phosphorene via Bipolar Electrochemistry for Capacitive Energy Storage Application, Journal of Materials Chemistry A (2019).

[119] M. Pourbaix, J. Van Muylder, N. De Zoubov, Electrochemical properties of the platinum metals, Platinum Metals Review 3(2) (1959) 47-53.

[120] W. Wu, C. Lin, C. Yang, Fabrication and corrosion behaviour of platinum-coated titanium electrodes from low temperature molten salt electrolytes, Journal of applied electrochemistry 34(5) (2004) 525-531.

[121] W. Wu, Z. Chen, B. Li, X. Cong, Q. Chen, Mechanical and electrochemical properties of platinum coating by double glow plasma on titanium alloy substrate, Russian Journal of Electrochemistry 49(1) (2013) 76-80.

[122] N.-C. Yeh, C.-C. Hsu, J. Bagley, W.-S. Tseng, Single-step growth of graphene and graphene-based nanostructures by plasma-enhanced chemical vapor deposition, Nanotechnology 30(16) (2019) 162001.

[123] M.Z. Bazant, K. Thornton, A. Ajdari, Diffuse-charge dynamics in electrochemical systems, Physical review E 70(2) (2004) 021506.

[124] J. Duval, J.M. Kleijn, H.P. van Leeuwen, Bipolar electrode behaviour of the aluminium surface in a lateral electric field, Journal of Electroanalytical Chemistry 505(1-2) (2001) 1-11.

[125] S. Qian, J.F. Duval, Coupling between electroosmotically driven flow and bipolar faradaic depolarization processes in electron-conducting microchannels, Journal of colloid and interface science 297(1) (2006) 341-352.

[126] S. Karmakar, Selective synthesis of DC carbon arc-generated carbon nanotube and layered-graphene and the associated mechanism, Nanotechnology 32(10) (2020) 105602.

[127] K. Parvez, R. Li, S.R. Puniredd, Y. Hernandez, F. Hinkel, S. Wang, X. Feng, K. Müllen, Electrochemically exfoliated graphene as solution-processable, highly conductive electrodes for organic electronics, ACS nano 7(4) (2013) 3598-3606.

[128] J. Liu, H. Yang, S.G. Zhen, C.K. Poh, A. Chaurasia, J. Luo, X. Wu, E.K.L. Yeow, N.G. Sahoo, J. Lin, A green approach to the synthesis of high-quality graphene oxide flakes via electrochemical exfoliation of pencil core, Rsc Advances 3(29) (2013) 11745-11750.

[129] K. Parvez, Z.-S. Wu, R. Li, X. Liu, R. Graf, X. Feng, K. Müllen, Exfoliation of graphite into graphene in aqueous solutions of inorganic salts, Journal of the American Chemical Society 136(16) (2014) 6083-6091.

[130] J. Yao, Y. Jia, Q. Han, D. Yang, Q. Pan, S. Yao, J. Li, L. Duan, J. Liu, Ternary flower-sphere-like MnO2-graphite/reduced graphene oxide nanocomposites for supercapacitor, Nanotechnology 32(18) (2021) 185401.

[131] H. Hashimoto, Y. Muramatsu, Y. Nishina, H. Asoh, Bipolar anodic electrochemical exfoliation of graphite powders, Electrochemistry Communications (2019).

[132] G. Çakmak, T. Öztürk, Continuous synthesis of graphite with tunable interlayer distance, Diamond and Related Materials 96 (2019) 134-139.

[133] A.M. Abdelkader, I.A. Kinloch, R.A. Dryfe, Continuous electrochemical exfoliation of micrometer-sized graphene using synergistic ion intercalations and organic solvents, ACS applied materials & interfaces 6(3) (2014) 1632-1639.

[134] M. Mao, M. Wang, J. Hu, G. Lei, S. Chen, H. Liu, Simultaneous electrochemical synthesis of few-layer graphene flakes on both electrodes in protic ionic liquids, Chemical Communications 49(46) (2013) 5301-5303.

[135] J. Wang, K.K. Manga, Q. Bao, K.P. Loh, High-yield synthesis of few-layer graphene flakes through electrochemical expansion of graphite in propylene carbonate electrolyte, Journal of the American Chemical Society 133(23) (2011) 8888-8891.

[136] M. Xu, H. Sun, C. Shen, S. Yang, W. Que, Y. Zhang, X. Song, Lithium-assisted exfoliation of pristine graphite for few-layer graphene nanosheets, Nano Research 8(3) (2015) 801-807.

[137] D.R. Gaskell, Introduction to the Thermodynamics of Materials, CRC press2012.

[138] A. Arora, J.C. Eijkel, W.E. Morf, A. Manz, A wireless electrochemiluminescence detector applied to direct and indirect detection for electrophoresis on a microfabricated glass device, Analytical chemistry 73(14) (2001) 3282-3288.

[139] M. Zhu, R. Outlaw, M. Bagge-Hansen, H. Chen, D. Manos, Enhanced field emission of vertically oriented carbon nanosheets synthesized by C2H2/H2 plasma enhanced CVD, Carbon 49(7) (2011) 2526-2531.

[140] R. Thomas, G.M. Rao, Synthesis of 3-dimensional porous graphene nanosheets using electron cyclotron resonance plasma enhanced chemical vapour deposition, RSC Advances 5(103) (2015) 84927-84935.

[141] A. Malesevic, R. Vitchev, K. Schouteden, A. Volodin, L. Zhang, G. Van Tendeloo, A. Vanhulsel, C. Van Haesendonck, Synthesis of few-layer graphene via microwave plasma-enhanced chemical vapour deposition, Nanotechnology 19(30) (2008) 305604.

[142] H. Hashimoto, Y. Muramatsu, Y. Nishina, H.J.E.C. Asoh, Bipolar anodic electrochemical exfoliation of graphite powders, (2019).

[143] I. Khakpour, A.R. Baboukani, A. Allagui, A.A. Hachicha, C. Wang, On the mechanistic pathways of exfoliation-and-deposition of graphene by bipolar electrochemistry, Nanotechnology 32(34) (2021) 345603.

[144] A. Allagui, A.S. Elwakil, C. Psychalinos, Decoupling the magnitude and phase in a constant phase element, Journal of Electroanalytical Chemistry 888 (2021) 115153.

[145] A. Allagui, A.S. Elwakil, H. Eleuch, Highlighting a Common Confusion in the Computation of Capacitance of Electrochemical Energy Storage Devices, ACS Publications, 2021.

[146] A. Allagui, A.S. Elwakil, M.E. Fouda, Revisiting the Time-Domain and Frequency-Domain Definitions of Capacitance, IEEE Transactions on Electron Devices (2021).

[147] P. Taberna, P. Simon, J.-F. Fauvarque, Electrochemical characteristics and impedance spectroscopy studies of carbon-carbon supercapacitors, Journal of the Electrochemical Society 150(3) (2003) A292.

[148] D. Zhao, W. Chang, C. Lu, C. Yang, K. Jiang, X. Chang, H. Lin, F. Zhang, S. Han, Z. Hou, Charge transfer salt and graphene heterostructure‐based micro‐supercapacitors with alternating current line‐filtering performance, Small 15(48) (2019) 1901494.

[149] C. Xu, L. Jiang, X. Li, C. Li, C. Shao, P. Zuo, M. Liang, L. Qu, T. Cui, Miniaturized high-performance metallic 1T-Phase MoS2 micro-supercapacitors fabricated by temporally shaped femtosecond pulses, Nano Energy 67 (2020) 104260.

[150] S. Xu, W. Liu, B. Hu, X. Wang, Circuit-integratable high-frequency micro supercapacitors with filter/oscillator demonstrations, Nano Energy 58 (2019) 803-810.

[151] P. Giannakou, M.G. Masteghin, R.C. Slade, S.J. Hinder, M. Shkunov, Energy storage on demand: ultra-high-rate and high-energy-density inkjet-printed NiO micro-supercapacitors, Journal of Materials Chemistry A 7(37) (2019) 21496-21506.

[152] C. Yang, K.S. Schellhammer, F. Ortmann, S. Sun, R. Dong, M. Karakus, Z. Mics, M. Löffler, F. Zhang, X. Zhuang, Coordination Polymer Framework Based On‐Chip Micro‐Supercapacitors with AC Line‐Filtering Performance, Angewandte Chemie International Edition 56(14) (2017) 3920-3924.

[153] T. Yu, Y. Wang, K. Jiang, G. Zhai, C. Ke, J. Zhang, J. Li, D. Tranca, E. Kymakis, X. Zhuang, Catechol‐coordinated framework film‐based micro‐supercapacitors with AC line filtering performance, Chemistry‐A European Journal (2021).

[154] F. Xia, S. Xu, B. Hu, X. Jia, X. Wang, High-frequency Micro Supercapacitors Based on High-aspect-ratio 3D Nanoporous Gold Interdigital Electrodes for On-chip Filtering, 2019 20th International Conference on Solid-State Sensors, Actuators and Microsystems & Eurosensors XXXIII (TRANSDUCERS & EUROSENSORS XXXIII), IEEE, 2019, pp. 1447-1450.

[155] W. Hua, J. Xiu, F. Xiu, Z. Zhang, J. Liu, L. Lai, W. Huang, Micro-supercapacitors based on oriented coordination polymer thin films for AC line-filtering, RSC advances 8(53) (2018) 30624-30628.

[156] Z. Chen, Y. Chen, Y. Zhao, F. Qiu, K. Jiang, S. Huang, C. Ke, J. Zhu, D. Tranca, X. Zhuang, B/N-Enriched Semi-Conductive Polymer Film for Micro-Supercapacitors with AC Line-Filtering Performance, Langmuir (2021).

VITA

IMAN KHAKPOUR

2006-2011	B.Sc., Materials Science and Engineering Shiraz University, Shiraz, Iran
2011-2014	M.Sc., Materials Science and Engineering University of Tehran, Tehran, Iran
2017-2021	Doctoral Candidate (Ph.D.), Materials Science and Engineering Florida International University, Miami, FL, USA

- Dissertation Year Fellowship (DYF), Florida International University (2020)
- Doctoral Evidence Acquisition (DEA) Fellowship, Florida International University (2020)

SELECTED PUBLICATIONS / PATENTS / PRESENTATIONS:

I. Khakpour, A. Rabiei Baboukani, A. Allagui, C. Wang, Bipolar Exfoliation and in Situ Deposition of High-Quality Graphene for Supercapacitor Application, ACS Applied Energy Materials 2(7) (2019) 4813-4820.

I. Khakpour, A. Rabiei Baboukani, A. Allagui, A. Hachicha, C. Wang, On the Mechanistic Pathways of Exfoliation-and-Deposition of Graphene by Bipolar Electrochemistry, Nanotechnology, https://doi.org/10.1088/1361-6528/ac037c.

I. Khakpour, A. Rabiei Baboukani, S. Forouzanfar, A. Allagui, C. Wang, In-plane interdigitated vertically-aligned graphene electrodes for high-frequency capability micro-supercapacitors, to be submited

A.R. Baboukani, I. Khakpour, V. Drozd, A. Allagui, C. Wang, Single-Step Exfoliation of Black Phosphorus and Deposition of Phosphorene via Bipolar Electrochemistry for Capacitive Energy Storage Application, Journal of Materials Chemistry A (2019).

A.R. Baboukani, I. Khakpour, E. Adelowo, V. Drozd, W. Shang, C. Wang, High-performance red phosphorus-sulfurized polyacrylonitrile composite by electrostatic spray deposition for lithium-ion batteries, Electrochimica Acta 345 (2020) 136227.

A. Rabiei Baboukani, I. Khakpour, V. Drozd, C. Wang, Liquid-Based Exfoliation of Black Phosphorus into Phosphorene and Its Application for Energy Storage Devices, Small Structures (2021) 2000148.

A. Allagui, D. Zhang, I. Khakpour, A.S. Elwakil, C. Wang, Quantification of memory in fractional-order capacitors, Journal of Physics D: Applied Physics 53(2) (2019) 02LT03.

S. Forouzanfar, F. Alam, I. Khakpour, A.R. Baboukani, N. Pala, C. Wang, Highly Sensitive Lactic Acid Biosensors Based on Photoresist Derived Carbon, IEEE Sensors Journal (2020).

J. Belisario, S. Mondal, I. Khakpour, A.F. Hernandez, A. Durygin, Z. Cheng, Synthesis and flash sintering of (Hf1-xZrx) B2 solid solution powders, Journal of the European Ceramic Society 41(4) (2021) 2215-2225.

S. Aghaei, I. Torres, A. Baboukani, I. Khakpour, C. Wang, Impact of surface oxidation on the structural, electronic transport, and optical properties of two-dimensional titanium nitride (Ti3N2) MXene, Computational Condensed Matter 20 (2019) e00382.

E. Adelowo, A.R. Baboukani, O. Okpowe, I. Khakpour, M. Safa, C. Chen, C. Wang, A high-energy aqueous on-chip lithium-ion capacitor based on interdigital 3D carbon microelectrode arrays, Journal of Power Sources 455 (2020) 227987.

I. Khakpour, A. Rabiei Baboukani, A. Allagui, C. Wang, "*Bipolar Exfoliation and In-situ Deposition of High-Quality Reduced Graphene on Negative Feeding Electrodes*", Under Review, United States Patent.

A.R. Baboukani, I. Khakpour, C. Wang, "Bipolar Exfoliation of Black Phosphorus into Phosphorene", US 10,676,357, 2020.

A.R. Baboukani, I. Khakpour, C. Wang, V. Drozd, A. Allagui, "Bipolar exfoliation and deposition of phosphorene onto negative feeding electrode", US 11,034,584, 2021.

I. Khakpour, A.R. Baboukani, V. Drozd, A. Allagui, and C. Wang, Simultaneous Exfoliation and Deposition of Graphene and Phosphorene Through Bipolar Electrochemistry, MRS Fall Meeting & Exhibit, Massachusetts, Boston, December 1-6, 2019.

I. Khakpour, A.R. Baboukani, C. Wang, Bipolar Electrochemically Exfoliated Graphene for Supercapacitor Application, 235th Electrochemical Society Meeting (ECS), Texas, Dallas, May 26-30, 2019.

I. Khakpour, A.R. Baboukani, A. Allagui, and C. Wang, Electrochemical Characterization of Bipolar Electrochemically Exfoliated Graphene, AAAFM Meeting, Leangles, California, Aug 19-22, 2019.

I. Khakpour, A.R. Baboukani, Anis Allagui, and C. Wang, Bipolar Electrochemically Exfoliated Graphene for Supercapacitor application, Virtual ECS PRiME Meeting, Honolulu, Hawaii, Oct 4-9, 2020.